The Hong Kong Polytechnic University
Department of Applied Physics

Functional Thin-Film Transistors Based on Hybrid Materials

SUN Zhenhua

A thesis submitted in partial fulfillment of the requirements for
the degree of Doctor of Philosophy

June 2012

CERTIFICATE OF ORIGINALITY

I hereby declare that this thesis is my own work and that, to the best of my knowledge and belief, it reproduces no material previously published or written, nor material that has been accepted for the award of any other degree or diploma, except where due acknowledgement has been made in the text.

______________________________(Signed)

Sun Zhenhua ______________________________(Name of student)

Abstract

Functional thin film transistors (TFTs) have attracted increasing interest due to their potential applications in many areas with excellent performance. Such devices can be realized with hybrid materials, which can demonstrate not only the desired properties of their components but also some unique synergistic effect. Therefore, it is important to develop the techniques of tailoring hybrid materials to realize various types of functional TFTs.

In this thesis, the applications of functional TFTs are introduced at the beginning. Various TFTs with different functions are described and the photodetectors and memories closely related to this thesis are discussed in details. Their working principles and the current situation of research are reviewed. Then hybrid materials are discussed on their history and classification. Therein, the most important organic-inorganic hybrid materials and the graphene-inorganic hybrid materials which are the rising hotspots are introduced. Their synthesis and applications are reviewed. The reported functional TFTs based on the hybrid materials are listed for reference.

The phototransistors and light driving memories based on hybrid materials have been carefully studied by us. In these devices, graphene or polymers acted as conducting media and inorganic components were used to absorb light. We found that the interface properties in the hybrid materials were critical to the performance of optoelectronic devices, which have been optimized in our experiments.

Near infrared (NIR) phototransistors based on poly(3-hexylthiophene) (P3HT)/Lead sulfide (PbS) quantum dots (QD) and graphene/PbS QDs hybrid films were fabricated and characterized. The phototransistors based on P3HT/PbS QDs show high photoresponsivity up to 2×10^4 A/W under NIR of 895nm with low light irradiance. This value is larger than the record of organic phototransistors. Under NIR illumination, the transfer curves shift to high gate voltage horizontally. Therefore the conductivity of the hybrid film changes under NIR light illumination at a constant gate voltage. This behavior is attributed to the photo induced electrons generated in PbS QDs which will induce field effect doping effect in P3HT films. Same effect happens in graphene/PbS QDs hybrid phototransistors which show ultrahigh photoresponsivity of 1×10^7 A/W. This high value is due to the high carrier mobility in graphene. The devices can be fabricated on flexible substrates and show stable performance. All of the aforementioned devices show fast response and their photoresponse behaviors can be described by a physical mode.

P3HT/Titania (TiO_2) nanoparticles hybrid materials have been investigated. It was found that hole mobility in P3HT can be enhanced by pyridine-capped TiO_2 nanorods. Both the shape of nanoparticles and surface ligand were proved crucial to the enhancement. Characterizations of the hybrid films showed that this enhancement of hole mobility can be attribute to the improved crystallinity of P3HT which may be induced by the self-assembly effect cased by pyridine-capped TiO_2 nanorods. The ultraviolet (UV) phototransistor fabricated based on this kind of hybrid film show much better performance than the devices based on TiO_2 nanoparticles without the surface modification of pyridine.

Light driving, multilevel, rewritable and nonvolatile memories were fabricated with CVD grown single-layer graphene decorated with TiO_2 nanodots which are capped with pyridine ligand on the surface. The memory is a TFT with a bottom-gate top-contact structure. The conductivity of the channel can be changed by UV illumination and shows excellent retention property. Since the conductivity can be modulated to various values by carefully controlling the illumination conditions, including the light intensity and illumination time, the device can be used as a multilevel memory. Thus different conductive state can be regarded as nonvolatile information programmed by UV illumination. The change of the conductivity of the channel can be attributed to net positive charges generated in TiO_2 nanodots under UV. The pyridine surface ligand which can trap the photon-induced holes in TiO_2 is critical to the nonvolatile memory effect. Positive gate voltage can be used to erase the excitation states thus make the memory rewritable. This study opens a novel path towards nonvolatile multilevel memories.

List of Publications

1. **Zhenhua Sun**, Zhike Liu, Jinhua Li, Guoan Tai, Shu-Ping Lau and Feng Yan. "Infrared Photodetectors Based on CVD-grown Graphene and PbS Quantum Dots with Ultrahigh Responsivity" *Adv. Mater.* 24 (2012) 5878–5883.
2. **Zhenhua Sun**, Jinhua Li, Chenming Liu, Shihe Yang and Feng Yan. "Enhancement of Hole Mobility of Poly(3-hexylthiophene) Induced by Titania Nanorods in Composite Films" *Adv. Mater.* 23 (2011) 3648–3652.
3. **Zhenhua Sun**, Jinhua Li and Feng Yan, Highly sensitive organic near-infrared phototransistors based on poly(3-hexylthiophene) and PbS quantum dots, *J. Mater. Chem*. 22 (2012) 21673-21678.
4. Jinhua Li, **Zhenhua Sun** and Feng Yan. "Solution Processable Low-Voltage Organic Thin Film Transistors with High- *k* Relaxor Ferroelectric Polymer as Gate Insulator" *Adv. Mater.* 24 (2012) 88–93.
5. Haixin Chang, **Zhenhua Sun**, Qinghong Yua, Feng Ding, Xiaoming Tao, Feng Yan, and Zijian Zheng. "Thin Film Field-Effect Phototransistors from Bandgap-Tunable, solution-Processed, Few-Layer Reduced Graphene Oxide Films" *Adv. Mater.* 22 (2010) 4872–4876.
6. Haixin Chang, **Zhenhua Sun**, Keith Yat-Fung Ho, Xiaoming Tao, Feng Yan, Wai-Ming Kwok and Zijian Zheng. "A highly sensitive ultraviolet sensor based on

a facile in situ solution-grown ZnO nanorod/graphene heterostructure" *Nanoscale*, 3 (2011) 258.

7. Zhike Liu, Jinhua Li, **Zhenhua Sun**, Guoan Tai, Shu-Ping Lau, and Feng Yan. "The application of Highly Doped Single-Layer Graphene as the Top Electrodes of Semitransparent Organic Solar Cells" *ACS Nano*, 6 (2012) 810-818.
8. Yeung Yu Hui, Guo'an Tai, **Zhenhua Sun**, Zihan Xu, Ning Wang, Feng Yan and Shu Ping Lau. "Modulation of field effect characteristics in graphene based field effect transistors by the thickness of ZnO nanomesh coating" *Nanoscale*, 4 (2012) 3118–3122.
9. Guo'an Tai, Kai Wang, **Zhenhua Sun**, Jun Yin, Sheung Mei Ng, Jianxin Zhou, Feng Yan, Chi Wah Leung, Kin Hung Wong, Wanlin Guo, and Shu Ping Lau. "Nonlithographic Fabrication of Crystalline Silicon Nanodots on Graphene" *J. Phys. Chem. C*, 116 (2012) 532–537.
10. Qidong Tai, Jinhua Li, Zhike Liu, ***Zhenhua Sun***, Xingzhong Zhao and Feng Yan. "Enhanced photovoltaic performance of polymer solar cells by adding fullerene end-capped polyethylene glycol" *J. Mater. Chem.* 21 (2011) 6848.

Acknowledgements

Firstly, I would like to express my sincere appreciation to my chief supervisor, Dr. Yan Feng. He always guides me with his profound knowledge, inspires me with his remarkable insight and supports me with his great patience. It is impossible for me to complete my research works and finish this thesis smoothly without his generous assistance. His edification will benefit me not only in my graduate stage, but also throughout my entire research career.

Then I am grateful to my co-supervisor, Dr. Wong Yuen Wah. His kind encouragement is very important for me to get through the rough stages of my works.

It is an honor for me to get valuable suggestions from Pro. Helen L.W. Chan, Prof. Wong Kin Hung and Prof. Dai Jiyan. These suggestions have been of great help to me.

I am indebted to the stuffs and my colleagues who supported me in my works. I would like to thank Mr Yeung Man Nin, Dr Lu Wei and Dr. Albert Choy for their assistance in facility utilization in our department. I would like to give my thanks to my colleagues Mr Lin Peng, Mr. Mok Sheung Man, Dr. Tang Hao, Dr. Wu Sujuan, Mr. Tai Qidong, Dr. Cheng Lihong, Mr. Li Jinhua, Mr. Liu Zhike, Mr. He Rongxiang, Mr. Zhu Hongwei, Mr. Zhao Meng, Mr. Vincent Chan, Miss Yao Yanli, Miss Zhang

Meng, Mr Chen Bolei, Mr Liu Yuming, Mr Jian Aoqun, Mr Wei Changsong, Mr Wang Kai, Mr Yeung Yu Hui and Dr Tai Guo’an for their great help and assistance. The discussions with them have given me many helpful inspirations. I would also like to thank Dr Liu Chenmin and Dr Chang Haixin for their cooperation in our collaborative works.

Here I have the honor to be friend of some excellent peoples and I’d like to express my thanks to them for their kind encouragement and company. They are Mr Zhang Shishun, Mr Wang Wei, Mr Xi Qiang, Mr C.M. Luk, Mr S. T. F. LEE, Miss M. K. Lau and Mr C. M. Tang. My lift in Hong Kong becomes colorful and memorable because of them.

Finally from my heart, I would like to express thank and love to my family, my dear father, mother and my sisters, who always support me whenever and wherever. If any achievement comes to me, I’d like to delicate it to them.

Table of Content

List of Figures

List of Tables

List of Symbols

Symbols	**Meaning**
W	Channel width
L	Channel length
μ	Carrier mobility
C_i	Capacitance of the gate insulator
V_t	Threshold voltage
I_{DS}	Source-drain current
V_{DS}	Source-drain bias
V_G	Gate bias
I_{ill}	I_{DS} under illumination
I_{Dark}	I_{DS} in dark
A	Channel area exposed under illumination
E_e	Light irradiance
R	Photoresponsivity
P	Photoswitching ratio

Chapter 1 **Introduction**

1.1 **Background**

Since the invention of the first field effect device by J. E. Lilienfeld in 1934 [1], field effect transistors (FETs) have become the elementary bricks of modern electronic industry after extensive evolution and development for decades. In particular, the silicon-based metal-oxide-semiconductor field-effect transistors (MOSFETs), whose structure is shown in Figure 1.1, have defeated other types of transistor with different forms (such as bipolar transistor) or different materials (such as Ⅲ-Ⅴ semiconductors) because of their advantages including easy fabrication, low cost and

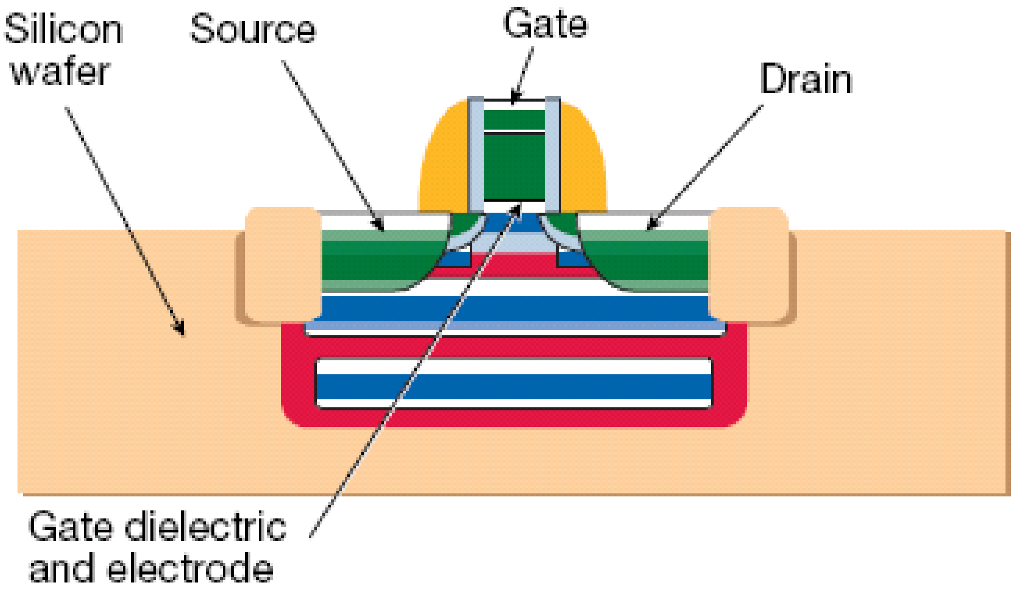

Figure 1.1 Schematic of metal-oxide-semiconductor field-effect transistor (MOSFET) [2].

small size [3]. Nowadays the MOSFETs have become the mainstream choices of large scale integrated circuits and widely used in microprocessors, logic memories, CCD cameras and so on. The explosion of portable electronic devices such as laptop computers and cell phones benefits largely from the achievement obtained in the miniaturization of MOSFET and high density cells array [2, 4], as shown in Figure 1.2

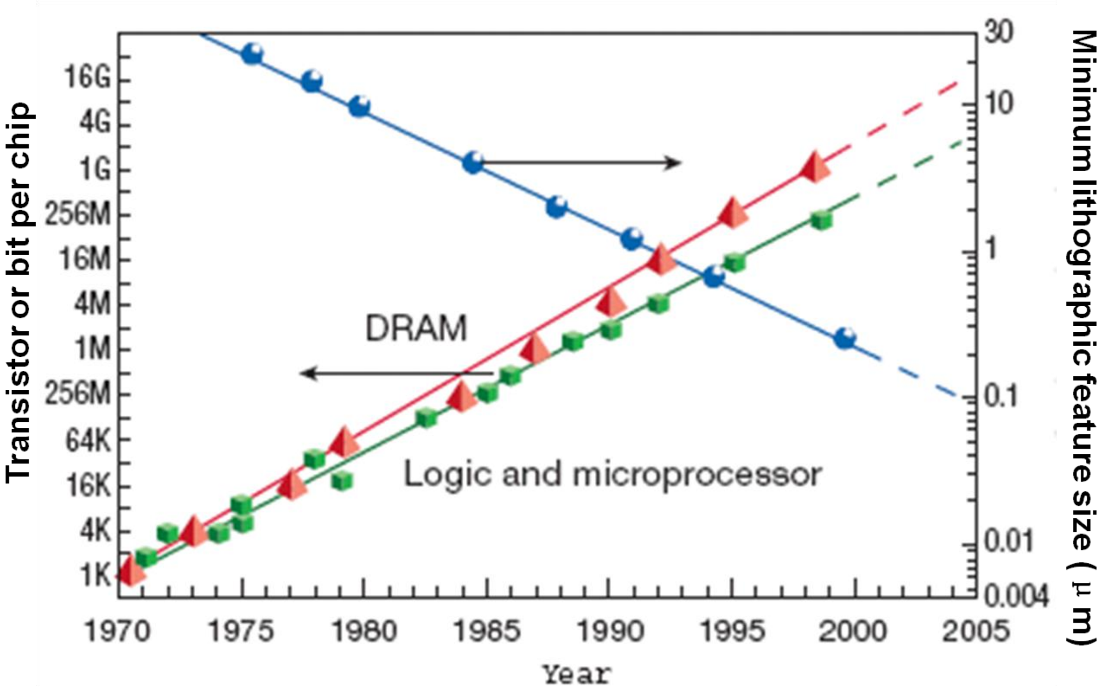

Figure 1.2 Developments of device densities and minimum feature sizes of lithographic. Both dynamic random access memory (DRAM) and logic devices are shown inside [4].

On the other hand, first thin film transistor (TFT) was proposed by Paul. K. Weimer et al. in 1962 and aroused huge interest soon [5-7]. Essentially TFTs are a kind of enhancement-mode FETs with thin films deposited as active layer, dielectric layer as well as electrodes. Compared with MOSFETs, TFTs can be fabricated under a lower temperature and on various substrates such as glass. Amorphous and polycrystalline silicon are the main choices of the active layer in a TFT for their optimal trade-off between high mobility and low cost. TFTs' thin film property and high integration ability as driver circuit make them suitable as switchers for active matrix panel display devices. In fact, the display industry is the largest application area of TFTs by far and, in 2007, about 10^{15} TFTs were made for it [8].

In the process to optimize and miniaturize TFTs, many functional devices based on TFTs have been invented and developed. Nowadays, TFTs are used not only as switchers or amplifiers in logic circuits, but also as various functional devices such as photodetectors [9, 10], memory [11], sensors [12] and light emitting devices [13, 14]. These functional TFTs have large application potentials in waveguide communication, electronic equipments, environmental monitoring, military defense, medical diagnostics and so on [8, 15]. Conventional functional devices in the market such as various photodetectors and memories have both economic and performance drawbacks [10, 16, 17]. Compared with them, functional TFTs possess advantages such as higher performance (sensors), low cost (photodetectors and memories) and smart operation derived from the gate electrodes (photodetectors and light emitting TFTs) [15, 18-20].

Electronic devices keep progressing toward miniaturization, high speed, low cost, flexible and even transparent. In this process, silicon materials are exhausting themselves. A variety of novel materials have been proposed to meet the future demands [21]. For example, Organic semiconductors including both conductive polymers and small molecular semiconductors are investigated as active layer in FETs for their unique properties such as low cost, solution-processibility and flexibility [22]. High-*k* dielectric materials are considered as promising candidates of gate insulator for low voltage and high performance FETs [23]. Recently, graphene is the new hotspot material. Much effort has been devoted to its application in high speed FETs in view of its excellent electronic properties such as high carrier mobility [24, 25].

It is easy to understand the importance of materials to the performance of both conventional and new functional TFTs. However, it is impossible to find a single material to meet all the demands of a device, especially when the area is developed so fast. For example, commonly used inorganic semiconductors have high carrier mobility which is highly desired in TFTs. But at the same time they are rigid and difficult to process, which make them unsuitable for cheap and flexible devices. On the other hand, the widely investigated organic semiconductors are of low cost, solution-processible and have abundant optoelectronic properties. But they suffer from low carrier mobility. Therefore, hybrid materials, which can combine all the advantages of their components and even show some novel synergistic effect, are attracting more and more attention [26-30].

1.2 Significance of Research

Although huge effort has been made on hybrid materials and their application in functional FETs, some promising materials have not been involved yet. Sometimes, blending of distinct materials will induce degradation of the components' intrinsic properties, more or less. In this case negative influence will be inevitably imposed on the properties of hybrid materials and the performance of devices based on them. Here in our research, photodetectors with extraordinary performance and memories based on novel principle have been fabricated and characterized. These devices make use of the structure of TFT for not only its superiority on device performance, but also its advantages in physical mechanism research. Organic-inorganic and graphene-inorganic hybrid materials were used as the active layers of these functional TFT devices. The working principles of these functional TFTs have been clarified very particularly. The interactions of the components in these hybrid materials have been studied and a reliable mobility improvement of the organic component in the organic-inorganic hybrid material has been illustrated and investigated. Our research not only demonstrates several excellent functional TFT devices, but also proposes underlying physical mechanisms of them, which will be helpful for devices design and fabrication in these areas in future.

1.3 Structure of Thesis

The chapters of this thesis are organized as follows:

Chapter 1: Introduction. In this chapter, the background and significance of this research are introduced for better understanding of this research. In the meantime, the structure of this thesis is described for reading guidance.

Chapter 2: Overview of Functional TFTs and Hybrid Materials. In this chapter, working principle of TFTs is introduced and the applications of functional TFTs are overviewed. Particularly, the photodetectors and memories based on TFTs are introduced in details because they are the focuses in this research. Hybrid materials especially the organic-inorganic and graphene-inorganic hybrid mateirals and their applications in functional TFTs are discussed to offer readers an insight into this area.

Chapter 3: P3HT-TiO_2 Nanorods Hybrid Films with Enhanced Hole Mobility and Their Application in Ultraviolet Photodetectors. In this chapter, enhancement of hole mobility of P3HT induced by Titania (TiO_2) nanorods is demonstrated. The reasons of this phenomenon are discussed through characterizing the hybrid films and comparing the effects of different TiO_2 nanoparticles. The ultraviolet photodetectors based on this kind of hybrid films are illustrated finally.

Chapter 4: Highly Sensitive Organic Near-infrared Phototransistors Based on Poly(3-hexylthiophene) and PbS Quantum Dots. In this chapter, hybrid films of Poly(3-hexylthiophene) (P3HT) and Lead sulfide (PbS) quantum dots are used to fabricate solution-processible and high performance near infrared photodetectors. Figures of merit of this kind of device are characterized and mechanism of the photoresponse is discussed.

Chapter 5: Infrared Photodetectors based on CVD-grown Graphene and PbS Quanttum dots with Ultrahigh Responsivity. In this chapter, infrared photodetectors making use of hybrid films of graphene and PbS quantum dots are demonstrated. This kind of photodetector shows very high photoresponsivity and can be fabricated on both rigid and flexible substrates. Their performances are characterized and the working principle is clarified.

Chapter 6: Ultraviolet Driving Multilevel Memories Based on Graphene-TiO_2 Nanodots Hybrid Films. In this chapter, TFTs based on graphene-TiO_2 are fabricated and the TFTs show photoresponse to Ultraviolet (UV). The channel current is dependent on light intensity and illumination time and can retain after light is removed. Therefore, the devices can be used as nonvolatile memories. The kind of memory is proven to have multilevel feature and good erasability. Finally the physical mechanism of the memory behavior is discussed.

Chapter 7: Conclusion and Future Prospect. In this chapter, the results in this thesis are summarized and concluded. Meanwhile, future prospect of the research of functional TFTs is described.

Chapter 2 **Overview of Functional TFTs and Hybrid Materials**

2.1 Working Principle of TFTs

As addressed above, TFTs belong to a subcategory of FETs, mostly are the enhancement-mode FETs. In a TFT, thin films of semiconductor, dielectric and metal (or others conductive materials) are deposited on substrate layer by layer and serve as active layer, insulator layer and electrodes of the TFT, respectively. According to the positions of source, drain and gate electrodes, TFTs can be divided into four types: bottom gate-top contact, bottom gate-bottom contact, top gate-bottom contact and top gate-top contact TFTs. Their configurations are shown in Figure 2.1. Whichever structure, the active layer and the insulator layer keep contact and their interface is the place where the conducting channel is to be formed.

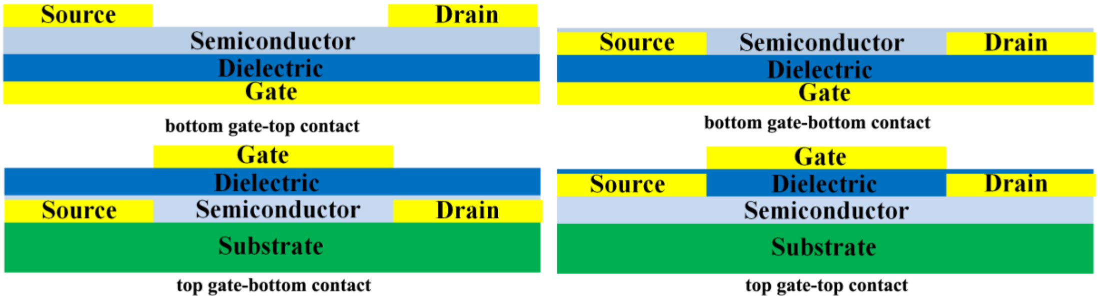

Figure 2.1 Structure schematics of four kinds of TFTs

The working mechanism schematic and performance characters of a TFT are shown in

Figure 2.2. Here the bottom gate-bottom contact structure and a p-type semiconductor are chosen as an example. When negative gate voltage (V_G) beyond the threshold voltage (V_t) is applied to the gate electrode and the source electrode is grounded, a very thin layer of holes will be induced in the semiconductor layer near insulator layer. This thin layer of holes will form the conducting channel for the source-drain current (I_{DS}) when a drain voltage (V_{DS}) is applied.

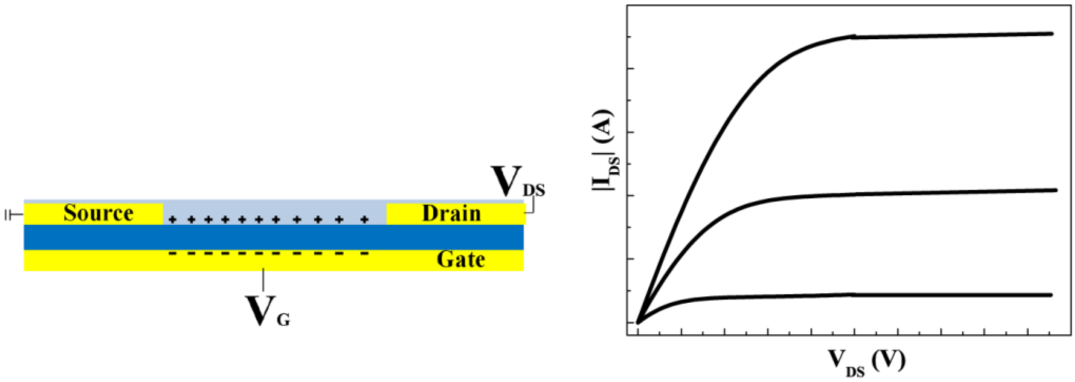

mechanism schematic **output**

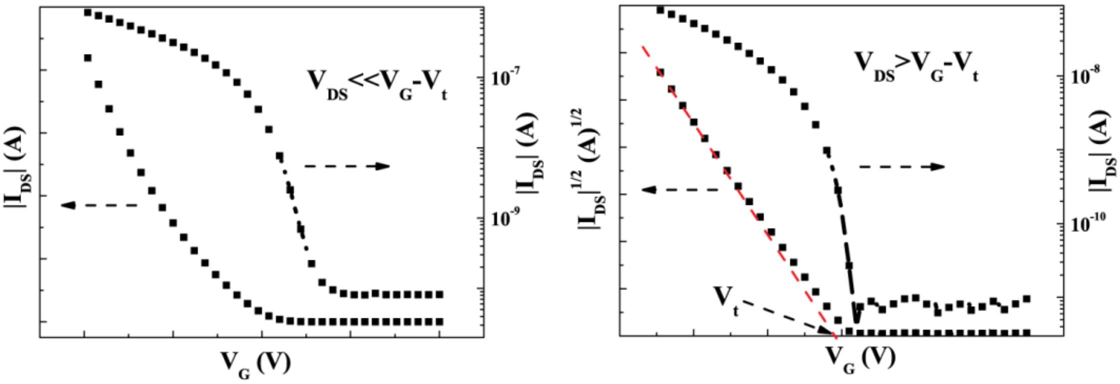

linear transfer **saturation transfer**

Figure 2.2 Working mechanism schematic of a bottom gate-bottom contact p-type TFT and its performance.

Figure 2.2 also shows the typical output (I_{DS}~V_{DS}) curve, the linear and saturation transfer (I_{DS}~V_G) curves of this p-type TFT. The transfer character can be described by:

$$I_{DS} = \begin{cases} \frac{W}{L}\mu C_i (V_G - V_t - \frac{V_{DS}}{2})V_{DS} & \mathrm{V_{DS}} << V_G - V \\ \frac{W}{2L}\mu C_i (V_G - V_t)^2 & \mathrm{V_{DS}} > V_G - V_t \end{cases},$$

where *W*, and *L* are the width and length of the channel, respectively. μ is the carrier mobility. C_i is the capacitance of the gate insulator. V_t is the threshold voltage of the device, which can be determined by the saturation transfer curve as shown in Figure 2.2.

The mobility μ, the threshold voltage V_t (the minimum V_G used to form the conducting channel) and the on/off ratio (the ratio of maximum and minimum I_{DS} in transfer curves) are the three most important parameters to present the performance of a TFT [21].

2.2 Functional TFTs

2.2.1 Introduction

A functional TFT is a functional device with the structure of TFTs. The functional device is a broad category covering many devices. These devices have been widely used in modern society for both large instruments and portable devices. Here we just talk about the functional devices which are either semiconductor devices such as diodes and transistors or integrated devices based on them. In terms of applications, functional devices can be divided into several categories:

- Memories. For example, capacitive memories for dynamic random access memory (DRAM) and floating gate transistors for flash memory [17].
- Light emitters. For example, light emitting field effect transistors (LEFETs) for flat panel display [3, 15].
- Photodetectors. For example, Si-based visible photodiodes and Ⅲ-Ⅴ elements-based infrared photodiodes for thermal imaging [3, 10, 16].
- Other functional devices such as biosensors, chemical sensors, gas sensors and so on [15].

Functional devices have been developed for long time and got glorious improvements. However, they always suffer from some disadvantages on cost and performance and the effort to search for their alternatives has never stopped [16, 17]. Functional TFTs benefit from their structures and attract more and more interest. For example, widely used LEDs need external circuits for device control and signal reading out. This requirement may increase the technical complexity and the device cost. As a comparison, a light emitting TFT can integrate the light emitting and the switching functionality in a single cell. This integration may give rise to remarkable improvement of devices performance and promising industrial prospect [31]. Regarding photodetectors, conventional photodetectors based on photodiodes suffer from the limited quantum efficiency and this parameter can be largely improved using TFT structure [32]. Furthermore, some reports show that the gate voltage in TFT photodetectors can be used to enhance or erase the photoresponse [18, 19]. In the application of memory, floating gate and ferroelectric transistors have already been used in modern flash memory and are being further improved [20, 33-37]. Besides, some novel light driving memories based on TFTs which show promising features such as multilevel storage ability have been proposed [38-43].

On the other hand, because of the strict processing conditions and small amount of conventional inorganic semiconductors, they offer limited choices for the materials that can be used in functional devices. Therefore, the rise of organic semiconductors since 1970s blooms the research of functional TFTs [15, 44]. High level synthetic chemistry supplies abundant organic semiconductors with various semiconductor properties. Moreover, The solution-processibility of some organic semiconductors makes them promising candidates for future low cost, roll to roll processible and flexible electronic devices [22]. Besides organic semiconductors, graphene and quantum dots have also attracted huge attention in functional TFTs research because of their extraordinary electronic properties (graphene) [45] and unique optoelectronic property derived from quantum size effect (quantum dots) [46]. Based on these materials or the hybrids of them, various functional TFTs have been fabricated such as visible photodetectors [47, 48], infrared photodetectors [49-51], flash memories [20, 33-37] and light driving memories [38-43]. These devices show not only impressive performance, but also valuable inspirations for future research.

2.2.2 Photodetectors Based on TFTs

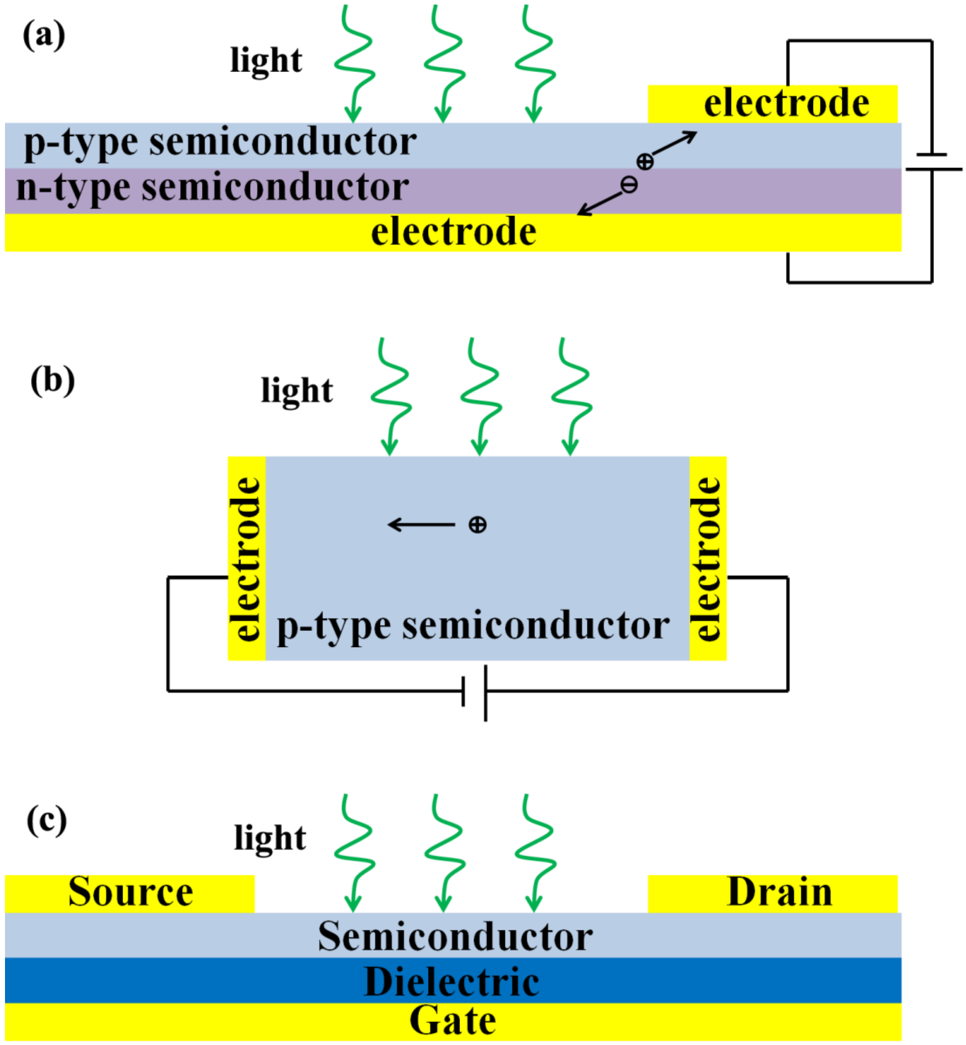

Figure 2.3 (a) Schematic of a typical photodiode and its working principle under illumination. (b) Schematic of a p-type photoconductor and its working principle under illumination. (c) Bottom gate-top contact phototransistor under illumination.

A photodetector is a device to sense the light through converting light signals into electric signals. Photodetectors are widely used in visible imaging for cameras, thermal imaging for military, diagnosis or remote monitor, optical fiber communication as laser receiver and others [3]. Photodetectors can be divided into two categories: photodiodes and photoconductors. Their typical structures and working process are shown in Figure 2.3a and b. It is easy to understand that photo-induced charge carriers contribute to the photocurrents of photodetectores.

In a photodiode, both holes and electrons attend the conduction and the external quantum efficiency (EQE, which is the ratio of photocurrent to photon incident on the device) is limited below 1. In a photoconductor, with one kind of carriers trapped, the other kind of carriers can circulate in channel for many times before recombination. As shown in Figure 2.3b with a p-type photoconductor as an example, this device may has gain larger than 100% thus higher sensitivity than a photodiode [32].

Figure 2.3c shows a photodetector with the structure of bottom gate-top contact TFTs. It can also be called a phototransistor. It is apparent that a phototransistor can be regarded as a photoconductor with an extra gate electrode. Both of photodiodes and photoconductors suffer from high noise current because of the conductivity of semiconductors [32, 52]. The gate voltage of a phototransistor can be used to switch the operation mode of device to minimize the noise current [10, 53]. Besides, it can also be used to tune the photoresponsivity and response time for better performance [18, 54, 55]. Moreover, with TFT structure, phototransistors are easier to be integrated into electronic circuit [16, 18, 19, 32, 53, 54, 56-58].

Under light illumination, the transfer curves of phototransistors will shift horizontally to high or low gate voltage direction. The direction depends on photo-excitation and charge carriers' injection conditions. For example, a phototransistor is fabricated based on p-type semiconductor. When it is placed under light illumination, photo-induced electrons will be trapped in these electron-trapping centers, with holes in the p-type conducting matrix. The transfer curve will shift to high gate voltage direction because of the p-doping effect, as shown in Figure 2.4a. The sampling response of this phototransistor, which is the channel current monitored under light illumination, is shown in Figure 2.4b.

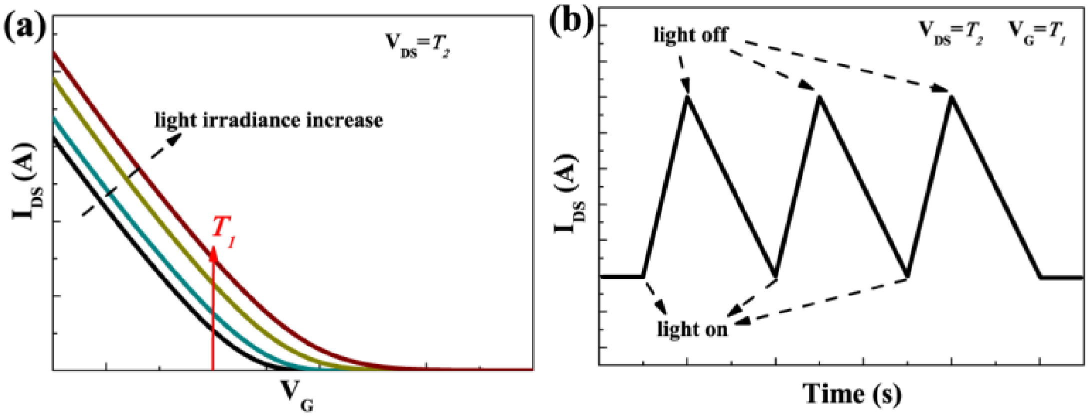

Figure 2.4 Photoresponse of p-type phototransistor with electron-trapping centers. (a) Transfer curves under light illumination. (b) Sampling curve with three on/off cycles of light.

Besides the common parameters of TFTs, there are two important figures of merit especially for phototransistors: photoresponsivity *R* and photoswitching ratio *P*. They are given by:

$$R = \frac{I_{ill} - I_{Dark}}{AE_e} = \frac{\Delta I_{DS}}{AE_e} \qquad 2\text{-}1$$

$$P = \frac{I_{ill} - I_{Dark}}{I_{Dark}} = \frac{\Delta I_{DS}}{I_{Dark}} \qquad 2\text{-}2$$

where the I_{ill} is the source-drain channel current under illumination, I_{Dark} is the channel current in dark, A is the channel area exposed under illumination and E_e is the light irradiance [9].

Table 2.1 Some phototransistors which make use of different kind of materials and sense wavelength in different regions.

Phototransistor	**Ultraviolet**	**Visible light**	**Infrared**
Organic	BPTT [59] P3HT [60] Spiro-DPSP [61] PY-4(THB) [55] Sexithiophene, Pentacene [62]	MEH-PPV [63, 64] HXS-1 [65] (Me-ABT) [58] J-Aggregated organic [66] P3HT, Pentacene [67] P3OT [68, 69] P3HT [60, 70] BAS-PPE [71] F8T2 [9] Pentacene, tetracene [72] Pentacene [57, 73, 74] Rubrene, tetracene [75]	squarilium dyes [76]
Inorganic	Graphene oxide [77] AlGaN [78]	MoS_2 [79] monolayer graphene [80] Si [81] Si nanowire [82] Ge nanowire [83]	Graphene [49, 56, 84, 85] Si nanowire [82]
Hybrids	ZnO nanoparticle-SWNT [86] TiO_2-P3HT [87, 88]	Graphene-PbS [50] 60PCBM:OC_1C_{10}PPV [89] MDMO-PPV-PCBM [90] $C_{59}N$@SWNTs [91] TiO_2-P3HT [47, 48] Graphene-TiO_2 [92] P3HT-IGZO [93] P3HT-PCBM [94] P3HT-F8BT [95] P3HT-dye [96]	Graphene-PbS-quantum dots [51]

Phototransistors are first invented by Dr. John N. Shive in 1950 at Bell Laboratory [97] and have undergone great development ever since. For example, visible light detection is important for many applications and silicon (Si) is the widely used material in this area. In 1984, N. M. Johnson et al. reported their phototransistor based on single crystal Si, which showed photoresponsivity ≥300A/W [81]. Recently in 2010, Arthus Zhang and his partners fabricated similar devices making use of Si nanowire. They successfully improved the photoresponsivity largely, which is up to 1×10^5 A/W at low temperature and weak irradiance [82]. Attempts on fabricating practical phototransistors never cease and some reported phototransistors making use of various materials are listed in Table 2.1. It is worthy of note that in the recent works, phototransistors based on organic materials take up a large proportion. In the meantime, phototransistors based on graphene and quantum dots are obtaining more and more attention.

2.2.3 Memories Based on TFTs

Memory technologies are of great importance because nowadays almost every electronic device needs its own memory for date recording and processing [15]. In fact, for computers, cell phones and many other types of equipments, the performances of their Random Access Memory (RAM) are the second crucial factors that will influences devices speed and capacity besides CPUs. Dramatic achievements have been attained in memory researches and they contribute largely to the miniaturization and optimization of electronic devices. Table 2.2 lists current mainstream memory technologies as well as some technologies in research. Some more features concerned can be found in literatures [17, 98].

Table 2.2 Some memory technologies industrialized or in research stage.

Features **Memory Principle**		**Volatility**	**Multilevel**	**Driver**	**Applications**
Capacitive couple memory		Yes	No	Electricity	Random Access Memory (RAM)
Transistor memory	**Floating gate transistor**	No	yes	Electricity	Flash Memory Read Only Memory (ROM)
	Ferroelectric transistor	No	No	Electricity	Flash Memory
Resistive memory		No	Research	Electricity	Demonstration
Phase change memory		No	Research	Laser	CD/DVD disk
Magnetoresistive memory		No	No	Magnetism	Hard Disk Drive (HDD)

It is well known that Hard Disk Drive (HDD) and flash memory are the mainstreams of nonvolatile memory. HDD, which makes use of magnetoresistance technology, is the first choice for the large capacity memory because of its high density and low cost advantages. Nevertheless, HDD suffers from slow accessing speed, high energy consumption and unstable operation and is being replacing by flash memory [17]. Flash memory is mainly fabricated based on floating gate transistors. It has good nonvolatility, low energy consumption and is easy to be integrated into electronic circuits. However, its endurance is unsatisfactory and the effort to increase the memory density through miniaturizing element cells is hindered by intrinsic limitations of its materials [17]. Therefore, various new materials including organic semiconductor and graphene have been used in the research of memories based on floating gate and ferroelectric transistors for improved performance [11, 20, 33-37, 99, 100].

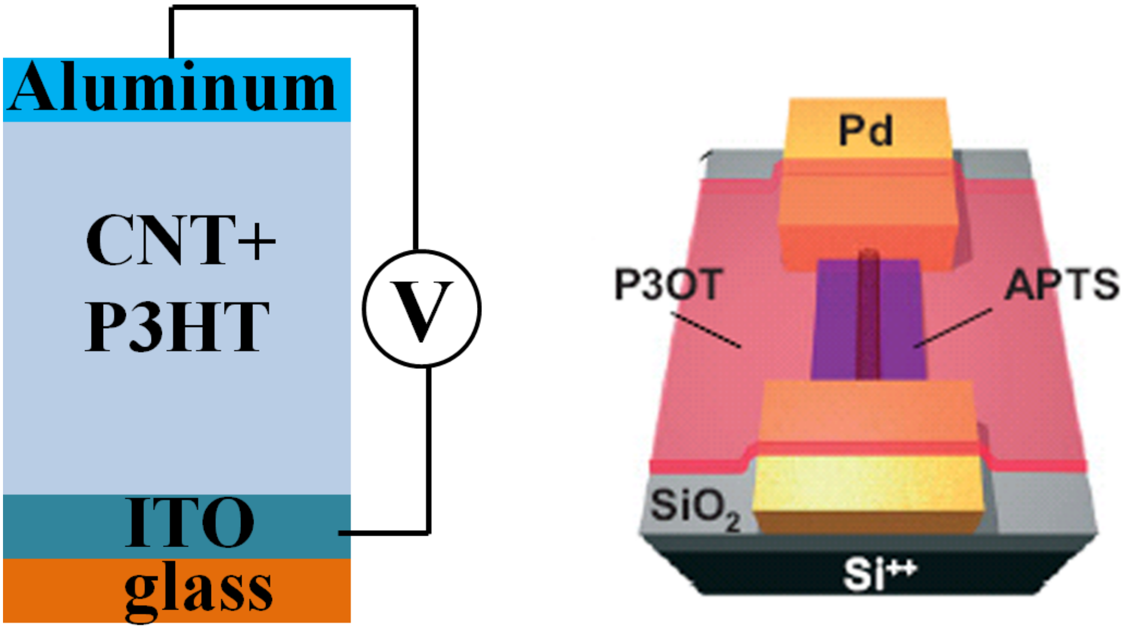

Figure 2.5 Left: electricity driving resistive memory based on hybrid carbon nanotube (CNT) and P3HT, conceived schematic from ref. [101]. Right: light driving TFT memory based on hybrid of carbon nanotube and P3OT, reproduced from ref. [41].

On the other hand, some novel memory devices have been proposed, such as the electricity driving resistive memories and the light driving TFT memories. An electricity driving resistive memory is comprised of a resistance switchable material with two terminal electrodes. Different resistive states can be switched by electric bias between the electrodes. A light driving TFT memory has the same structure as a phototransistor. It makes use of light illumination to change the resistive state of the conducting material to programme information. These excited states can retain for long term and be erased by the gate voltage. Figure 2.5 shows an electricity driving resistive memory and an light driving TFT memory. The Left figure is the conceived schematic of the resistive memory reported by Basudev Pradhan et al. in 2006 [101]. Their devices are fabricated based on the hybrids of carbon nanotube (CNT) and P3HT. This kind of resistive memory shows electrical bistability under voltage sweeping. Also in 2006, a light driving TFT memory based on CNT and P3OT, whose structure is shown in the right figure of Figure 2.5, was reported by Julien Borghetti et al. [41]. The channel resistance of the TFT decreases under visible illumination and is stable after light removed. Furthermore, the low resistance state can be erased by gate voltage.

It is worth noting that a light driving TFT memory can be regarded as a kind of resistive memory programmed with light illumination instead of electricity. In fact, the conventional floating gate transistor memories and ferroelectric transistor memories all make use of different resistive states of the conducting channel to record information. These states are switched by gate voltage. It is apparent that making use of light instead of electricity to be the programming method is helpful to lower the energy consumption. The TFT configuration makes the device facile to operate and integrate into electronic circuits. Besides, the variability of light intensity and wavelength facilitate multilevel storage, which is of large significance for high density memory. Some multilevel light driving TFT memories have already been reported [39, 40].

Compared with the bistable electrical property shown by rare materials [17], most semiconductors have optoelectronic properties. This point accommodates large potential of light driving memories research. It should be pointed out that the carries traps are crucial for the nonvolatile performance. This is why most reported light driving TFT memories are fabricated based on hybrid materials, including carbon nanotube-polymer [38, 40-42], organic-inorganic hybrids [42, 43] and others [39, 54]. One component in these hybrid systems is in charge of conducting current and the other is responsible for the trapping of photo-induced carriers. Their synergy gives rise to the nonvolatile memory effect.

2.3 Hybrid Materials

2.3.1 Introduction

It is well known that materials play critical roles in the performance of devices. Scientific community is always attempting to find or design perfect materials for certain applications. Unfortunately, every material shows trade-offs between different properties such as mechanical, durative, and functional properties. Therefore, combing different pristine materials to get hybrid materials with desired properties is an effective route for materials design and hybrid materials has attracted increasing attention, as shown in Figure 2.6.

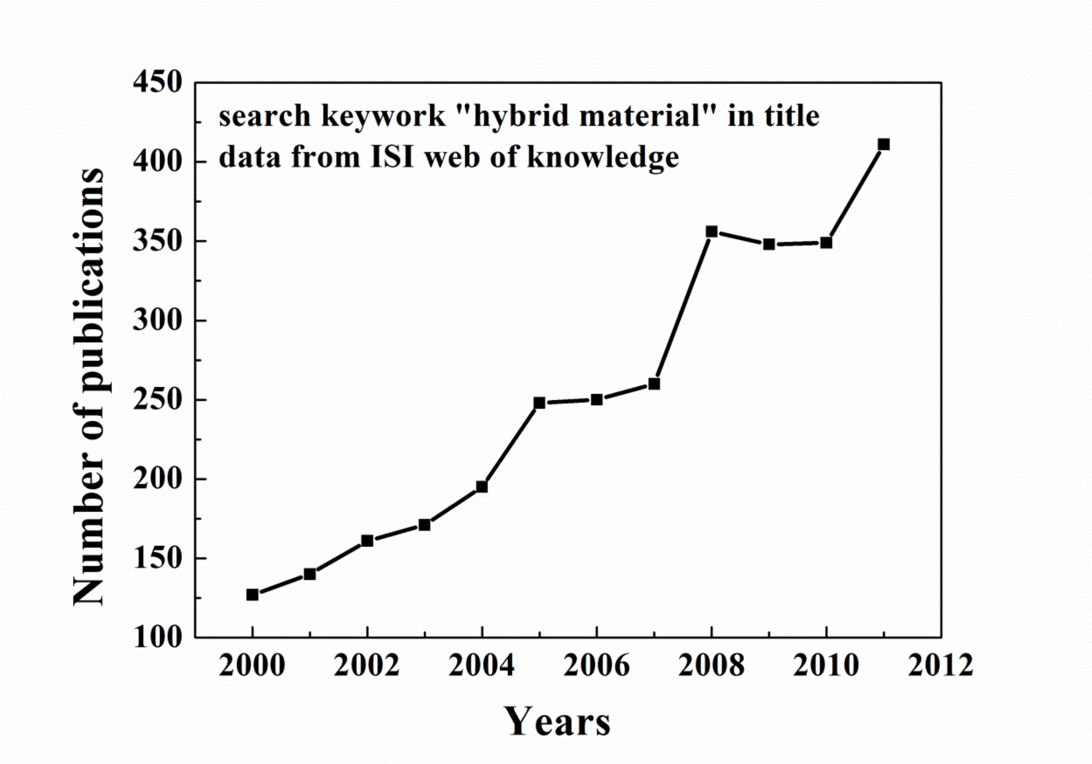

Figure 2.6 Publication amounts in recent eleven years about hybrid materials. Date from ISI Web of Knowledge with keyword “hybrid material” in title.

In fact, in ancient age people knew how to fabricate Adobe, which is a kind of hybrid material with straw mixed into clay to prevent easy cracking [27]. With the development of scientific scale, hybrid materials have developed from macro-mixtures to nanosize composites and then the molecular level complexes nowadays [28, 102]. The properties of hybrid materials certainly depend on the natures of their components, but the interactions of these components are also very important. In fact, many interesting functionalities of hybrid materials are derived from these interactions [102]. These functionalities can be used in many fields such as biology, chemistry and optoelectronics. Various functional devices including biosensors, photocatalysts, lasers and solar cells have been fabricated making use of various hybrid materials [27-30].

It is not easy to categorize hybrid materials because of their huge amount and wide range of features. Several classifications relying on dimensions of components, interaction of components or applications have been used to divide them [28, 102]. Here we just study the binary hybrid materials and define them to be the single systems that comprise two different components. Thus it is reasonable to categorize them into three classes generally through the components types.

- Organic-Organic (O-O) hybrid materials. Both of the components are organic materials. Organic materials have good compatibility to each other and most of this kind of hybrid materials is solution-processible. The organic solar cell, which is the scientific hotspot now, mostly makes use of O-O materials such as the classic PCBM-P3HT system [103]. Besides, the O-O materials also obtain attention in TFTs area. Junshi Soeda et al. and Richard Hamilton et al. respectively reported their TFTs with improved performance based on blends of organic materials [104, 105]. Maxim Shkuno et al. fabricated ambipolar transistors using hybrids of p-type and n-type organic semiconductor [106]. Some functional TFTs such as phototransistors using O-O materials have also been reported [89, 90].
- Inorganic-Inorganic (I-I) hybrid materials. This kind of hybrid materials has already been used in mass production. Last generation transparent electrode, the fluorinated tin oxide (FTO) and current used Indium tin oxide (ITO) can be

regarded as I-I materials. There are also many other I-I hybrid materials such as doping semiconductors and photoluminescence materials [107]. What have aroused large research interest recently in this area are the graphene-inorganic hybrid materials. This kind of material appears with the rise of graphene and shows excellent properties and promising application prospect [108, 109]. It will be discussed later in detail.

- Organic-Inorganic (O-I) hybrid materials. O-I materials is the mainstream of the hybrid materials research. Pedro Gomez-Romero in his review paper divides this kind of materials into three categories: organic-inorganic (O-I) materials, inorganic-organic (I-O) materials and nanocomposites [102]. In this classification, O-I and I-O materials are the molecular scale hybridization of components with organic and inorganic components as host matrix, respectively. And the nanocomposites are the hybrid systems with inorganic nanoparticles dispersed in organic matrixes.

2.3.2 **Organic-Inorganic Hybrid Materials**

Here the organic-inorganic hybrid (O-I) materials are defined broadly as the composites comprising organic and inorganic components. Though some O-I materials, for example the Maya blue pigments, have already been used in human society for thousands of years [28], it is believed that industrial products based on O-I materials had not been developed until 1940s [110]. The term “hybrid” was first proposed in 1990s with the development of molecular chemistry [111].

Table 2.3 Comparison of properties of some organic and inorganic materials [112].

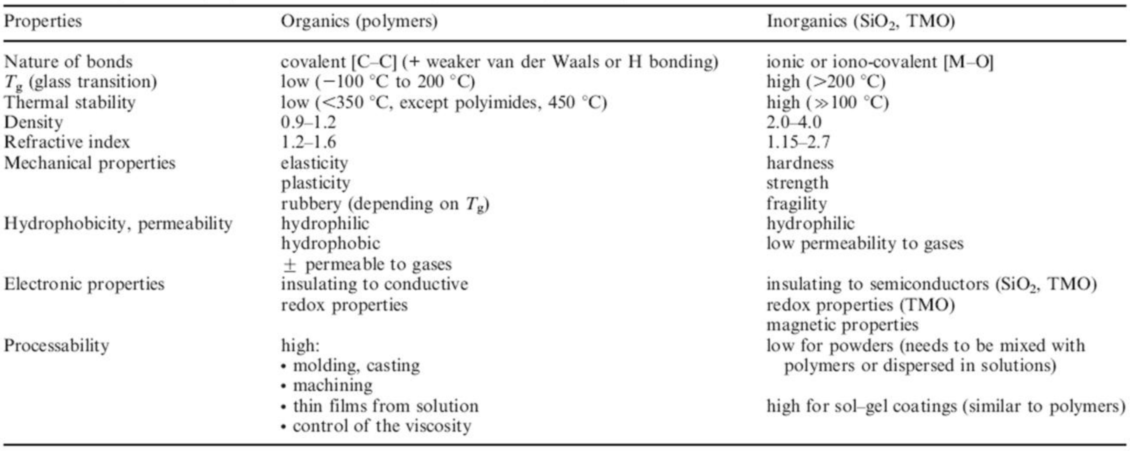

Properties	Organics (polymers)	Inorganics (SiO_2, TMO)
Nature of bonds	covalent [C–C] (+ weaker van der Waals or H bonding)	ionic or iono-covalent [M–O]
T_g (glass transition)	low (−100 °C to 200 °C)	high (>200 °C)
Thermal stability	low (<350 °C, except polyimides, 450 °C)	high ($\gg$100 °C)
Density	0.9–1.2	2.0–4.0
Refractive index	1.2–1.6	1.15–2.7
Mechanical properties	elasticity plasticity rubbery (depending on T_g)	hardness strength fragility
Hydrophobicity, permeability	hydrophilic hydrophobic ± permeable to gases	hydrophilic low permeability to gases
Electronic properties	insulating to conductive redox properties	insulating to semiconductors (SiO_2, TMO) redox properties (TMO) magnetic properties
Processability	high: • molding, casting • machining • thin films from solution • control of the viscosity	low for powders (needs to be mixed with polymers or dispersed in solutions) high for sol–gel coatings (similar to polymers)

O-I materials earn huge interest because of their great potential in material design. It is well know that both single organic and inorganic materials have their advantages as apparent as their disadvantage. The properties of some organic and inorganic materials are shown in Table 2.3 [112]. It is worth noting that the properties of organic and inorganic are complementary to each other. Therefore, it is reasonable to compensate their disadvantages through mixing them together.

2.3.2.1 **Synergistic Effects in O-I Materials and Their Applications**

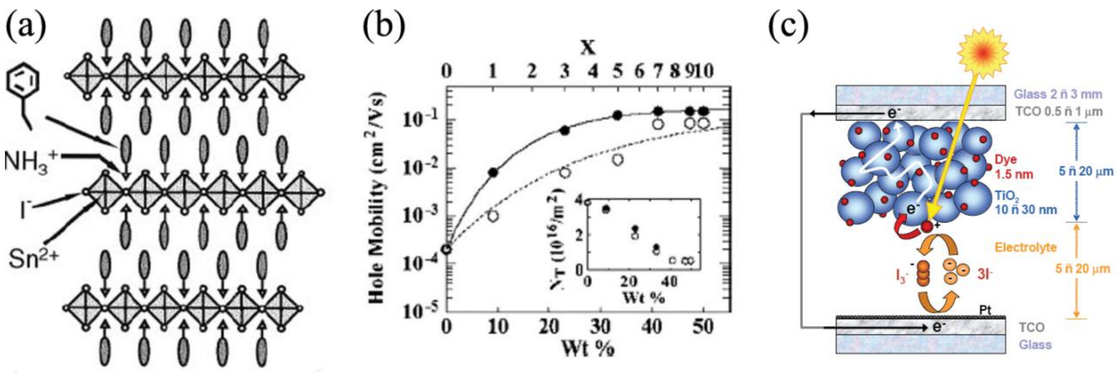

Figure 2.7 (a) Perovskit structure of $(C_6H_5C_2H_4NH_3)_2SnI_4$ hybrid film [113]. (b) Enhancement of hole mobility in MEH-PPV by adding ZnO tetrapods. The Wt% is the mass ratio of ZnO tetrapods in hybrid system [114]. (c) Structure and working principle of dye sensitized solar cell. The big blue spheres represent TiO_2 nanoparticles and the small red spheres represent dye [115].

One of the advantages of hybrid materials is that they may show the expected properties which are come from their components. For example, hard mechanical property of inorganic induces complicated processing but many organics are soluble. Therefore dispersing inorganic into organic matrixes to realize solution-processibility of inorganic components without sacrificing their excellent electronic properties is a feasible way. C. R. Kagan et al. reported their high performance TFT based on the perovskite $(C_6H_5C_2H_4NH_3)_2SnI_4$ hybrid film [113]. The structure of this hybrid film is shown in Figure 2.7a. It is synthesized by organic component $C_6H_5C_2H_4NH_2HI$ and inorganic component SnI_2. The final hybrid materials are solution-processible with high mobility of SnI_2 reserved.

Another advantage of hybrid materials is that the components therein may enhance the properties of their counterpart. For example, Zong-Xiang Xu et al. found that adding ZnO tetrapods into polymer MEH-PPV matrix would induce the increase of hole mobility of the polymer matrix, as shown in Figure 2.7b [114]. This exceptional phenomenon is also found in our research and is attributed to the nanoparticle inducing self-assembly of polymer [88].

Besides combining or improving of the intrinsic properties of the components, hybrid materials may show new functional properties that don't belong to any single component, which derive from the synergistic effects of their components. Dye sensitized solar cell (DSSC) is a classical example of this kind of effect. The core of a DSSC is its photoanode which commonly is a hybrid film of TiO_2 nanoparticles and organic dye. The dye adhering to TiO_2 harvests light with TiO_2 film accepts and conducts electrons. The synergistic effect is the photovoltaic phenomenon, as shown in Figure 2.7c [115, 116].

Some O-I materials and their applications are list in Table 2.4 to give a glance into this area. It should be pointed out that the interface of different components in an O-I material plays an important role in the synergistic effect. Many applications of O-I materials especially the optoelectronic devices such as photodetectors and photovoltaic devices benefit from the interface, where the photo-induced excitons dissociate and the charge carriers generate. This mechanism will be harnessed very much in our research.

Table 2.4 Some O-I materials, their synergistic effect and applications.

Organic	**Inorganic**	**Synergy effect**	**Application**
PVA-*g*-P(4-VP)	Silica sol	Improved performance	Biosensor [117]
P3HT	TiO_2 nanocrystal	Visble-UV sensitivity	Phototransistor [47, 48]
Dye	TiO_2 nanocrystal	Photovoltaic effect	Solar cell [116]
MEH-PPV	TiO_2 nanocrystal	Photovoltaic effect	Solar cell [118]
Polyaniline	CdS particles	Proton uptaking	Electrochromic [119]
$C_6H_5C_2H_4NH_2HI$	SnI_2	Intrinsic properties	Improved TFT [113]
MEH-PPV	ZnO	Unclear	Increased mobility [114]
P3HT	TiO_2 nanorods	Self-assembling	Increased mobility [88]
Polypyrrole	MnO_2	Active of MnO2	Li-battery [120]
polyaniline	V_2O_5	Mechanical support	Li-battery [121]
TPAPAM	Graphene	Redox reaction	Memory [122]
Polystyrene	Graphene	Reinforcement	Improved conductivity [123]

2.3.2.2 **Synthesis and Processing**

The bloom of O-I materials should be largely ascribed to the progress of the synthesis techniques. The largely developments of soft chemistry and physical deposition techniques make it possible to tailor hybrid materials for expected properties. The synthesis techniques of O-I materials can be divided into two categories generally:

- Physical techniques. Thermal evaporation is an effective method to deposit O-I material films especially for small molecule organics that are poorly soluble, as well as some O-I materials that require to be deposited under vacuum condition. High quality of hybrid films such as Alq-MgF_2, CuPc-TiO_x and $(C_6H_5C_2H_4\text{-}NH_3)_2PbI_4$ perovskite hybrid films have been successfully deposited by this way [26, 124].

- Chemical techniques. They are the predominant techniques used to synthesize O-I materials. Chemical techniques belong to a category with broad content. This category includes sol-gel method, hydrothermal synthesis, integrative synthesis, solution mixing, Langmuir-Blodgett assembling, self-assembling, electrostatic assembling and so on. These methods can be used to obtain O-I materials with scales from hybridized layer by layer perovskite structure to macroscopic mixture [26-29].

Besides synthesis, processing of O-I materials is another important step toward applications. The physical techniques are processing methods themselves, which deposit hybrid films directly. On the other hand, solution-processiblity is a remarkable advantage of the O-I materials which are synthesized by chemical techniques. Various processing methods have been developed, such as ink-jet printing, spray, electro-spinning, fiber extrusion and pulling, dip coating, doctor blading, spin coating, and drop casting [26, 27]. Among them, the spin coating and drop casting are two important methods to deposit thin films and widely used in the fabrications of various devices such as TFTs [125] and solar cells [118]. The common advantages of spin coating and drop casting are their easy operation and compatibility with large scale processing, which have promising applications in low cost industrial production. Besides, spin coating can result in films that are very thin, uniform and smooth.

Meanwhile, drop casting allows the self-assembly process which may improve properties of films [26, 125]. These features are of great significance in our scientific research reported in the thesis.

2.3.3 **Graphene-Inorganic Hybrid Materials**

2.3.3.1 **Overview of Graphene**

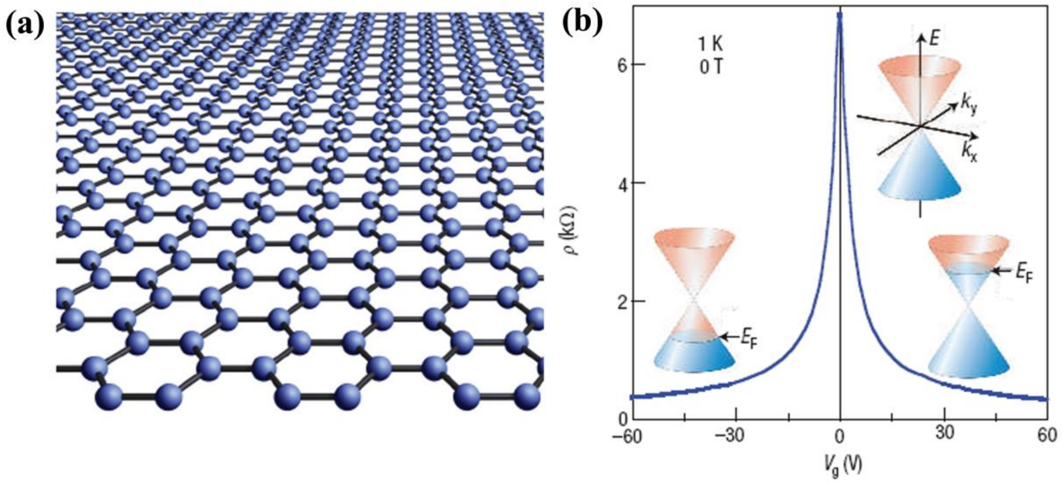

Figure 2.8 (a) Schematic of graphene [126] (b) Ambipolar electric field effect in single layer graphene. The insets show the conical low-energy spectrum. Fermi level E_F under different gate voltage is indicated [45].

Graphene is a two-dimensional crystal with carbon atoms arranged in a hexagonal lattice (Figure 2.8a) which was first reported by K. S. Novoselov et al. in 2004 [127]. Graphene has received intense interest for its unique properties, some of which are summarized as follows:

- Electronic properties. Graphene is a kind of zero bandgap semimetal with conduction band and valence band touch at a point. It shows ambipolar transport feature with massless Fermions behavior and ballistic transport of charge carriers (Figure 2.8b) [45, 126]. The charge carrier mobility in graphene is up to 10^5 cm^2/Vs at ambient temperature [128, 129] and 10^6 cm^2/Vs at low temperatures [130]. The high mobility makes graphene promising candidate in applications such as high speed TFTs [24, 25, 131]. In fact, even with modest mobility around 10^3 cm^2/Vs, high speed TFT with cut-off frequency up to 100GHz has been obtained [25].

- Conductivity at neutrality point. Graphene retain its conductivity of the order of $4e^2/h$, where e is the electron charge and h is the Plank constant, within the limit of nominally zero carrier concentration near the neutrality point. The aforementioned remarkable mobility and this high conductivity with zero carrier concentration make it suitable to be used as electrodes [126, 132].
- Optical properties. Single layer graphene shows poor absorption to light from infrared to UV [133]. It is proven that in infrared region the absorbance of single layer graphene is ~2.3% [134-136]. This value increases with the increase of light frequency but still be less than 3% in visible region [137]. At UV of ~280nm, graphene has an absorption peak with absorbance of ~10% due to the presence of the van Hove singularities at the zone edge [138, 139]. With fewer wavelengths the absorbance decreases sharply. This means that graphene is almost transparent in wide wavelength range. The high conductivity and transparent optical

properties of graphene make it a promising candidate for transparent electrode in optoelectronic devices [132, 140]. Chanwook Jeong et al. reported their ultratransparent polycrystalline graphene electrodes with improved sheet resistance [141]. In earlier time Wu et al. fabricated OLED with solution-processed graphene as transparent conductor [142].

- Mechanical properties. Defect-free graphene is proven to have a Yong's modulus of 1YPa [143, 144]. As more available graphene, the chemically derived graphene with defects still has the value of 0.25 Ypa and simultaneously good flexibility [145]. With these properties, graphene can be used to support or reinforce the other component in a hybrid system.
- Thermal properties. Suspended single layer Graphene has a thermal conductivity of ~5000W/mK at room temperature [146]. The excellent thermal property makes graphene stable when it is used as substrates, electrodes or active materials in some applications such as photodetectors and solar cells.

These unique properties make graphene attractive both in scientific research and applications. But in some occasions these properties may become its weaknesses. For example, when graphene is used as the active layer in TFTs, the high conductivity at neutrality point will induce high off current and low on/off ratio which will suppress the switching performance of TFTs [126]. Besides, the low absorbance of graphene makes it unable to harvest light energy and limits the application of graphene in optoelectronic devices. Considering aforementioned discussions about hybrid materials, hybrid materials based on graphene is a reasonable choice for sophisticated utilization of graphene in functional devices.

Obviously there are two kinds of hybrid materials based on graphene: graphene-organic and graphene-inorganic hybrids. Several excellent review papers have been published on this topic [109, 147-149]. Here graphene-inorganic hybrid materials will be introduced because of its relevance to our research.

2.3.3.2 **Preparations of Graphene-Inorganic Hybrid Materials.**

There are abundant methods to prepare graphene-inorganic hybrid materials. According to when the components are synthesized, these methods can be divided into two categories:

- Ex situ hybridization. In this category, both graphene and inorganic components are pre-synthesized before they are hybridized. The hybridization can be realized by noncovalent or covalent interactions. Sometimes surface modifications of the components are needed for their combinations [109, 147]. Both the depositing inorganic on the surface of graphene layer and the mixing of graphene and inorganic are included in this category. The inorganic components can be metals, metal oxides or other materials. Such as the reported Au [150, 151], MnO_2 [152], Fe_3O_4 [153, 154], CdSe [155, 156] and PbS [51].

- In situ synthesis. Graphene and inorganic components are synthesized simultaneously in the hybridization process. Compared with ex situ hybridization, this approach can give rise to uniform distribution of the inorganic components on graphene [109, 147]. In situ synthesis is a widely used route toward graphene-inorganic hybrids and a variety of methods are included in this category, both physical and chemical. Physical deposition such as thermal evaporation has been reported to deposit Au [157], Al [158], and PbS [50] nanoparticles on surface of graphenes. Filtered Cathodic Vacuum Arc (FCAV) deposition is another physical method to deposit oxides such as ZnO on graphene for hybrid materials [159]. Chemical synthesis is predominant in the in situ synthesis, including sol-gel methods, hydrothermal methods, chemical deposition, electrochemical deposition and self-assembling methods. By chemical synthesis methods, many oxides and semiconductors nanoparticles such as TiO_2 [160], MnO_2 [161], ZnO [162, 163], and CdS [164, 165] have been hybridized with graphene. Graphene-metal particles hybrids also can be obtained using chemical ways, such as the graphene-Au [166], grahene-Pd [167] and graphene-Ag [168] hybrids.

2.3.3.3 **Applications of Graphene-Inorganic Hybrid Materials**

It is impossible and unnecessary to list all graphene-inorganic hybrid materials here. In fact, it is of more significance to classify them according to their applications and investigate their synergistic effects derived from their interactions. The high stiffness, large surface and high thermal conductivity of graphene make it suitable to be support material in a hybrid system. And the electronic properties of graphene and the intrinsic properties of the inorganic component will decide the functionality of the hybrid system and the application of the device based on it.

Table 2.5 The roles and synergies of components in some graphene-inorganic hybrid materials and the applications of these hybrid materials.

Synergy	**Role of graphene**	**Role of inorganic**	**Application**	**Ref.**
Excitons dissociation in interface	conducting media	Light harvester	photodetector	[50, 51, 155, 162]
	conducting media	Light harvester	Solar cell	[164, 169]
Charges transport through interface	conducting media	conducting media	DSSC	[170-172]
	conducting media	Sensing centre	Gas/biosensor	[173, 174]
	Large surface area; conducting media	catalyzer	Electrocatalysis; photocatalysis	[175-177]
	High stiffness; Large surface area	cathode	Li batteries	[178, 179]
Decreased aggregation of graphene	anode	Intercalateors	Li batteries	[180, 181]
	High capacitance	High capacitance; stablizer	supercapacitor	[161, 182]

The interfaces of graphene and inorganic components are crucial to their synergistic effects because the interfaces are the sites where charge transfer and excitons dissociation happen. In some applications of graphene-inorganic hybrid materials, the involved properties of each component and synergistic effects of them are summarized in Table 2.5. In fact, both the excitons dissociation and charges transport behaviors can be ascribed to the high mobility in graphene which will facilitate the charge carrier injections. Take the dye sensitized solar cell (DSSC) as an example, the DSSCs comprising graphene as conducting layer show better performance than the devices without it, because the photo-induced electrons trend to inject into graphene and transport away from recombination centers very fast. This process will increase charge separation in the solar cell [170-172].

2.3.4 **Functional TFTs Based on Hybrid Materials**

As the organic semiconductors are regarded as the key to solve the performance and cost bottlenecks faced by the current silicon based electronic industry, large effort has been devoted into the synthesis of new organic semiconductors for future miniaturized, flexible, low cost, and even transparent electronic devices [22, 183, 184]. The achievements of the effort surely are great. For example, the field effect mobility of some organic semiconductor has been improved up to 5 cm^2/Vs, which is superior to amorphous silicon [185]. The development of organic semiconductors offers more potential for hybrid materials. On the other hand, though the boom of organic semiconductors makes great contribution to functional TFTs, in this area the hybrid materials still show apparent advantages. Taking the photo-excitation process as an example, hybrid materials show advantages in the application of optoelectronics. It is more difficult to obtain high quantum efficiency in single semiconductor than hybrid materials, because the interfaces in hybrid materials can supply the sites for excitons to dissociate, which are rare in single semiconductor. To our best knowledge, the highest photoresponsivity of phototransistors based on single organic semiconductor is ~1.2×10^4A/W with an elaborately synthesized organic material [58]. The widely investigated polymer P3HT have been used to fabricated phototransistor and shows modest photoresponsivity of ~250 A/W [70]. But in our research, the phototransistor based on the P3HT-PbS quantum dots hybrid materials shows photoresponsivity up to 2×10^4 A/W in infrared region.

2.3.4.1 **Phototransistors based on hybrid materials**

The phototransistors based on hybrid materials have never been paid enough attention until 2006. In that year, N. Marjanovic et al. and R. M. Meixner et al. reported their phototransistors making use of MDMO-PPV/PCBM [90] and dye/P3HT [96] blends, respectively. R. M. Meixner et al. illustrated that their devices can sense light wavelength selectively through choosing different dye as light harvester. Some other organic blends such as PCBM/OC_1C_{10}PPV [89], P3HT/PCBM [94] and P3HT/F8BT [95] have been used in phototransistors later. They all used p- and n-type semiconductors as components simultaneously in blends to ensure the dissociation of photo-induced excitons, which lead to photocurrent thus the photoresponse. At the same time, the organic-inorganic hybrid materials such as P3HT-TiO_2 nanoparticle and P3HT-indium gallium zinc oxide hybrid thin films have been introduced into phototransistors and show moderate performance [47, 48, 88, 93]. The advantages of using inorganic wide bandgap semiconductors is that, besides absorbing light with short wavelength, the high mobility in inorganic semiconductors and the distinct energy level structures of organic and inorganic components are supposed to give rise to improved exictons dissociation, thus larger photoresponse. Furthermore, in our research of P3HT/TiO_2 nanorods hybrid system, it is proven that TiO_2 nanorods can improve the hole mobility in P3HT matrix, which can induce better photoresponse [88].

Because of the excellent electronic properties of carbon nanotube (CNT) and graphene, the hybrid materials with any of them as components have also been used in phototransistors. The group of Professor Xuefeng Guo has reported their phototransistors making use of single-walled carbon nanotube/ZnO nanopraticles [86] and graphene/PbS quantum dots [50] hybrid materials. In these devices, carbon nanotube and graphene are used as conducting medias with nanoparicles used as light harvesters. This kind of combination takes advantage of the good electronic properties of CNT or graphene and the tailored optical properties of inorganic nanoparticles perfectly. These two kinds of devices show high photoresponsivity up to ~3×10^5 A/W under ultraviolet and ~3×10^3 A/W under infrared respectively. Most recently, similar hybrid phototransistor with PbS quantum dots deposited on the surface of graphene has been fabricated, whose photoresponsivity reaches up to 5×10^7 A/W. This is the highest value reported until now [51].

2.3.4.2 **Memories Based on Hybrid Materials with TFT Structure**

Conventional memories based on TFT structure comprise floating gate and ferroelectric transistor memories. Making use of hybrid materials in this kind of device is part of the tide of memories. Some groups have reported their works on organic floating gate transistor memories, in which polymer insulator films are used as tunnel layers and Au particles are embedded into these layers as floating gate materials [20, 33, 37]. These hybrid films comprising organic insulators and Au particles are solution-processible, therefore flexible devices can be obtained [20]. On the other hand, inorganic materials still have advantages in performance. Inorganic-inorganic hybrid film with high-*k* HfO_2 as the matrix comprising Au nanoparticles has been used in floating gate transistor memory which shows low operation voltage, long term retention and good stress endurance [36]. Similar device using high-*k* HfAlO/carbon nanotube hybrid film has been reported as well [34]. Besides, hybrid system of ZnO nanowire and $BaTiO_3$ ferroelectric nanoparitcles has been reported to be used in ferroelectric transistor memory. This memory device shows large modulation, long term retention and multilevel memory storage ability [35].

Different from the conventional transistor memories which are driven by electricity, recently another kind of transistor memory driven by light has been proposed. In this kind of memory, the channel resistance can be tuned by light illumination. Different resistive state retains for long time and can be erased by gate voltage. Therefore, light illumination and gate voltage can be used as programming and erasing methods, respectively. It is obvious that photo-excitation is essential in the programming process, which is one advantage of using hybrid materials as addressed above. The hybrid systems with carbon nanotube coated by polymer such as P3OT or PmPV have been used in this kind of light driving memory [38]. In those devices, the underlying carbon nanotube conducts the currents and the polymers serve as the light harvesters. The resistance of carbon nanotubes can be changed by the light illumination through the optoelectronic effect of polymers and retains for long time. The wavelength of driving light is dependent on the polymer components. Same phenomenon has been reported by other groups [40, 41]. Some similar devices have also been reported with polymer-quantum dots hybrid materials. The group of Kung-Hwa Wei showed their light driving transistor memories with P3HT-CdSe quantum dots and P3HT-CdSe/ZnSe core/shell quantum dots hybrid films as active layers [42, 43]. P3HT films are used as conducting matrixes and the CdSe quantum dots with surface ligand or ZnSe shell trap the photo-induced charge carriers. Light driving memories based on TFTs have the virtues of low energy consumption, high scalability and multilevel storage ability.

The extraordinary properties of hybrid materials support their widely application in functional TFTs. Until now considerable effort have been devoted to this topic and many excellent devices have been fabricated, such as the light emitting TFT based on

T5/P13 organic blends films [87, 186] and the chemical sensor based on blends of 6TPPT6 and HO6OPT [187]. This thesis is focusing on phototransistors and memories based on hybrid materials.

2.4 Summary

Nowadays, functional devices such as various sensors, memories and light emitters are popularly used in the information society. Their wide application promotes the research for high performance, low cost, miniaturized, flexible and even transparent functional devices. Therein, accompanying the upsurge of organic TFTs, functional devices based on TFTs are attracting increasing attention for their advantages in both performance and structure. Abundant organic semiconductors with various electronic properties accommodate plenty of choices of materials for functional TFTs.

Organic-inorganic hybrid materials can combine the high mobility and optical properties of inorganic components and the solution-processibility of organic components together into single systems. Moreover, the interfaces of different components in the hybrid systems can facilitate the charge transfer between them. This kind of exceptional synergistic effect is of high significance especially for optoelectronic devices such as phototransistors, light driving memories, etc.

Hybrid materials based on graphene is another kind of promising candidate material for functional TFTs. Graphene have extraordinary electronic properties which are overwhelming common organic and inorganic materials. Various functional TFTs devices with outstanding performances have been fabricated based on the hybrid materials comprising grapheme.

In our research, phototransistors and light driving memories based on the hybrid materials are demonstrated. The physical principles of the devices are systematically studied, which provides guidelines for further development.

Chapter 3 P3HT-TiO_2 Nanorods Hybrid Films with Enhanced Hole Mobility and Their Application in Ultraviolet Photodetectors

3.1 Introduction

Organic electronics have attracted much attention recently due to many advantages over inorganic semiconductor devices, including low cost, solution-processability, flexibility and environmental friendliness [22, 188]. Organic-inorganic nano-composites are one type of the advanced materials for organic devices because of the expected synergy between the organic and inorganic components, leading potentially to new physical properties of the composites and various applications in devices, including solar cells [189-193], phototransistors [47, 48, 194], memories [43] and sensors [195]. The composites of a conjugated polymer such as P3HT and inorganic nanoparticles, such as ZnO, TiO_2 or CdSe, have been used in organic solar cells and gratifying power conversion efficiency up to 3.8% are obtained [189-193]. Phototransistors using poly(3-hexylthiophene) (P3HT) and TiO_2 hybrid film as the active layer was also reported before [47, 48]. These devices especially the hybrid photovoltaic devices try to make use of the high charge carrier mobility of the inorganic component and the negative influence on the counterpart conjugated polymer caused by the inorganic component is often ignored.

Carrier mobility is the most important parameter for a semiconductor and dominates the performance of most semiconductor devices. However, organic semiconductors normally show much lower carrier mobility than their inorganic counterparts, which is a drawback for their applications in electronic devices, especially transistors and solar cells. Poly(3-hexylthiophene) (P3HT) is the most intensively studied semiconducting polymer widely used in both organic thin film transistors (OTFT) and solar cells due to its relatively high field-effect mobility (up to 0.1 cm^2/Vs) , which is close to the value of amorphous silicon film [31]. It has been found that the microstructure in P3HT is critically affected by regioregularity and processing conditions, resulting in the variation of field effect mobility by several orders of magnitude [196, 197]. Therefore various techniques have been used to improve the carrier mobility of P3HT by controlling the self-assembly process in the polymer films, such as choosing appropriate solvent [196, 198, 199], surface modification of the substrate [197, 200], deposition method [201, 202], and annealing conditions [203, 204]. The key point of these methods is to enhance the crystallinity of conjugated polymer and optimize the orientation of molecules to a preferential direction.

It is not difficult to understand that mixing some distinctive materials into conjugated polymer may deteriorate the crystallinity and lead to more localized energy states in the semi-crystalline polymer film, which will all induce the degradation of charge carrier mobility in the conjugated polymer [48, 205]. For example, S. M. Mok et al. reported that the hole mobility in the composite film of TiO_2 nanoparticles and P3HT decreases with the increase in the weight ratio of TiO_2 [48]. Therefore it will be fascinating to see the excellent property of every single component being kept or even elevated in the hybrid materials. In fact, in the research of organic semiconductor, besides the improved functional performance of hybrid materials, the enhancement of the carrier mobility of conjugated polymer means much to its applications.

To our best knowledge, the only paper that addressed the enhancement of hole mobility in P3HT-based composite films is reported by M. D. McGehee et al [206]. The hole mobility can be enhanced by a factor of 20 by infiltrating P3HT into straight nanopores of anodic alumnia due to the alignment of polymer chain along the charge transport direction, which demonstrates a feasible method of increasing the carrier mobility in the composite films by optimizing the coupling between the semiconducting polymer and inorganic nano-materials.

In this chapter, we illuminate that composite films of conjugated polymer P3HT and TiO_2 nanorods modified with pyridine show double even triple hole mobility of pristine P3HT film, which can be attributed to the improvement of the crystallinity of P3HT and the optimized orientation of polymer chains in the composite films induced by the nanorods. Through the comparison of different types of nanoparticles, it is confirmed that the rod-like shape and the surface modifier (pyridine ligand) both play important roles on the crystallinity and hole mobility in P3HT matrix.

3.2 Experimental

3.2.1 Materials

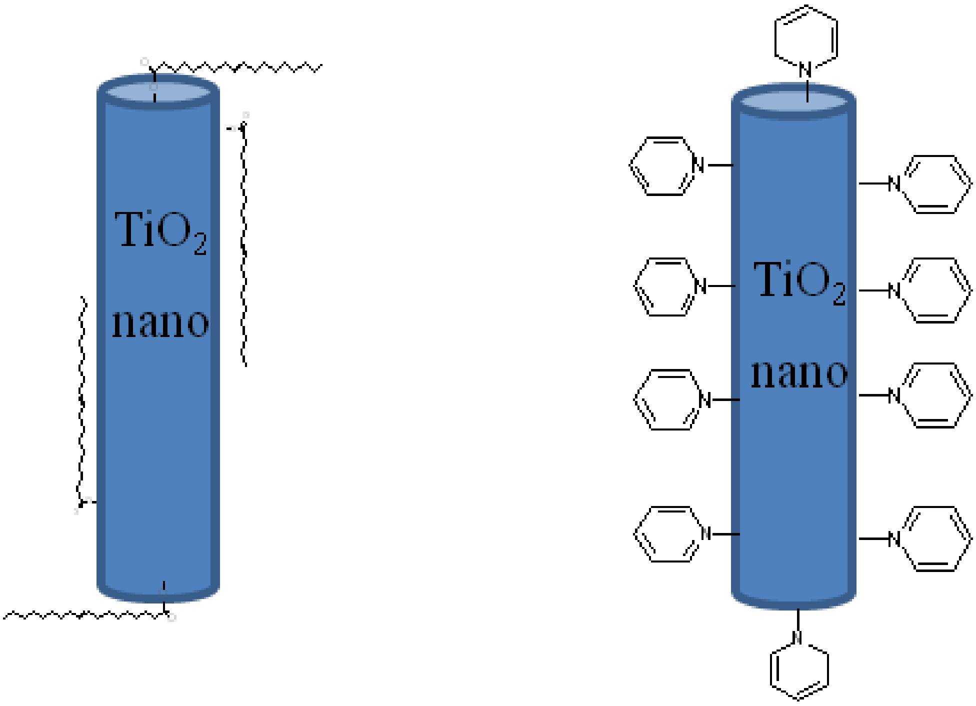

Figure 3.1 Left: schematic illustration of nanorods modified with oleic acid; right: schematic illustration of nanorods modified with pyridine.

Poly(3-hexylthiophene) (P3HT): Regioregular P3HT (4002-EE, regioregularity: 90 ~ 93 %, molecular weight: 50,000; Sepioilid^{TM} P200, regioregularity: 98 %, molecular weight: 25,000) was purchased from Rieke Metals without further purification.

Tatiana (TiO_2) nanocrystallites: Four types of TiO_2 nanocrystallites modified with oleic acid and pyridine, including (a) 3×10nm^2 nanorods (average diameter = 3nm;

average length = 10nm), (b) $3\times20nm^2$ nanorods (average diameter = 3nm; average length = 20nm), (c) 2nm TiO_2 nanodots (average diameter = 2nm), and (d) 5nm TiO_2 nanodots (average diameter = 5nm), were synthesized by nonhydrolytic method [207]. TiO_2 nanoparticles without surface modification, including rutile TiO_2 nanorod with a size of 5nm (diameter)×20nm (length), anatase TiO_2 nanodots with a diameter of 10nm, and TiO_2 nanoparticles with the size between 10~100nm, were purchased from Sigma-Aldrich and used in composite films for comparison. The schematic illustrations of nanorod with different surface ligand are shown in Figure 3.1.

Ligand exchange: Ligand exchange of oleic acid on TiO_2 nanoparticles to pyridine was carried out by the following method. Firstly, the TiO_2 colloidal toluene solution was mixed with ethanol with a volume ratio of 1:1. After centrifugation, the supernatant liquor was removed. Then, the white precipitate was re-dispersed in pyridine liquid and the mixture solution was sonicated and heated at 60 C° for 2-3 hours to get clear solution. Normally one hour is enough to get clear solution. Waiting for longer time is to ensure complete ligand exchange. Finally, ethanol was added into this solution and the mixture solution was centrifugalized to get the final product.

3.2.2 Device Fabrications

Different TiO_2 nanoparticles and P3HT were mixed in toluene (2mg/mL). OTFTs were fabricated by drop-casting method. Highly doped n-type silicon wafer with

500nm thermal oxide on the top was chosen as the substrate. SiO_2 surface was modified with hexamethyldisilazane (HMDS) monolayer. Then polymer films were coated on the SiO_2/n-type Si substrates, dried for more than one hour in a covered petri dish followed by a thermal annealing process at 120 ℃ in a glove box filled with high purity nitrogen. Gold source and drain electrodes were deposited on top of the polymer films through a shadow mask by thermal evaporation. All of the devices have the channel width and length of 2mm and 100μm, respectively.

Transmission Electron Microscopy (TEM): TEM (JEOL JEM 2010) was used to character the hybrid films and the TEM images are shown in Figure 3.2. The nanorods show regular shape and good crystallinity.

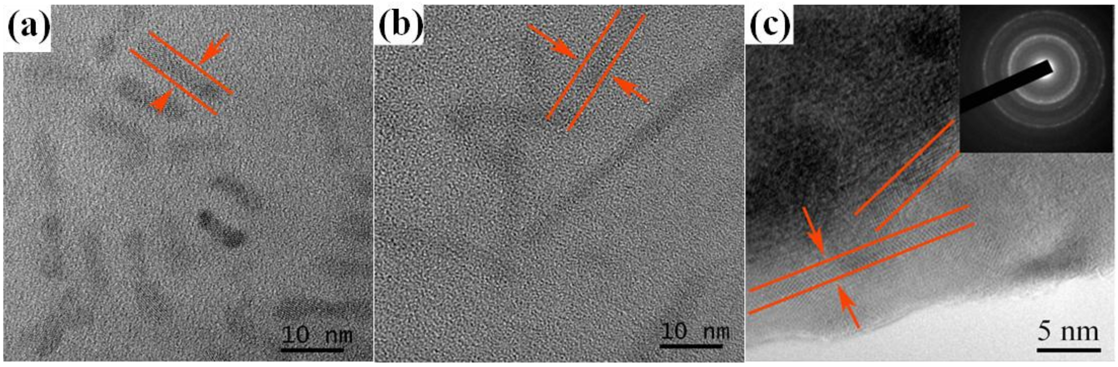

Figure 3.2 (a) TEM image of pyridine modified 3×10nm^2 TiO_2 nanorods (without P3HT); (b) TEM image of pyridine modified 3×20 nm^2 TiO_2 nanorods (without P3HT); (c) TEM images of pyridine modified 3×20 nm^2 TiO_2 nanorods mixed with P3HT film. Inset: selected area electron diffraction pattern of the composite film.

3.2.3 Measurement of Devices

The OTFTs were measured in a glove box with a Semiconductor Parameter Analyzer (Agilent 4156 C). For transfer characteristics, the channel current I_{DS} between source and drain was measured as a function of gate voltage V_G under a constant drain voltage. V_{DS}= -10 V for characterizing linear mobility μ_{lin} and V_{DS}= -100 V for saturation mobility μ_{sat}. For output characteristics, the channel current I_{DS} was measured as a function of drain voltage V_{DS} under a constant gate voltage V_G and different V_G (-100, -75, -50, -25 and 0V) resulted in different curves of I_{DS} versus V_{DS}. The photo response of the OTFT to UV light was characterized under a UV LED with a wavelength of 370nm. The LED intensity was controlled by different DC bias voltages [48].

Absorption spectrum: UV-Vis absorption spectra of composite films drop-cast on transparent silica substrates modified with HMDS were characterized by using a Shimadzu UV-2550 UV-vis spectrophotometer.

Space charge limited current: TiO_2 nanoparticles and P3HT composites or pure P3HT were dissolved in toluene (2mg/mL) and coated on PEDOT:PSS/ITO glass substrates by drop casting followed by a thermal annealing process at 120 ℃ in the glove box filled with high purity nitrogen. To get thick films, the solution were dropped on the substrate for many times. Then Au electrodes were deposited through a shadow mask by thermal evaporation. The *J-V* characteristics of the Au/P3HT-composite/ PEDOT:PSS/ITO sandwiched devices were characterized by semiconductor parameter analyzer (Agilent 4156C) in the glovebox. Positive voltage was applied on Au electrode to induce hole injection in P3HT layer.

X-Ray diffraction spectrum (XRD): Polymer films were characterized with Philips X'Pert X-ray Diffractometer with Cu Ka radiation.

3.3 Performance of Devices

First, TiO_2 nanorods (3×10 nm^2) modified with oleic acid and pyridine are mixed with P3HT (regioregularity: 90~93%; Molecular weight: 50,000) in toluene at a weight ratio of 0.75 and coated on n^+Si/SiO_2 substrate to fabricate OTFTs.

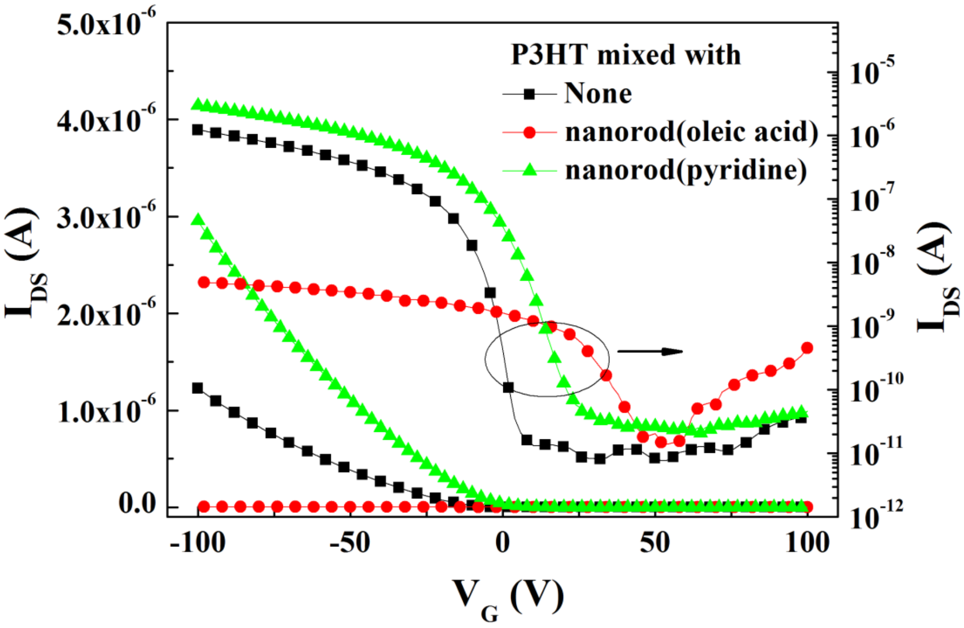

Figure 3.3 Transfer characteristics (I_{DS} ~ V_G) of OTFTs based on P3HT or TiO_2-nanorod / P3HT composite films, V_{DS} = -10V.

Figure 3.3 shows the transfer characteristics (I_{DS} vs. V_G, V_{DS} = -10V) of the OTFTs based on the P3HT/TiO_2 composites or pristine P3HT film. The composite film with TiO_2 nanorods modified with pyridine shows much higher channel current than that of the pristine P3HT film.

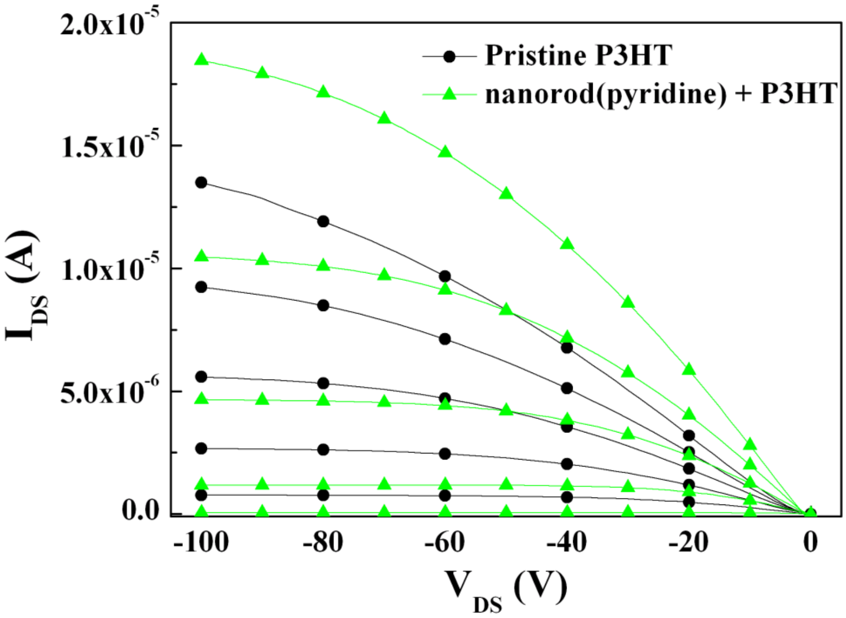

Figure 3.4 Output characteristics (I_{DS} ~ V_{DS}) of OTFTs based on P3HT or TiO_2-nanorod / P3HT composite films. For curves of each sample, from top to bottom, V_G is -100V, -75V, -50V, -25V and 0 V, respectively; Regioregularity of P3HT is 90~93%

Figure 3.4 shows the output characteristics (I_{DS} vs. V_{DS} at different V_G) of the OTFTs. Similar effect of the TiO_2 nanorods on the channel current can be observed in the output curves. The hole mobilities in the different films can be calculated from the transfer curves [197]. It is interesting to find that the device with pyridine-modified TiO_2 nanorods shows much higher field effect mobility than the pristine P3HT device while the oleic acid-modified TiO_2 nanorods decrease the hole mobility in P3HT matrix by two orders of magnitude. To clarify this phenomenon, control devices with same fabrication procedure are fabricated and measured. These control devices make use of P3HT solution with pyridine added to deposit the active layer of transistors. Their mobilities are shown in Figure 3.5.

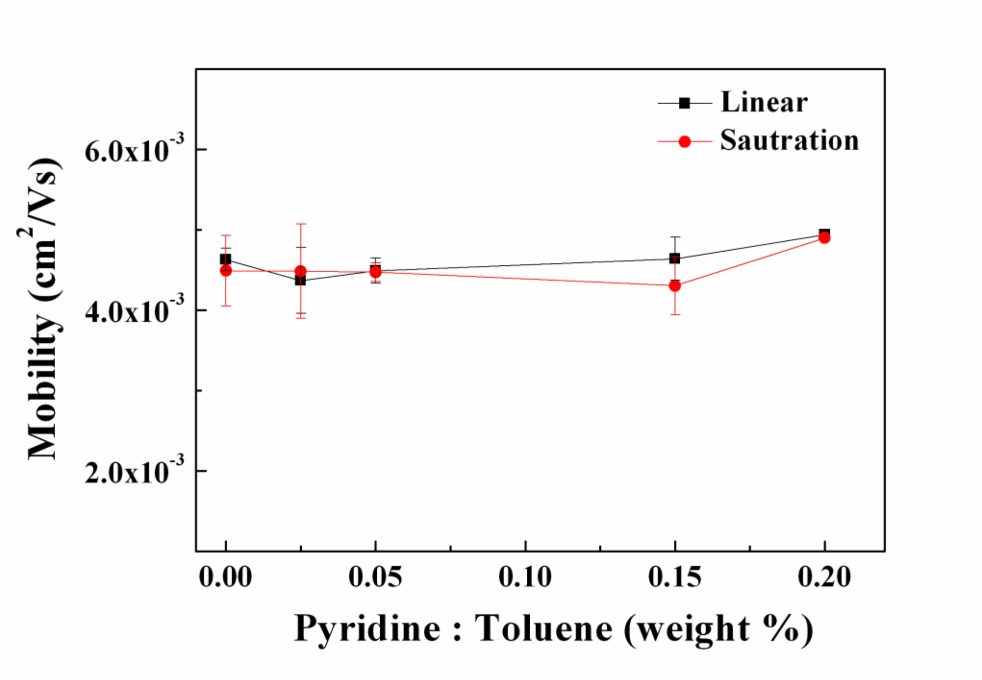

Figure 3.5 The average hole mobilities of P3HT (regioregularity: 90~93%) in OTFTs (12 samples for each condition) prepared with mixed solvents of pyrindine/toluene by drop casting. All of the samples were prepared in the same batch with the same processing conditions. The maximum amount of pyridine added in toluene is 0.2%, which is equal to the weight percentage of P3HT to toluene. Therefore, the amount of pyridine similar to that attached to TiO_2 nanorods (less than 0.2 %) will play little effect on carrier mobility of P3HT when it was added in the solvent (toluene) separately.

We find that the enhancement of carrier mobility in the former case is not due to the effect of adding small amount of pyridine in the solvent. These results indicate that the surface modification on the nanorods is critical to the device performance. It is not strange to find oleic acid modified on the surface being unfavorable for charge transport in P3HT. For example, Y. Y. Lin et al reported that organic solar cells based on P3HT and oleic acid-modified TiO_2 nanorods showed much lower power conversion efficiency (PCE) than the devices with pyridine-modified TiO_2 nanorods [208]. Although the big difference in PCE was attributed to the different conductivity of the surface modifier in that paper, the different hole mobility in P3HT can be another possible reason that was not addressed.

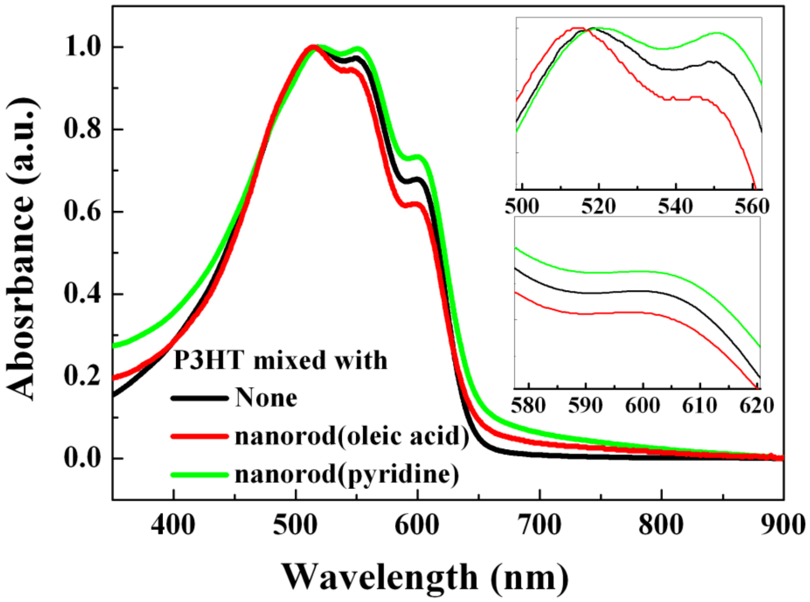

Figure 3.6 UV-visible absorption spectra of P3HT or TiO_2-nanorod / P3HT composite films. Insets: enlarged absorption peaks. For each composite film, the size of TiO_2-nanorod is: 3×10nm^2. Weight ratio of TiO_2 to P3HT is 0.75. Regioregularity of P3HT is 90~93%.

To better understand the effect of the TiO_2 nanorods on the device performance, UV-visible absorbance spectra of the P3HT/TiO_2 composite and pristine P3HT films fabricated at the same condition were characterized and shown in Figure 3.6. There are three absorption peaks at about 520nm, 550nm and 600nm for each sample. It is widely accepted that the first two peaks correspond to the intrachain π-π* transition, and the 600nm one is related to the interchain π-π* transition [209, 210]. We can find that the composite film with pyridine-modified TiO_2 nanorods shows a red shift of the peak at ~520nm as well as a higher peak at ~600nm compared with pristine P3HT film, indicating the longer conjugation length and better π-π stacking of the P3HT chains in the composite film, respectively. Therefore both peaks show the better crystallinity of the P3HT in the composite film with pyridine-modified TiO_2 nanorods than in the pristine film. On the contrary, the composite film with oleic acid-modified TiO_2 nanorods shows a blue shift of the absorption peak at ~520nm and lower peak at ~600nm compared with pristine P3HT film, which means the crystallinity of the P3HT matrix is deteriorated by the nanorods. Therefore the big difference in carrier mobility in the three OTFTs may be due to the different crystallinity of P3HT in the devices.

Unfortunately, the coupling between nanorods and polymer chains in the composite films can not be directly observed under TEM or AFM since the films are randomly oriented and have no long range ordering. D. H. Kim et al. reported that the interaction between surface modifier and alkyl chain/thienyl backbone of P3HT plays an important role on the orientation of P3HT relative to the substrate [200]. Therefore it is expected that the interaction between the surface modifier and P3HT influences the self-assembly process during the film solidification, especially the coupling between the nanorods and the polymer chains, which may enhance or deteriorate the crystallization of P3HT.

To study the influence of surface modifier on the crystallinity of P3HT layer separately, TiO_2 thin films were prepared by spin coating on glass substrates and modified with pyridine or oleic acid followed by coating a layer of P3HT thin film [192]. As shown in Figure 3.7, the sample with oleic acid modified on the surface of TiO_2 shows an obvious blue shift of the absorption peak at ~550nm and a lower peak at ~600nm compared with the sample modified with pyridine, indicating that the crystallinity of P3HT is lower in the former, which is consistent with our results for the composite films. The absorption spectra for the samples modified with pyridine or without any modification on TiO_2 films can hardly show any difference, which means the crystallinity of the P3HT layer on top of the two surfaces are very similar.

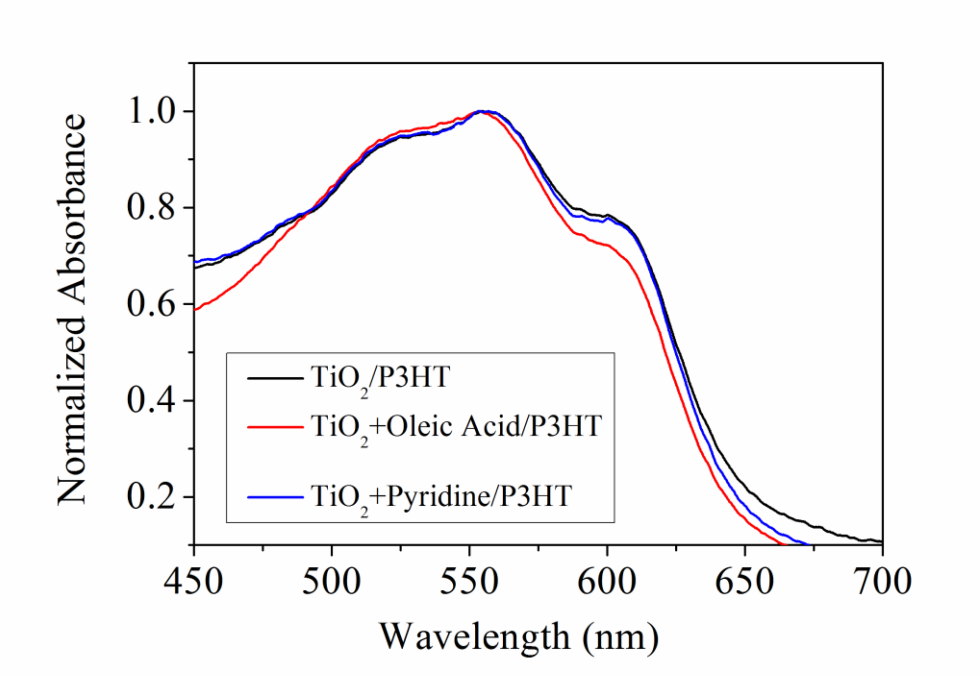

Figure 3.7 UV-visible absorption spectra (normalized to the peak at ~550nm) of P3HT films coated on top of a TiO_2 film and TiO_2 films modified with oleic acid or pyridine.

Next, we studied the effect of TiO_2 nanoparticles with different shapes on the performance of P3HT/TiO_2 hybrid OTFTs. Here, all of the nanoparticles are modified with pyridine.

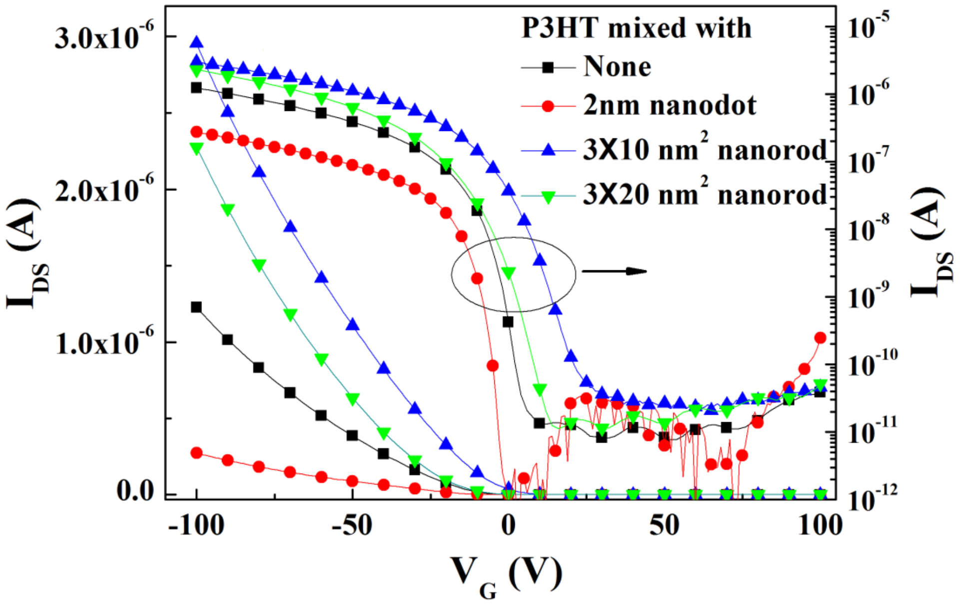

Figure 3.8 Transfer characteristics ($I_{DS} \sim V_G$) of OTFTs based on P3HT or TiO_2 / P3HT composite films, V_{DS} = -10V, Regioregularity of P3HT is 90~93%.

Figure 3.8 shows the transfer characteristics of the devices based on TiO_2 nanorods (length: 10 nm or 20 nm) or nanodots (diameter: 2 nm). The hole mobilities in different samples can be calculated from the transfer curves. It is interesting to find that only the TiO_2 nanorods can increase the hole mobility of P3HT while the nanodots decrease the mobility dramatically. Figure 3.9 shows the absorption spectra of the P3HT/TiO_2 composites with different nanoparticles. The crystallinity of P3HT matrix is enhanced by TiO_2 nanorods (10 nm and 20 nm) while degraded by nanodots. The 20 nm TiO_2 nanorods induce even higher crystallinity of P3HT than the 10 nm nanorods do, while the carrier mobilities in the two devices are very similar.

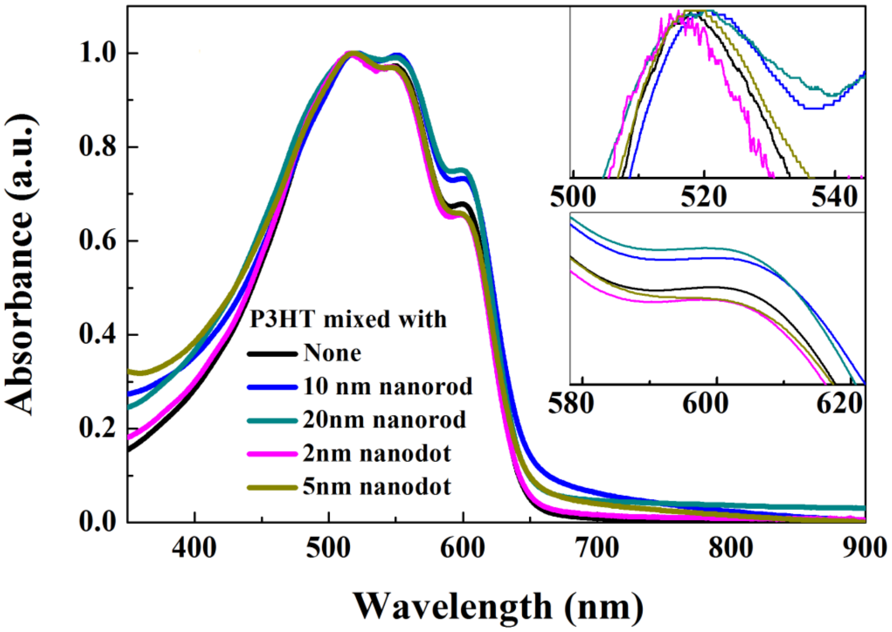

Figure 3.9 UV-visible absorption spectra of P3HT or TiO_2/P3HT composite films. Insets: enlarged absorption peaks; Regioregularity of P3HT is 90~93%.

The enhancement of the crystallinity of P3HT matrix induced by TiO_2 nanorods also can be observed in AFM images of the composite films, as shown in Figure 3.10. The AFM image of composite film shows a relatively bigger grain size than pristine P3HT film. Obviously the bigger grain size benefits carrier transport in the composite film [204].

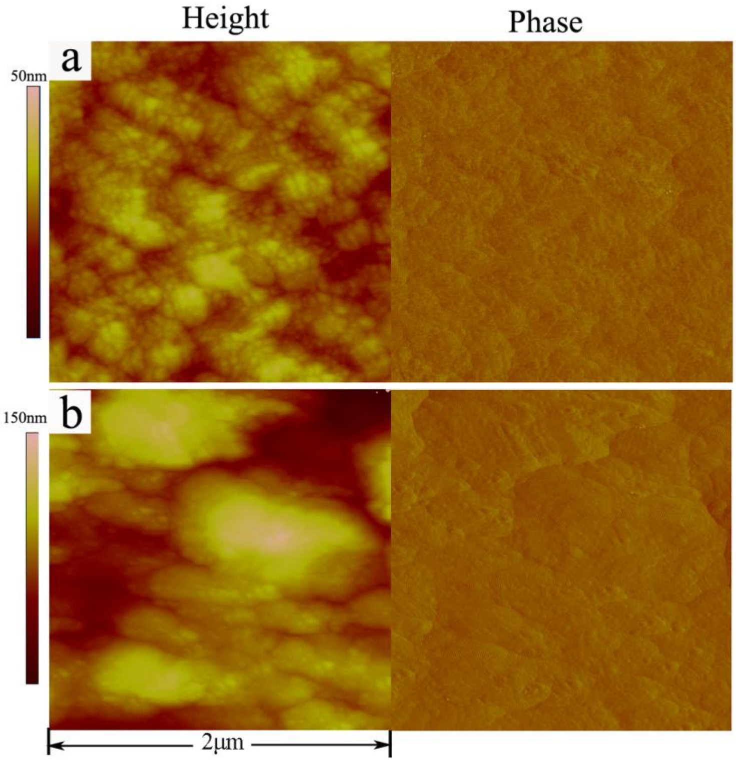

Figure 3.10 AFM images of (a) P3HT film and (b) TiO_2/P3HT composite films with TiO_2 nanorods (3×20 nm^2) modified with pyridine.

Figure 3.11 shows the X-Ray diffraction (XRD) spectra of a pure P3HT film and three different P3HT/TiO_2 composite films. The (010) peak can be observed in the pure P3HT film and the P3HT/TiO_2-nanodots composite film. The peak height of the latter one is even higher than that of the former one indicating that there are more plane-on P3HT domains when it is mixed with TiO_2 nanodots [197]. However, the (010) peak cannot be observed in the composites with TiO_2 nanorods and thus edge-on P3HT domains dominate in the composite films, which are favourable for carrier transfer in P3HT films [197]. Therefore the orientation of P3HT chain is influenced by the nanoparticles, which can be regarded as another reason why the TiO_2 nanorods and nanodots show different effects on the hole mobilities in P3HT films. But the cause of the orientational change is not fully understood.

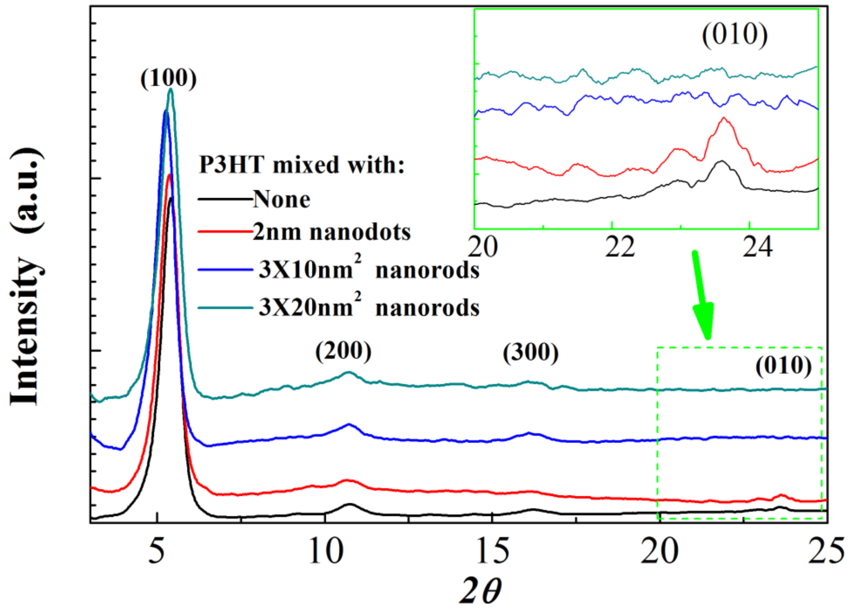

Figure 3.11 XRD spectra of a P3HT film and P3HT / TiO_2 composite films. Regioregularity of P3HT is 90~93%

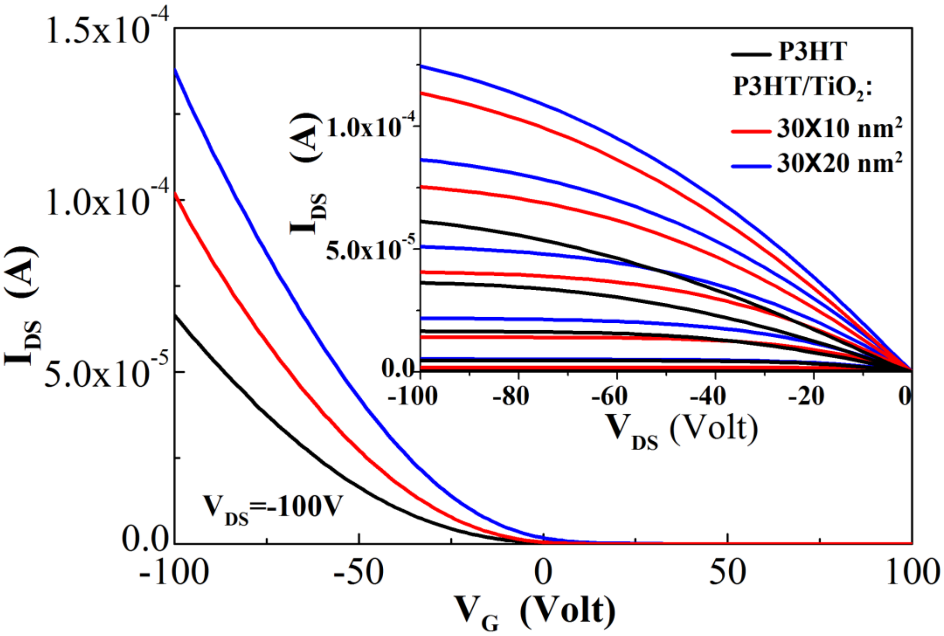

Figure 3.12 Transfer characteristics (I_{DS} ~ V_G) of OTFTs based on P3HT with or without TiO_2 nanorods modified with pyridine. V_{DS}=-100V. Regioregularity of P3HT is 98%. Inset: output characteristics (I_{DS} ~ V_{DS}) of the three devices. For curves of each device, from top to bottom, V_G are -100V, -75V, -50V, -25V and 0 V, respectively.

P3HT with higher regioregularity (98%, Molecular weight: 25,000, Sepioilid^{TM}, P200) has been used in the experiments. Figure 3.12 shows the transfer and output characteristics of the devices with or without TiO_2 nanorods. It is interesting to find that similar effect can be observed in these samples and the hole mobility can reach as high as 0.23 cm^2/Vs when P3HT is mixed with $3\times20nm^2$ TiO_2 nanorods modified with pyridine.

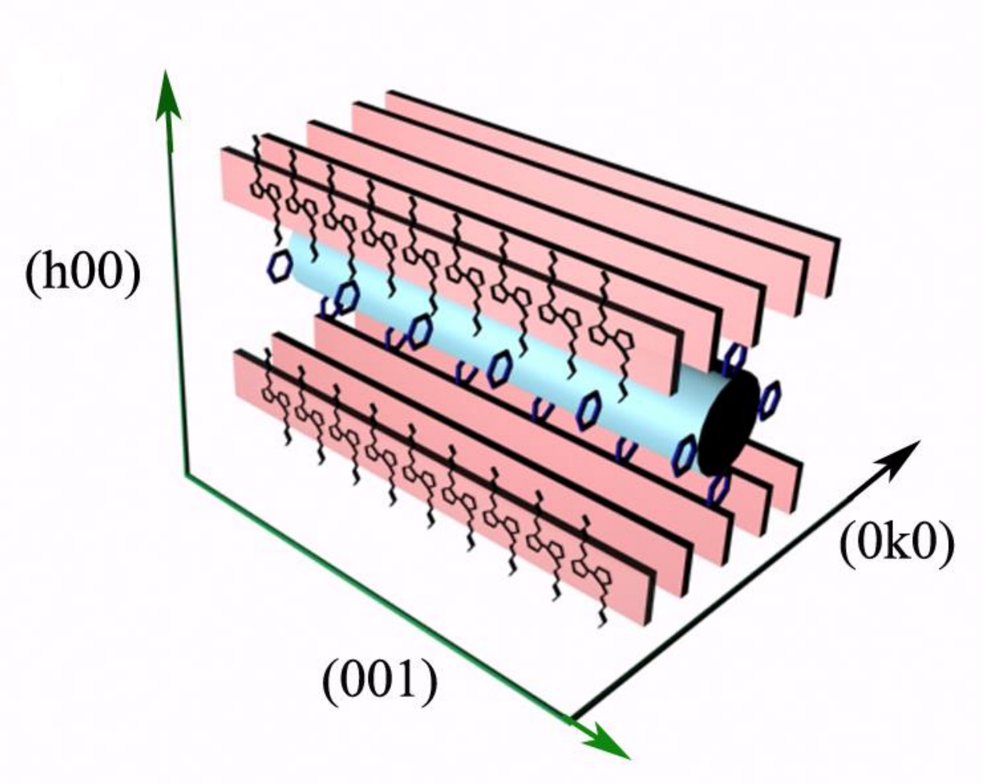

Figure 3.13 Illustration of the possible alignment of P3HT chains together with a TiO_2 nanorod modified with pyridine.

Actually the coupling between nanorods and P3HT chains was reported by M. Brinkmann et al., who have studied the self-assembly process in CdSe/P3HT composite films [211]. They found that CdSe nanorods exhibited raft-like aggregation in the ordered region of P3HT and preferentially oriented with their long axis parallel to the P3HT chain direction while CdSe nanodots distributed only in amorphous region of semi-crystalline P3HT films. But the influence of the CdSe nanoparticles on carrier mobility in the composite films is unclear. Obviously, interdigitation between CdSe nanorods and P3HT chains indicates a strong coupling between them in the self-assembly process when the film was coated. Spherical CdSe nanodots can not form an ordered distribution in the amorphous region of P3HT and thus it can not enhance the crystallization of the polymer film. Similarly, the coupling between TiO_2 nanorods and polymer chains in the TiO_2/P3HT composite films is expected in our experiments, which is regarded as the main reason for the enhanced crystallinity, optimized polymer orientation and higher carrier mobility of P3HT matrix in the composite films as addressed above. A possible alignment of P3HT chains together with a TiO_2 nanorod is illustrated in Figure 3.13.

Then OTFTs with different weight ratio of pyridine-modified TiO_2 nanorods to P3HT are fabricated and characterized. Figure 3.14a and b show the relationships between hole mobility and the weight ratio for 10 nm and 20 nm nanorods, respectively. The optimum mass ratio of TiO_2 to P3HT is about 0.5 ~0.75 for both nanorods.

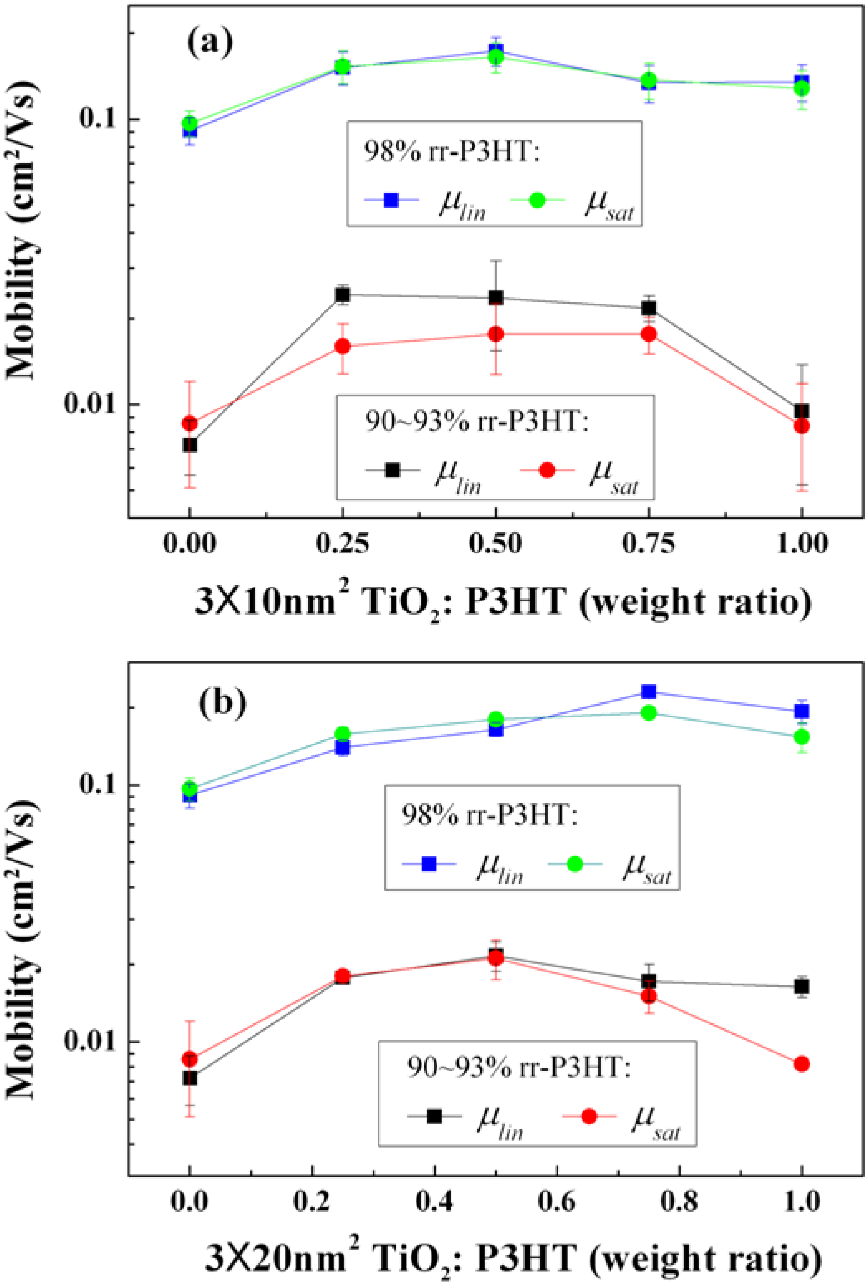

Figure 3.14 Field effect mobility of TiO_2-nanorod/P3HT composite film versus weight ratio of TiO_2-nanorod to P3HT. The nanorods are all modified with pyridine on the surface and have sizes of 3×10 nm^2 and 3×20 nm^2 for (a) and (b), respectively

Figure 3.15 shows the UV-visable absorbance spectra of the composite films with different weight ratio of TiO_2 nanorods ($3\times20nm^2$) to P3HT (regioregularity: 90~93%). We find that the absorption peaks at ~600nm for all composite films are higher than that of pristine P3HT film, indicating that the crystallinity of P3HT matrix are improved due to the presence of TiO_2 nanorods. The film with a weight ratio of 0.5 shows the highest peak and thus the best crystallinity of P3HT, which is consistent with the highest field effect mobility observed at this composition. If mass ratio is larger or less, the crystallinity of P3HT as well as the carrier mobility will decrease. Similar results were found in composite films with 3×10 nm^2 TiO_2 nanorods. So the self-assembly process in the composite film is influenced by the weight ratio of the nanorods to P3HT, which has also been observed in CdSe nanorods/P3HT composite films before [211].

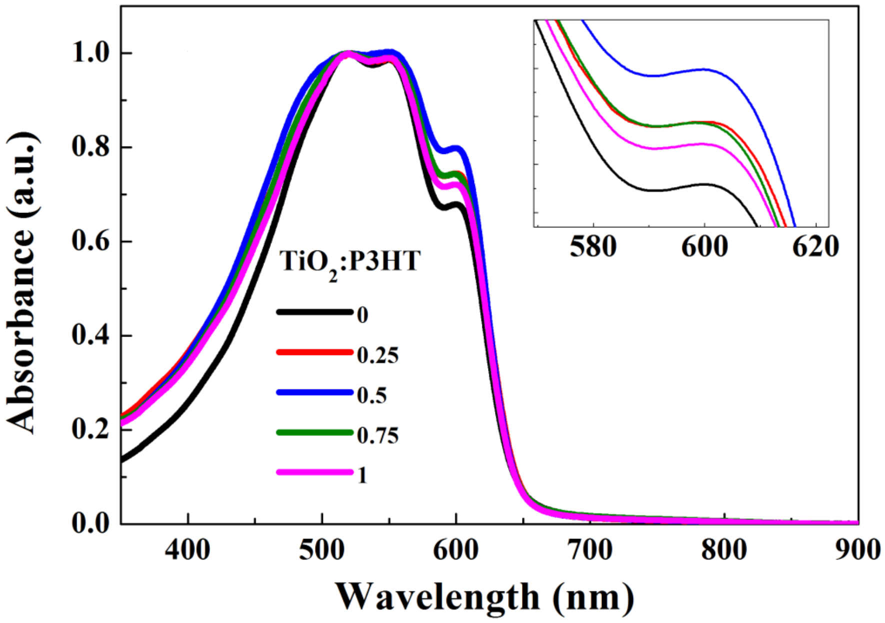

Figure 3.15 Absorption spectra of TiO_2-nanorod/P3HT composite film with different weight ratio of TiO_2-nanorod to P3HT. Inset: enlarged absorption peaks. The size of nanorods is 3×20 nm^2. Regioregularity of P3HT is 90~93%.

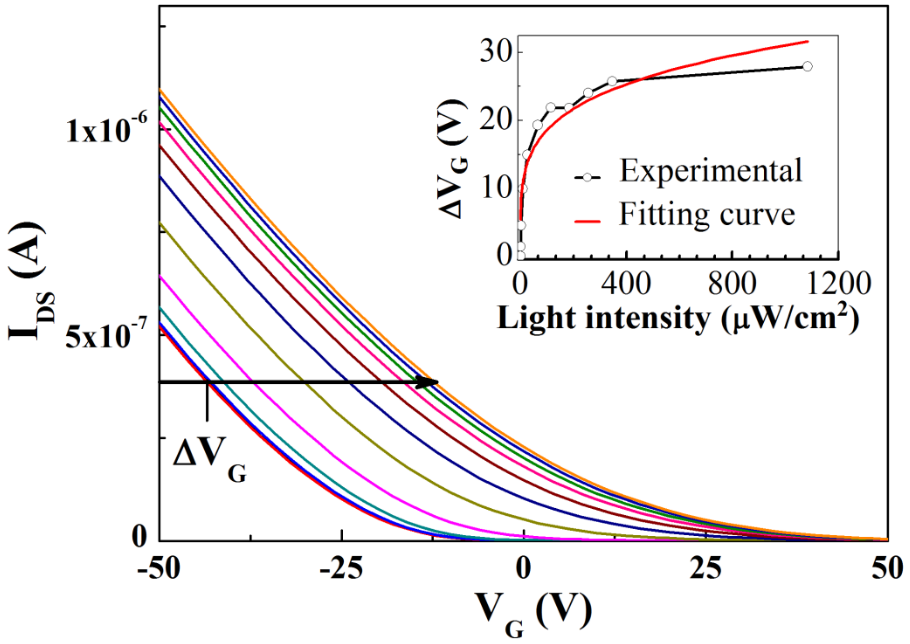

Figure 3.16 Transfer characteristics of an OTFT based on 3×10 nm2 TiO2-nanorod/P3HT composite film under 370nm UV illumination with different intensity. V_{DS} =-10V. The arrow indicates the shift direction of the transfer curve of the device illuminated with increased light intensity. Inset: Shift of gate voltage vs. light intensity I. The relationship can be fitted with: $\Delta V_G = \alpha E_e^{\beta}$, α is a constant and β = 0.22. The fitting curve is shown in red.

Transistors based on the TiO_2/P3HT composite films are one type of phototransistors as reported in our previous papers [47, 48]. A device with TiO_2 nanorods have been characterized under 370nm UV light with different light intensities, as shown in Figure 3.16. It is worth noting that the current response of the device to light illumination is ~10 times higher than that of the OTFT based on P3HT and TiO_2 nanoparticles reported in our previous paper. The transfer curve shifts to higher gate voltage horizontally with the increase of light intensity (E_e) and the gate voltage change (ΔV_G) can be fitted with the analytical model [47]:

$$\Delta V_G = \alpha E_e{}^{\beta} \qquad 3\text{-}1$$

where α is a constant and $\beta = 0.22$. It is worthy of note that similar phototransistors based on organic/inorganic composites have been investigated by our group before [47, 48] and equation 3-1 was also successfully used in those visible and ultraviolet phototransistors. The shift of the transfer curve can be attributed to the accumulation of electrons in the embedded TiO_2 nanorods [47]. Under UV light illumination, excitons will be generated in the TiO_2 nanorods and dissociate at the TiO_2/P3HT interface. Electrons will be trapped in the TiO_2 nanorods while holes will diffuse into P3HT matrix. Therefore the trapped electrons in the TiO_2 nanorods will decrease the electrostatic potential of the active layer and induce a shift of the threshold voltage of the device to a more positive value [47].

We find that the nanoparticles will not only influence the field effect mobility of P3HT in transistors but also the bulk hole mobility characterized by measuring space charge limited current (SCLC) of the composite films. The *J-V* curves for the devices with the sandwich structure of Au/polymer composite/ PEDOT:PSS/ITO glass have been measured and shown in Figure 3.17. The SCLC is given by $J = \frac{9}{8}\varepsilon_0\varepsilon_r\mu\frac{V^2}{d^3}$, where V is the applied bias voltage, d is the thickness of the composite film, ε_0 is the dielectric constant of vacuum and $\varepsilon_r \approx 3$ is the relative dielectric constant of P3HT film [212]. Therefore, $\sqrt{J}$ is proportional to bias voltage V and the slope will give the hole mobility. The composite film with pyridine-modified TiO_2 nanorods shows much higher hole mobility (3.36×10^{-4} cm^2/Vs) than that of the pristine P3HT film (6.58×10^{-5} cm^2/Vs) while the one with the oleic acid-modified TiO_2 nanorods shows much lower value (2.05×10^{-6} cm^2/Vs).

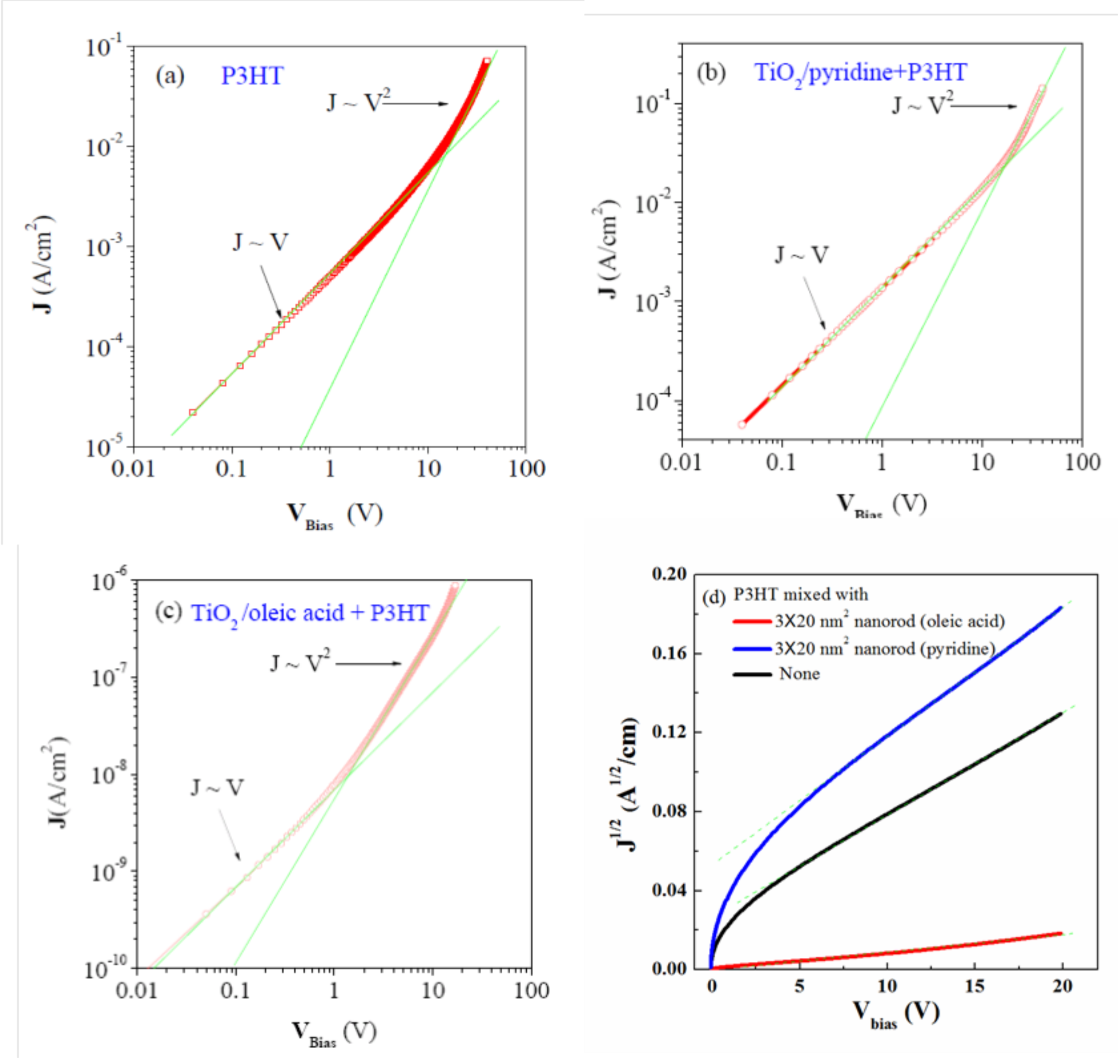

Figure 3.17 *J*–*V* characteristics of reverse biased (a) Au/P3HT/PEDOT:PSS (b) Au/P3HT+TiO_2(pyridine)/PEDOT:PSS and (c) Au/P3HT+TiO_2 (Oleic acid)/ PEDOT:PSS sandwiched devices. (d) $J^{1/2}$ –*V* characteristics of the three different devices, which show SCLC behavior. The film thicknesses for (i) pristine P3HT, (ii) composites of P3HT and oleic acid-modified nanorods and (iii) composites of P3HT and pyridine-modified nanorods are 868 nm, 1042 nm and 1302 nm, respectively.

Figure 3.18 shows the linear and saturation carrier mobility of some representative

OTFTs. We find that all of the devices with TiO_2 nanorods or nanodots without surface modification show much lower hole mobility than that of pristine P3HT, as shown in Table 3.1. Since the TiO_2 nanoparticles without any surface modification cannot be uniformly dispersed in the solvent, the poor performance of the devices can be attributed to the aggregation of nanoparticles in the composite films. Therefore, both the surface modifier and the shape of the nanoparticles are critical issues for obtaining the composite films with high carrier mobility.

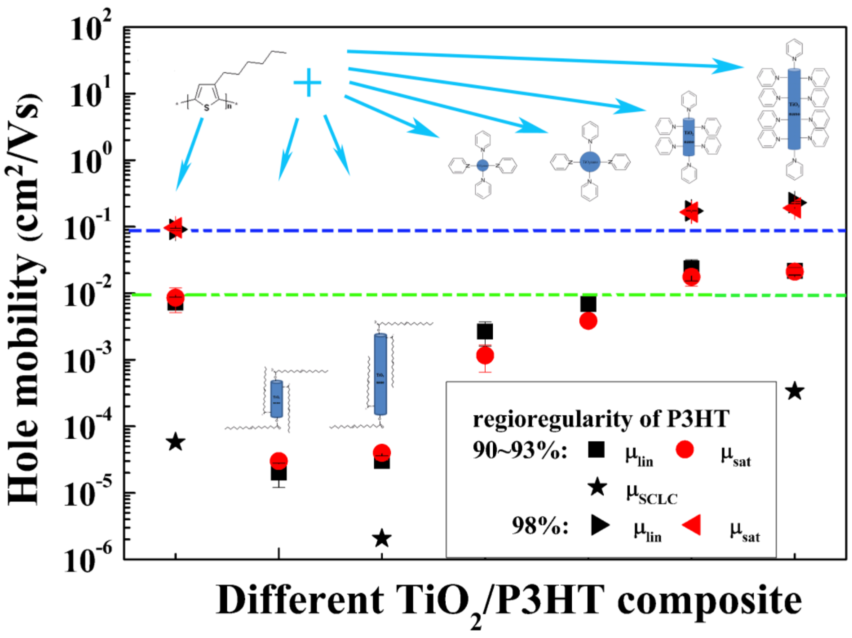

Figure 3.18 Linear (μ_{lin}) and saturation (μ_{sat}) field effect mobilities and bulk mobilities (μ_{SCLC}) of composite films with different TiO_2 nanoparticles. Weight ratio of TiO_2 to P3HT is 0.75 for all samples. Four types of TiO_2 nanoparticles are modified with pyridine: nanorods (3×10 nm^2 or 3×20 nm^2); nanodots (2nm or 5nm). Two types of TiO_2 nanorods are modified with oleic acid.

Table 3.1 Hole mobilities in a P3HT film or TiO_2 /P3HT composite films with different TiO_2 nanoparticles.

TiO_2 nano-material/P3HT	**Regioregularity of P3HT**	**Linear mobility μ_{lin} $(cm^2V^{-1}s^{-1})$**	**Saturation mobility, μ_{sat} $(cm^2V^{-1}s^{-1})$**	**SCLC Mobility μ_{SCLC} $(cm^2V^{-1}s^{-1})$**
Pristine P3HT	90~93%	$(7.2\pm1.6)\times10^{-3}$	$(8.6\pm3.5)\times10^{-3}$	$(6.58\pm0.66)\times10^{-5}$
5×20nm² nanorod☆	90~93%	$(4.6\pm1.0)\times10^{-4}$	$(3.5\pm1.0)\times10^{-4}$	
10nm nanodot☆	90~93%	$\sim2\times10^{-5}$	$\sim5\times10^{-5}$	
10-100nm nanoparticle☆	90~93%	$(8.3\pm1.0)\times10^{-4}$	$(5.4\pm1.0)\times10^{-4}$	
2nm nanodot+pyridine	90~93%	$(2.7\pm1.1)\times10^{-3}$	$(1.2\pm0.5)\times10^{-3}$	
5nm nanodot+pyridine	90~93%	$(5.9\pm0.8)\times10^{-3}$	$(3.9\pm0.5)\times10^{-3}$	
3×10nm² nanorod+pyridine	90~93%	$(2.2\pm0.8)\times10^{-2}$	$(1.8\pm0.5)\times10^{-2}$	
3×20nm² nanorod+pyridine	90~93%	$(2.0\pm0.3)\times10^{-2}$	$(1.6\pm0.4)\times10^{-2}$	$(3.36\pm0.10)\times10^{-4}$
3×10nm² nanorod+oleic acid	90~93%	$(2.0\pm0.8)\times10^{-5}$	$(3.0\pm0.3)\times10^{-5}$	
3×20nm² nanorod+oleic acid	90~93%	$(3.0\pm0.6)\times10^{-5}$	$(4.0\pm0.9)\times10^{-5}$	2.05×10^{-6}
Pristine P3HT	98%	0.091 ± 0.02	0.096 ± 0.06	
3×10nm² nanorod+pyridine	98%	0.17 ± 0.02	0.17 ± 0.02	
3×20nm² nanorod+pyridine	98%	0.23 ± 0.01	0.19 ± 0.01	

3.4 Summary

In summary, field effect mobility in TiO_2/P3HT composite film is strongly related to the shape and surface modifier of the TiO_2 nanoparticles. It is reasonable to expect that other inorganic nanorods with the same shape and surface modifier will show the similar effect. These results indicate that, besides the physical properties of the inorganic nanoparticles, the shape and surface modifier of them are both critical issues for organic-inorganic composite films, which are of general importance for their application in solar cells, transistors or other semiconductor devices.

Chapter 4 **Highly Sensitive Organic Near-infrared Phototransistors Based on Poly(3-hexylthiophene) and PbS Quantum Dots**

4.1 **Introduction**

Infrared (IR) photodetectors have attracted much interest because of their broad applications in society security, military, medical diagnosis and so on [10, 32]. Various functional materials including quantum dots (QDs) [10, 32, 52, 213], organic semiconductors [76, 214] and graphene[49, 51, 77, 215] have been investigated for their applications in high performance IR photodetectors. It is notable that sensors based on organic semiconductors have many advantages, including low cost, solution processability and flexibility [12]. With the fast development of organic electronics in the past decade, the carrier mobilities in some organic semiconductors are comparable to or even higher than that of amorphous silicon [216, 217], implying their broad potential applications in the future. Some narrow-bandgap organic semiconductors have been used in IR photodetectors [76, 214, 218, 219]. However, the responsivities of these devices are normally very low [214, 219].

Composite films of QDs and organic semiconductors have been used in IR sensors as well. Mcdonald et al. reported solution-processed lead sulfide (PbS) QDs and poly[2-methoxy-5-(2’-ethylhexyloxy-p-phenylenevinylene)] (MEH-PPV) composite films for IR photodetectors [213]. However, the quantum efficiency (~ 0.006%) and the responsivity of the device to IR light illumination are very low. Rauch et al reported infrared photodiodes with PbS QDs-sensitized P3HT/PCBM blends, which show quantum efficiencies up to 51% and the responsivity of ~ 0.5A/W [220]. It is notable that photodiodes normally have quantum efficiency/gain less than 1, therefore their responsivity is relatively low. Photoconductor is another type of photodetector, in which light-excited carriers can circulate in the channel for many times before the recombination with opposite charges. Therefore its gain is much higher than 1 and the responsivity may become very high [221]. For example, IR photoconductors based on Pb QDs show very high responsivities up to 2700A/W [52]. Since organic semiconductors show many advantages over inorganic QDs in terms of solution processability and carrier mobility [12, 216, 217], better performance is expected in the photoconductors based on inorgnaic QD and organic semiconductor hybrid films. In this chapter, near-infrared (NIR) hybrid phototransistors based on PbS QDs and Poly(3-hexylthiophene) (P3HT) films were prepared by solution process. P3HT is a typical high-mobility organic semiconductor popularly used in organic thin film transistors (OTFT) and organic solar cells [88, 132, 192]. It is notable that the phototransistor can be regarded as a type of photoconductor when the gate voltage is fixed. More importantly, the photo sensitive behavior can be modulated by the gate voltage. The PbS QDs/P3HT hybrid phototransistors show high responsivity up to 2×10^4 A/W under NIR illumination (wavelength: 895nm), which is one order of magnitude higher than the photoconductors of pure PbS QDs [52]. The transfer curves of the device shift to positive gate voltage horizontally under NIR illumination, indicating p-type doping effect in P3HT film due to the charges generated in PbS QDs [47, 48]. Therefore such hybrid phototransistors are promising in the applications of IR detectors.

4.2 Experimental

4.2.1 Materials

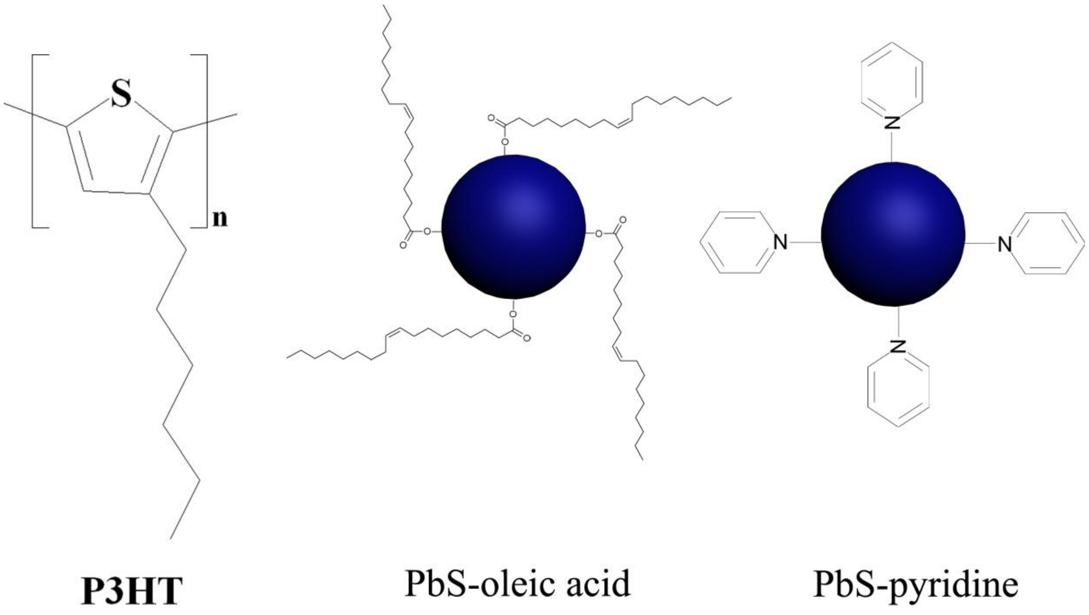

Figure 4.1 The molecular structure of P3HT and the schematics of oleic acid/-capped PbS QD and pyridine/-capped PbS QD.

Poly(3-hexylthiophene) (P3HT): The regioregular P3HT (Sepioilid^{TM} P200, regioregularity: ~98%, molecular weight: 25000) was purchased from Rieke Metals without further purification. The Lowest Unoccupied Molecular Orbital (LUMO) and highest occupied molecular orbital (HOMO) of P3HT are 3.2eV and 5.0eV respectively.

Lead Sulphide Quantum Dots (PbS QDs): oleic acid-capped PbS QDs were purchased from Evident Technologies Inc, USA.

Ligand exchange: Considering the long oleic acid ligand has been proven to be insulator and may inhibit the charge transfer between P3HT and PbS [222], ligand exchange of the oleic acid on PbS QDs to pyridine was carried out by the following procedure [88]. Firstly, the oleic acid-capped PbS colloidal toluene solution was mixed with ethanol with a volume ratio of 1:2. Then the solution was centrifugated and the supernatant liquor was removed. The black precipitate was re-dispersed in pyridine liquid and the mixture was sonicated and heated at 60 C° for about 1 hour to get clear solution. Then the colloidal solution was mixed with ethanol with volume ratio of 1:2, again. This mixture was centrifugated and the black precipitate was the pyridine-capped PbS QDs. Then the product was redispersed in toluene with certain concentration by sonication and long time stir at room temperature. The molecular structure of P3HT and the schematic of PbS QD capped with oleic acid or pyridine are shown in Figure 4.1.

Specific of PbS QDs: It was reported that PbS is a semiconductor with a bandgap of 0.41eV and an ionization potential of ~4.95 eV when it is a bulk material [213]. For PbS QDs, the ionization potential may be higher due to the effect of quantum confinement. For the PbS QDs, the bandgap is estimated to be about 1.2 eV since the absorption peak is at the wavelength of ~990nm (as shown in Figure 4.2). Because the holes and electrons in PbS have nearly equal effective masses [213], the conduction band and valence band levels of PbS QDs will move up and down from those of the PbS bulk by the same amount, respectively. Therefore, energy levels for the conduction (E_c) and valence (E_v) bands of PbS QDs are estimated to be 4.15 eV and 5.35 eV, respectively.

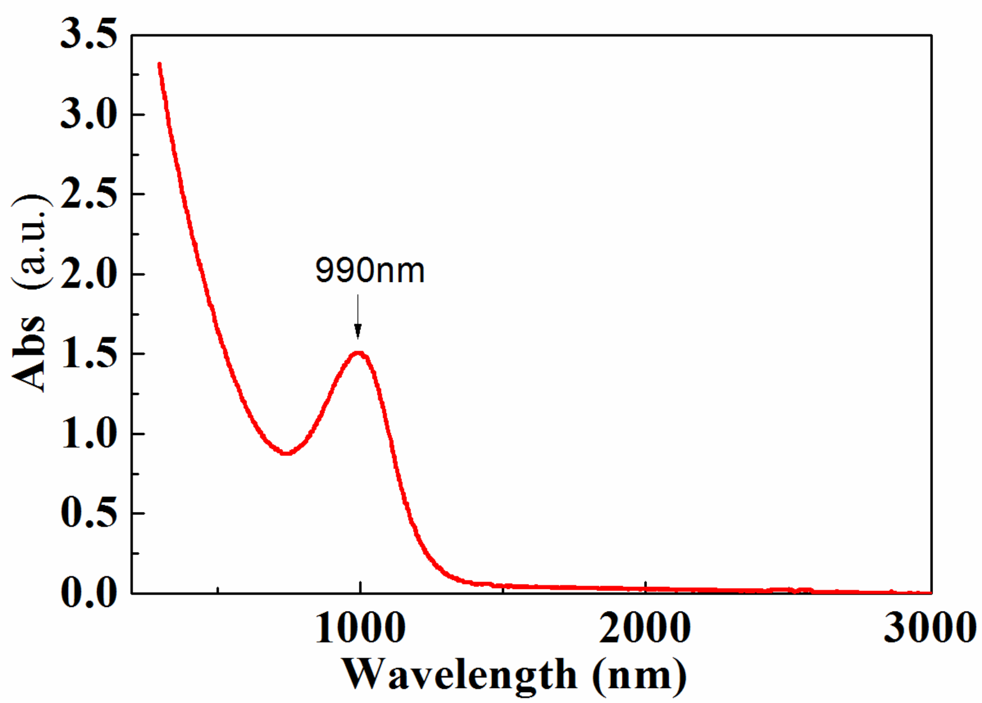

Figure 4.2 Light absorbance of PbS QDs

4.2.2 Device Fabrications

The pyridine-capped PbS QDs and P3HT were mixed in toluene with both 5mg/ml. Highly doped n-type Silicon wafers with 500nm silicon oxide layer on the top were chosen as the substrates. The surfaces of silicon oxide layer were modified with hexamethyldisilazane(HMDS) through immersing them in HMDS beyond 12 hours. The mixture solution was deposited on the top of substrate by spin coating method. A thermal annealing process at 130℃ was followed in the glove box filled with high purity nitrogen. Then gold source and drain electrode were deposited on the top of hybrid films through a shadow mask by thermal evaporation. The channel width and length are 2mm and 0.1mm, respectively. The schematic of the device structure and a photo of a real device are shown in Figure 4.3

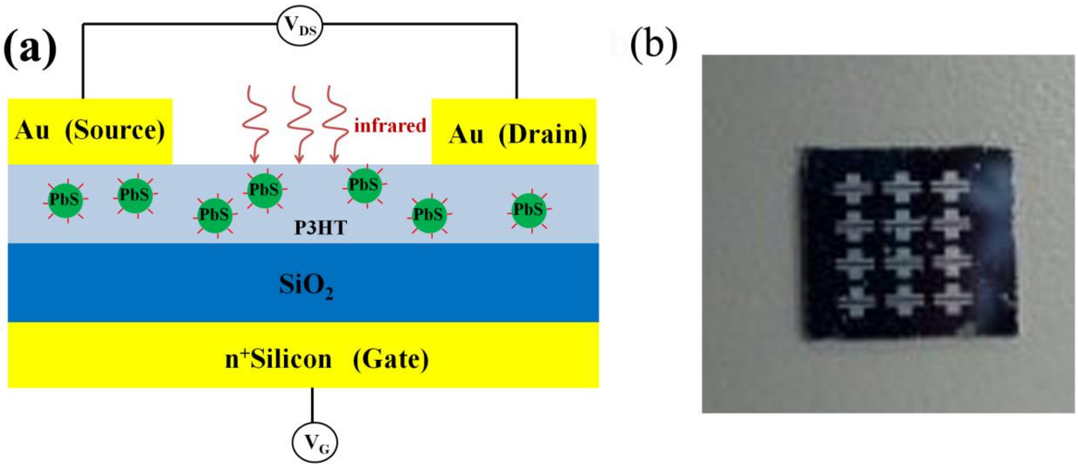

Figure 4.3 (a) Schematic of device structure and measure. (b) A photo of a real devices.

As comparison, Control samples of pure P3HT OTFTs were also fabricated at the same condition for comparison.

Photoluminescence spectrums (PL): Photoluminescence spectrums (EDINBURGH INSTRUMENTS Photoluminescence system with laser as an excitation source) of the pure P3HT, oleic acid-capped PbS QDs/P3HT and pyridine-capped PbS QDs/ P3HT films were measured and shown in Figure 4.4. It is notable that the PbS QDs have the emission peak at ~1100nm while the P3HT film does not show any peak in this wavelength region. The oleic acid-capped PbS QDs/P3HT hybrid film shows higher emission peak than the hybrid film of pyridine-capped PbS QDs/P3HT, indicating that more photo-induced carriers transfer to P3HT in the later one. Therefore charge transfer across pyridine is easier than that across oleic acid. So the ligand exchange of the PbS QDs from oleic acid to pyridine can improve the sensitivities of the hybrid phototransistors [223].

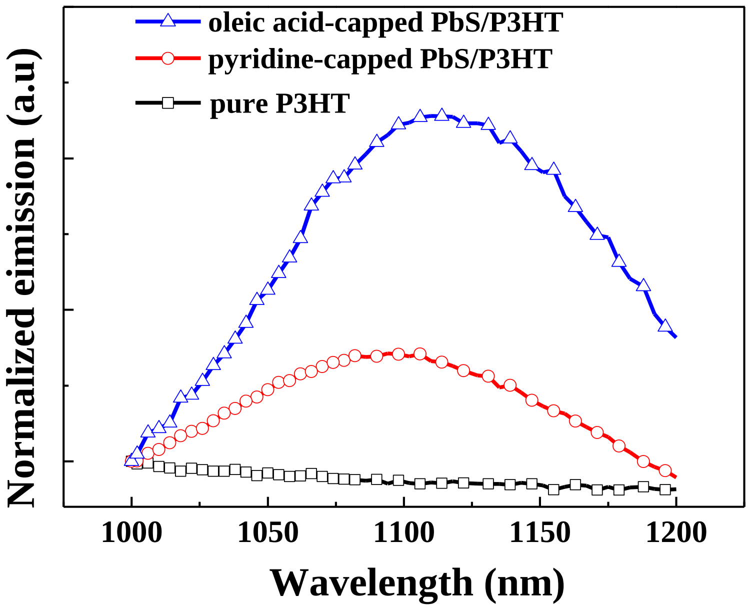

Figure 4.4 Photoluminescence (PL) spectra of pure P3HT film, oleic acid-capped PbS QDs/P3HT film and pyridine-capped PbS QDs/P3HT film.

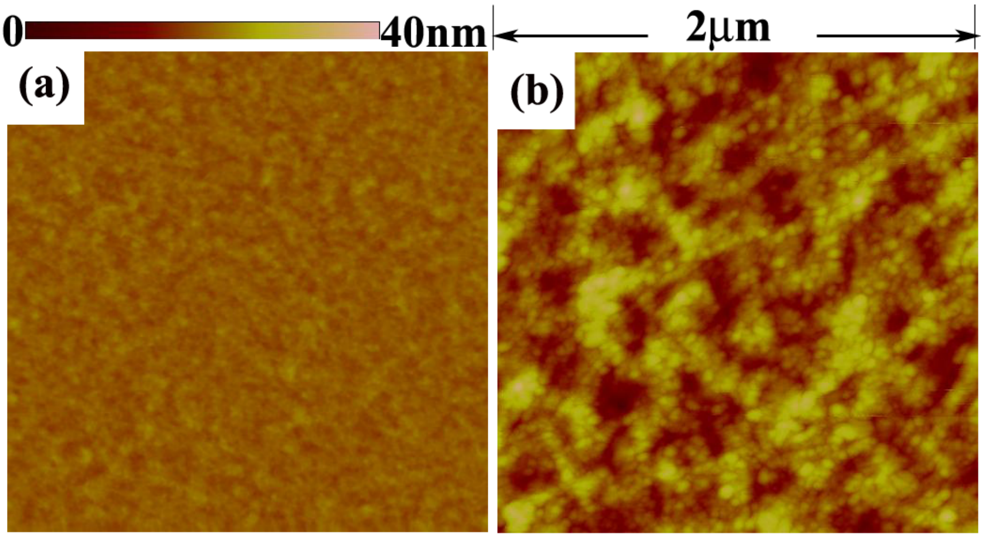

Figure 4.5 AFM images of (a) pure P3HT film. Roughness (r.m.s.):0.86nm, and (b) PbS QDs/P3HT film. Roughness(r.m.s.): 4.09nm.

Atomic Force Microscopy (AFM): The surface morphologies of the pure P3HT film and pyridine-capped PbS QDs/P3HT hybrids film were characterized by AFM (Vecco Metrology group NanoScope Ⅳ Scanning Probe Microscope) and shown in Figure 4.5. Their roughnesses are 0.86nm and 4.09nm, respectively. So the hybrid film has bigger roughness than the pure P3HT film.

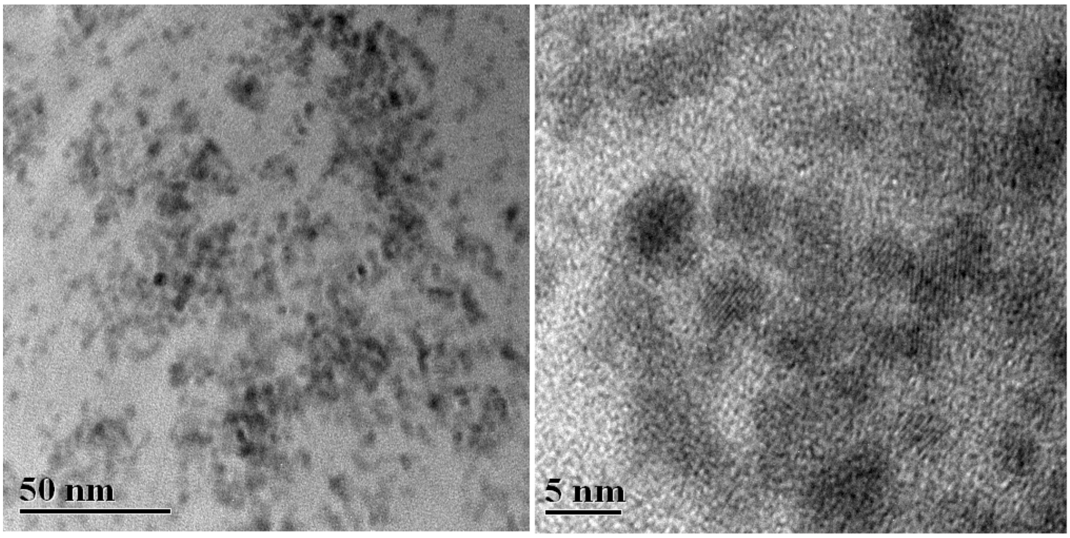

Figure 4.6 Transmission Electron Microscopy (TEM) images of films with PbS QDs dispersed in P3HT.

Transmission Electron Microscopy (TEM): Transmission Electron Microscopy (TEM, JEOL JEM 2010, Japan) was used to characterize the dispersion of PbS QDs in P3HT film. The TEM images with different scales are shown in Figure 4.6. The average size of the PbS QDs is about 4 nm.

4.2.3 Measurement of Devices

The infrared phototransistors were characterized by a semiconductor parameter analyzer (Agilent 4156C) under light illumination with different irradiance in the glovebox. The light sources were monochromatic LED with the wavelength of 895 nm with its light irradiance controlled by a DC power source. The glovebox is full of high purity N_2 and the voltages were applied on every electrode by a probes system. Photoresponse measurements were carried out with infrared from upside, as shown in Figure 4.3a. For the transfer and output characteristics, light illumination at different irradiance was kept for 2 minutes for balance before every measurement.

4.3 Performance of Devices

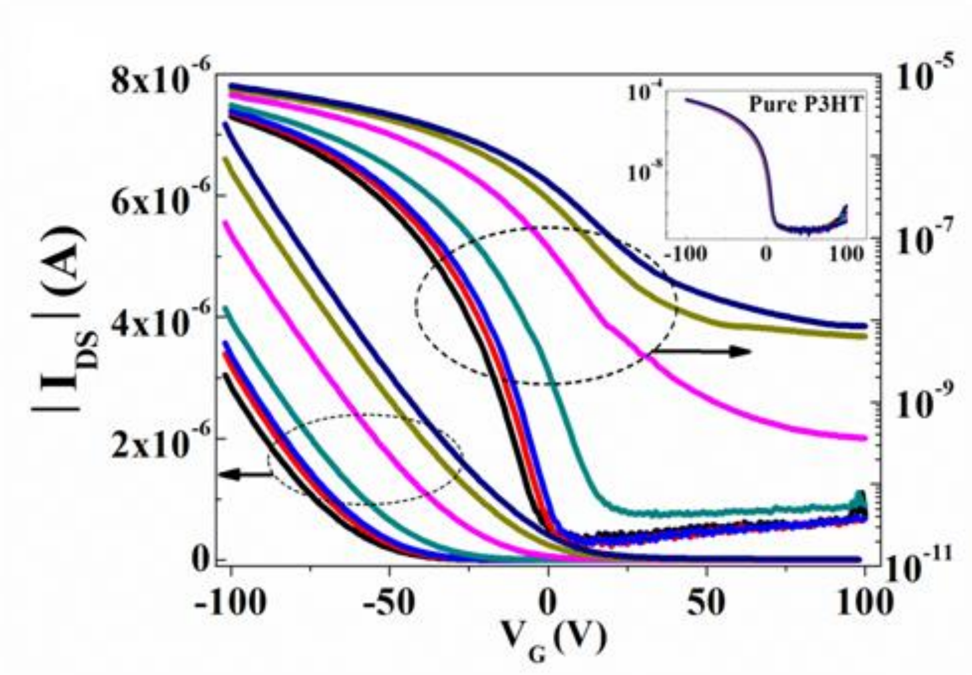

Figure 4.7 The transfer curves of a phototransistor under NIR light illumination (wavelength: 895nm). V_{DS} = -100V. From left to right curves, the corresponding light irradiance is: 0, 0.23μW/cm^2, 13.7μW/cm^2, 0.56mW/cm^2, 5.11mW/cm^2, 10.4 mW/cm^2 and 13.5mW/cm^2, respectively. Inset: transfer curves of pure P3HT transistor under light illumination.

The transfer characteristics of a phototransistor under different NIR light irradiance are shown in Figure 4.7. The hole mobility is about 0.01 cm^2/Vs in the device. The transfer curves shift to positive voltage horizontally with the increase of light irradiance, which is consistent with the results of such hybrid phototransistors reported before [47, 48]. However, the control OTFT sample with pure P3HT shows almost no change of the transfer curve under NIR light illumination as presented in the inset of Figure 4.7, indicating that the PbS QDs play a key role in the photosensitive behavior of the device.

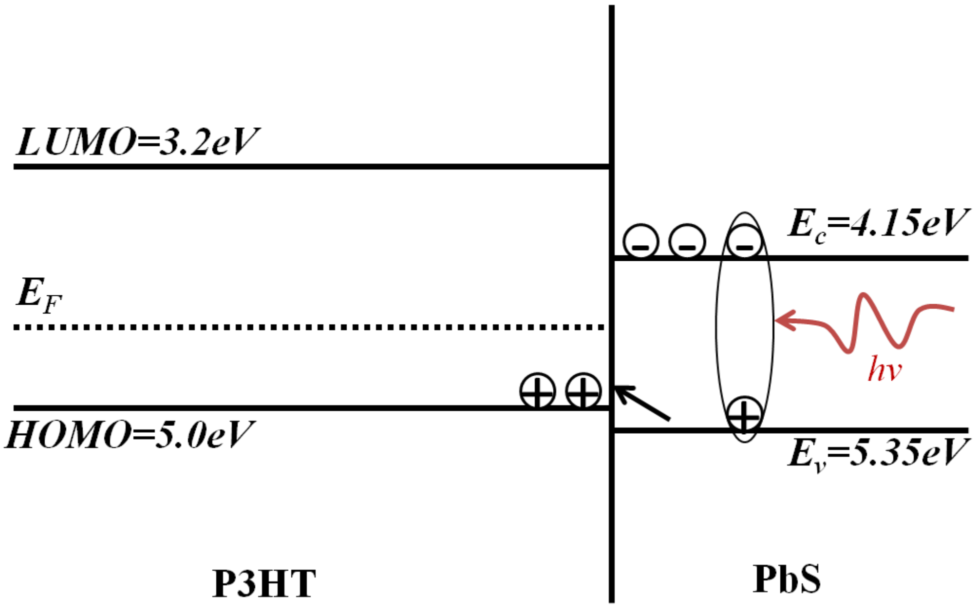

Figure 4.8 Schematic of charge transfer at the P3HT/PbS QDs heterojunction under NIR illumination.

As discussed before, the energy levels of the conduction (E_c) and valence (E_v) bands of PbS QDs are estimated to be 4.15 eV and 5.35 eV, respectively. The photosensitive mechanism of the phototransistor is illustrated in Figure 4.8. Under NIR light illumination, electron/hole pairs (excitons) are generated in PbS QDs and then dissociate at the interface of P3HT/PbS QDs. The holes can transfer to the P3HT film and induce p-type doping since the valance band (E_v) level of PbS QDs is lower than the highest occupied molecular orbit (HOMO) level of P3HT. On the other hand, the electrons in the PbS QDs can decrease the electrostatic potential of the active layer of the transistor [47], which lead to the increase of the threshold voltage of the device, as indicated by the transfer curve of the device shown in Figure 4.7. This phenomenon is similar to the hybrid P3HT/TiO_2 phototransistors reported before [47, 48]. The response of the phototransistor to light illumination is mainly due to the modulation of the threshold voltage or effective gate voltage applied on the transistor [48, 192]. The shift of the transfer curves (ΔV_G) of the device as a function of light irradiance (E_e) is shown in Figure 4.9. In high light irradiance region, the curve can be fitted very well with the equation 3-1 [47]: $\Delta V_G = \alpha E_e^{\beta}$, where α and β are constants and $\beta \approx 0.28$. It is noteworthy that visible and ultraviolet phototransistors based on P3HT/TiO$_2$ composites have been investigated before [47, 48, 88] and the equation 3-1 was successfully used in those phototransistors.

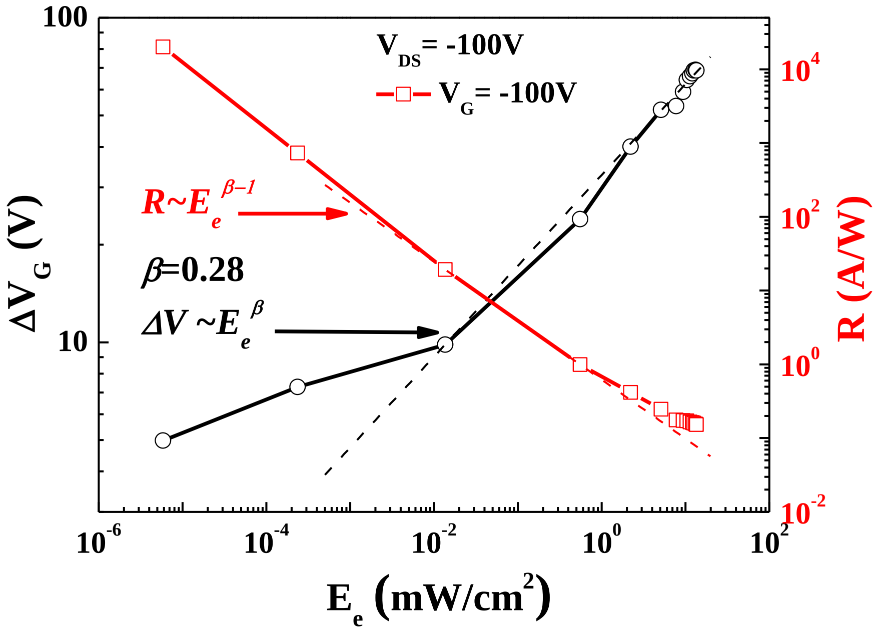

Figure 4.9 The horizontal shift of transfer curves (ΔV_G) and the responsivity (R) as functions of light irradiance (E_e).

The channel current change (ΔI_{DS}) of the P3HT/PbS QDs transistor under light illumination is given by [221]:

$$\Delta I_{DS} = \frac{W}{L} C_i \mu \Delta V_G V_{DS} \qquad 4\text{-}1$$

where C_i is the capacitance of the gate dielectric per unit area, W and L are width and length of the channel, respectively. So from equation 2-1, the responsivity (R) of the device is given by:

$$R = \frac{\Delta I_{DS}}{WLE_e} = \frac{C_i \mu \Delta V_G V_{DS}}{L^2 E_e} = \frac{\alpha C_i \mu V_{DS}}{L^2} E_e^{\beta - 1} \qquad 4\text{-}2$$

Figure 4.9 also shows the responsivity of the device versus light irradiance when V_G is equal to -100V, which can be fitted very well with equation 4-2. The responsivity of the phototransistor decreases with the increase of irradiance and shows a nonlinear relationship. It is notable that the maximum responsivity of the device at low light irradiance (5.85nW/cm^2) is about 2×10^4 A/W, which is one order of magnitude higher than that of the NIR photoconductor based on PbS QDs [52].

Photoswitching ratio P of a phototransistor is given by equation 2-2: $P = \frac{I_{ill} - I_{Dark}}{I_{Dark}} = \frac{\Delta I_{DS}}{I_{Dark}}$. The responsivity and photoswitching ratio as functions of gate voltage of the device (R~V_G and P~V_G curves) are shown in Figure 4.10. It can be found that the responsivity R reaches to its maximum value at the largest negative V_G while the photoswitching ratio P shows its maximum value when the gate voltage is around the threshold voltage. This result is consistent with some other organic phototransistors [58, 66].

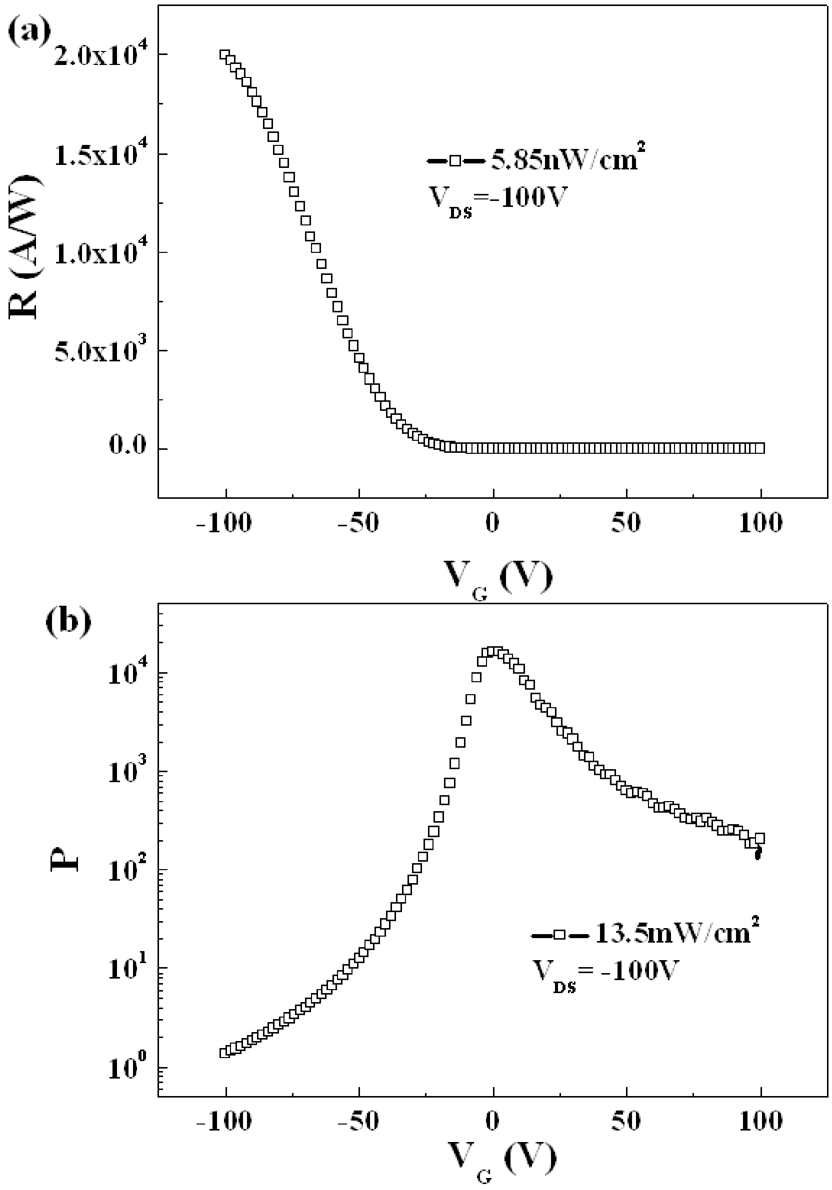

Figure 4.10 (a) Photoresponsivity (R) as a function of gate voltage (V_G) when irradiance is 5.85 nW/cm^2. (b) Photoswitching ratio (P) at different gate voltages when irradiance is 13.5mW/cm^2.

Next, the current response of this phototransistor to on/off light illumination was characterized.Figure 4.11 shows the channel current change (ΔI_{DS}) of the device under light illumination in one on/off cycle. ΔI_{DS} increases with the illumination time and can be fitted well with an exponential function of one relaxation time (τ_1): $\Delta I_{DS} = \Delta I_1(1 - \exp(-t/\tau_1)$ [48, 205]. The time constant τ_1 is 0.23s. We speculate that this relaxation time τ corresponds to the hole transfer from PbS to P3HT matrix. Similarly, the channel current decreases with time when the light is switched off and the curve can be fitted with an exponential function: $\Delta I_{DS} = \Delta I_3 \exp(-t/\tau_2) + \Delta I_4 \exp(-t/\tau_3)$ with two decay times: τ_2 = 0.21s and τ_3 = 2.7 s. The recovery of the channel current is obviously dominated by the recombination process of the electron and holes at the interface of P3HT/PbS QDs [47, 48].

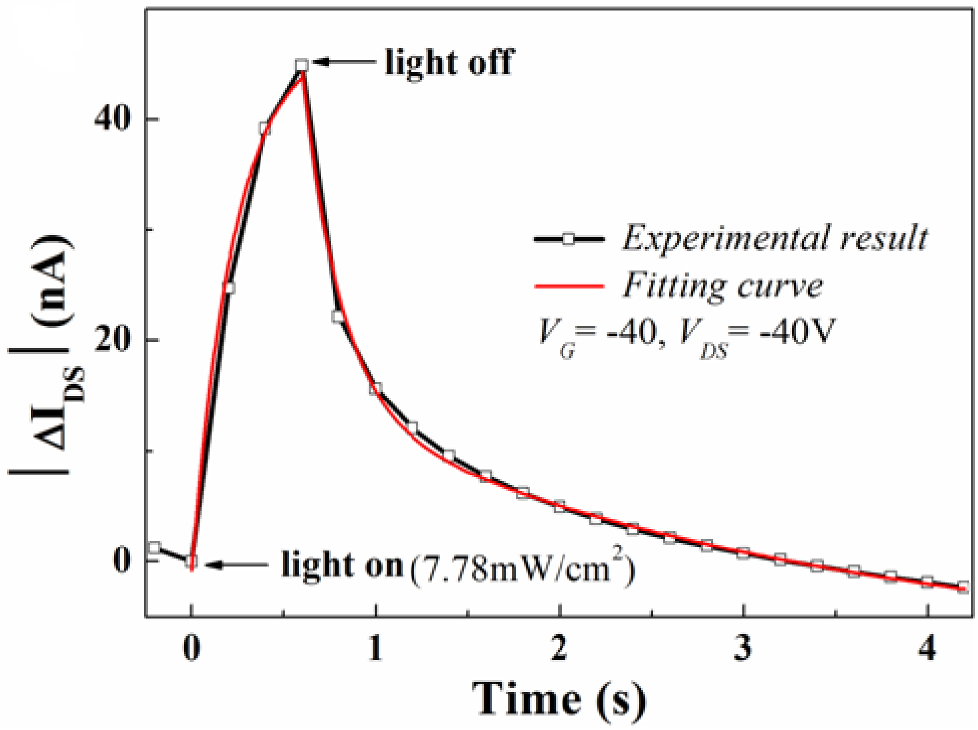

Figure 4.11 Current response of the hybrid NIR phototransistor to IR illumination with an on/off cycle.

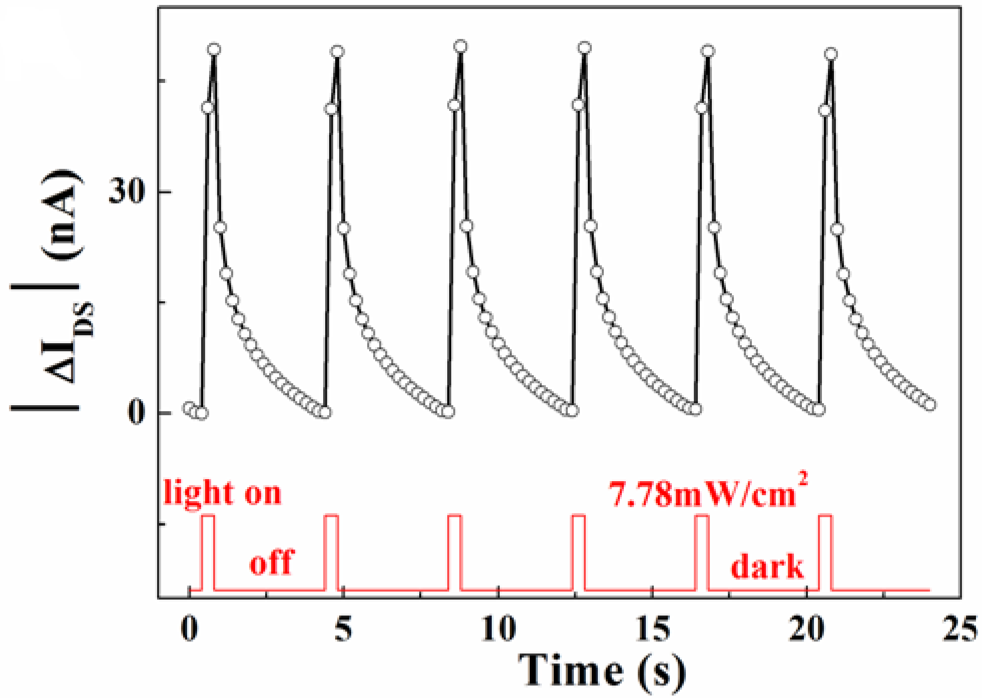

Figure 4.12 The current response of the phototransistor to NIR illumination (irradiance: 7.78mW/cm^2) with V_{DS}=-40V and V_G=-40V. Light signal width is 400ms and pulse frequency is 0.25Hz. The black square line (top) is the experimental current and the red line (bottom) is the schematic of light pulse。

The current response of the device under repeated NIR light illumination (wavelength: 895nm) was characterized and showed in Figure 4.12. The channel current I_{DS} increased for about 50nA in less 400ms and recovered to its original level in several seconds. This behavior can be repeated for many cycles with stable performance.

4.4 Summary

P3HT/PbS QDs hybrid film was used as the active layer of a NIR phototransistor. The responsivity up to 2×10^4 A/W was observed at low light intensity at the wavelength of 895nm, which is much higher than that of the photoconductor based on only PbS QDs or organic semiconductors [52, 76, 214]. The photosensitive behavior can be attributed to charge transfer from PbS QDs to P3HT matrix under NIR light illumination. The net negative charges accumulated in PbS QDs can decrease the electrostatic potential of the channel and increase the threshold voltage of the transistor. The phototransistor shows repeatable performance under NIR light illumination for many cycles. This kind of phototransistors may have promising applications in infrared sensors for its high sensitivity, easy fabrication and flexibility.

Chapter 5 **Infrared Photodetectors Based on CVD-grown Graphene and PbS Quantum Dots with Ultrahigh Responsivity**

5.1 **Introduction**

Infrared (IR) photodetectors are highly desired for various demanding applications including telecommunication, thermal imaging, biological imaging, remote sensing and so forth [10, 32]. In recent years, IR photo detectors based on quantum walls [10], quantum dots (QDs) [10, 16, 32, 213], graphene [49, 77, 215, 224] organic semiconductors [76, 214] and carbon nanotubes [225] have been extensively studied. The advantages of using colloidal QDs in IR sensors include solution processability, low cost, tunable wavelength, and high responsivity [32]. It is notable that the record responsivity of IR sensors based on PbS QDs is about 2,700A/W, which is comparable to those of photoconductors based on single crystalline silicon [52]. As addressed above, the two main types of IR photodetectors are photodiodes and photoconductors [32, 221]. IR photodiodes have fast response but low gains (quantum efficiencies) that are normally less than 1 [10, 221]. Photoconductors have the conductance that can be modulated by light illumination [52]. A photoconductor can have a gain much higher than one because carriers can circulate in the conductor between two electrodes for many times before their recombination with opposite charges [32, 221]. A field effect phototransistor also can be regarded as a type of photoconductor [48, 88, 89, 221]. The photocurrent I_p across a thin film photoconductor is given by $I_p = en\mu EW$, where e is electronic charge, n density of photo-induced carriers per unit area, μ carrier mobility, E the applied electric field and W the width of the device [221]. Therefore, the gain and the responsivity of the photoconductor are proportional to the carrier mobility μ. However, the maximum carrier mobility in QDs is only about 0.1 cm^2/Vs [32], which is much lower than those of silicon, carbon nanotubes, graphene, ZnO and some organic semiconductors [127, 217, 225-227].

Graphene being a sheet of two dimensional carbon atoms with a hexagonal honeycomb lattice has aroused considerable interest because of the behavior of Dirac Fermions and the extremely high carrier mobilities up to 200,000cm^2/Vs [127]. Graphene transistors have been used as ultrafast IR photodetectors for high-speed optical communications because of the high carrier mobility and light absorption in a broad wavelength region [49, 85]. However, the responsivity of the IR detectors are very low (≤ 6.1 mA/W) for the low light absorbance of graphene (~ 2.3% for single layer graphene). Therefore they can only be used for detecting IR light with high intensity [85]. Moreover, it has been reported that hot carrier effect instead of photovoltaic effect was found to be the main reason for the photoresponse of graphene

[228, 229]. Recently, Chitara *et al.* reported the IR photoconductors based on reduced graphene oxide or graphene nanoribbons, which show the responsivities up to 1 A/W [215]. Therefore, graphene-based IR detectors have much lower responsivities than that of a photoconductor based on QDs.

It is reasonable to consider that the responsivity of a graphene-based IR detector can be improved substantially by modifying the graphene film with QDs, which can absorb IR light more efficiently. On the other hand, for a QD-based IR detector, if the carriers generated by IR light can transfer to graphene film, their mobility will be much higher and thus the responsivity of the detector will be dramatically improved. Moreover, an array of graphene devices can be easily patterned by facile techniques, which could eliminate the possible crosstalk between neighbouring pixels that occurs in silicon devices [52, 230].

Until very recently, phototransistors with ultrahigh responsivity up to 10^7 A/W based on mechanically exfoliated single or bilayer graphene flakes and PbS QDs modified with ethanedithiol were reported [51]. However, exfoliated graphene is not compatible with large area fabrication. In this regard, devices based on chemical vapor deposition (CVD) grown graphene is more suitable for practical applications. In this chapter, we report the near infrared (NIR) photoconductors based on CVD grown single-layer graphene coated with PbS QDs by solution process. The devices were fabricated on various substrates, including flexible ones, by solution process and showed vey high responsivities up to 10^7 A/W, which is much higher than that of the visible-light detector based on CVD grown graphene and PbS thin film prepared by electron beam deposition reported very recently [50]. The sensing mechanism is attributed to the charges that are generated in PbS QDs under NIR light, which can modulate the Fermi level and thus the conductivity of the underlying graphene film. In addition, the ligand capped on the surface of the QDs was found to be critical to the photo responsivity of the device since charge transfer from QDs to graphene film was dominated by the ligand layer.

5.2 Expermental

5.2.1 Materials

Graphene: Single-layer graphene was synthesised on copper foils by CVD method and then transferred on substrates with the typical method as follows [85, 230]. Firstly, a thin layer (~300 nm) of Poly(methyl methacrylate) (PMMA) was spin-coated on the graphene side of Cu foil and then the foil was annealed at 100 ^{o}C for about 30 min. Subsequently, the foil was put in an aqueous solution of iron chloride at room temperature. After 2 hours, Cu underneath the graphene/PMMA was etched away and a visible thin film was floated on the surface of the solution. The graphene/PMMA film was then transferred to distilled water. Next, a substrate was placed in the water underneath the floating thin film to get the PMMA/graphene layer adhered to the surface of the substrate. Then the sample was taken out of water and dried for several minutes followed by the treatment of acetone to remove the PMMA on top of the graphene film.

Lead Sulphide Quantum Dots (PbS QDs): PbS QDs capped with oleic acid were purchased from Evident Technologies Inc, USA. The specific of the PbS QDs can be found in chapter 4.2.1. Ligand exchange of the oleic acid on PbS QDs to pyridine was carried out by the same method in chapter 4.2.1.

5.2.2 Device Fabrications

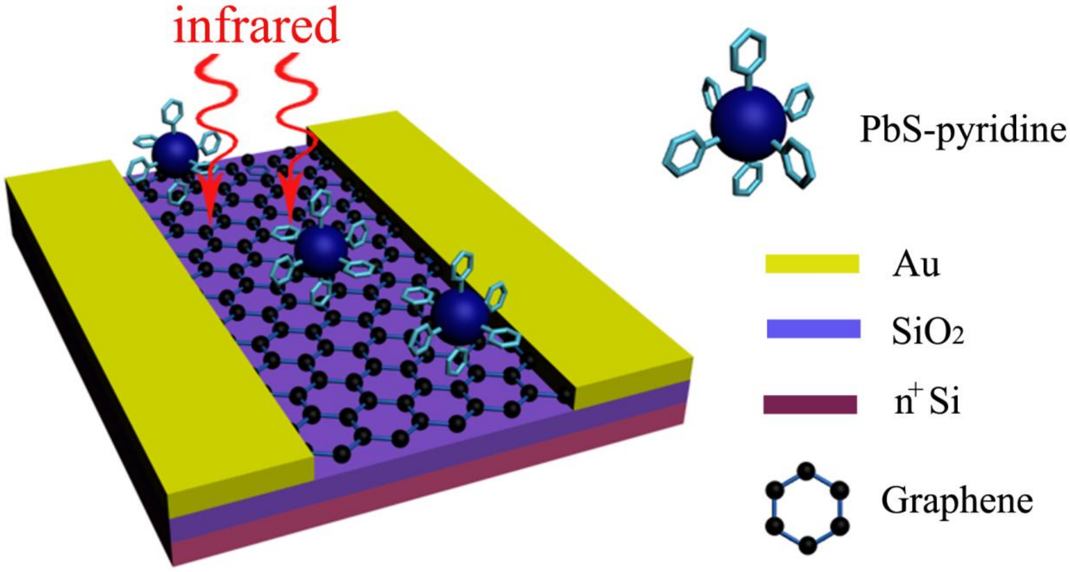

Figure 5.1 Structure of the photodetector based on graphene/PbS QDs hybrid films.

Graphene was transferred and patterned on n+Si/SiO$_2$ substrate by photolithography [229]. The thickness of SiO$_2$ is 300nm.Then Au source and drain electrodes were deposited on top of the graphene film through a shadow mask by thermal evaporation and formed a channel of W/L=2mm/0.1mm. Then PbS QD solution was dropped on the surface and dried in a glovebox filled with high purity Nitrogen gas.

Figure 5.1 shows the structure of a final photodetector based on graphene/PbS QDs hybrid film. When the gate voltage is zero, it can be regarded as a photoconductor. Otherwise it is a phototransistor. The flexible photoconductors were fabricated on polyethylene terephthalate (PET) substrates with the thickness of 150 μm, with the same graphene transfer and device fabrication procedures.

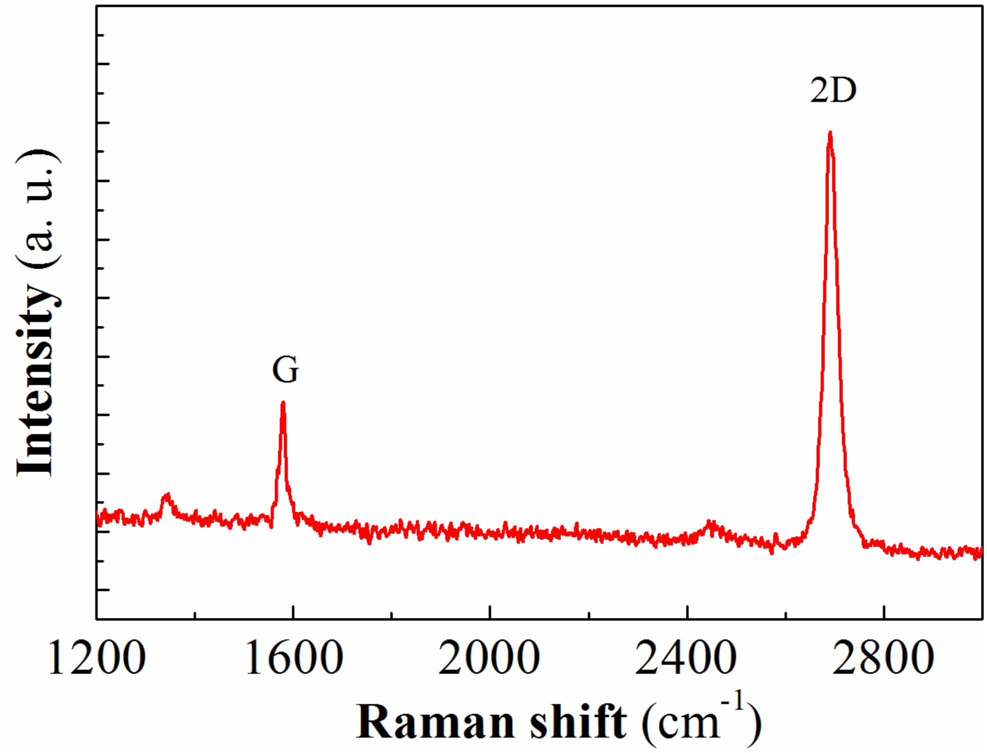

Figure 5.2 Raman spectrum of single layer graphene on Si/SiO_2 substrate.

Raman spectrum: The single-layer graphene on n+Si/SiO_2 substrate was characterized by Raman spectroscopy (HORIBA, 488nm laser source) to show the monolayer property, the Raman spectrum as shown in Figure 5.2 [231].

Atomic Force Microscopy (AFM): Surface morphology of graphene film and hybrid film were characterized by AFM (Veeco Instruments Inc.). Their AFM images are shown in Figure 5.3. The roughness (r.m.s.) of the pristine graphene film is about 0.25nm, which is similar to the roughness of single-layer graphene reported before [232].

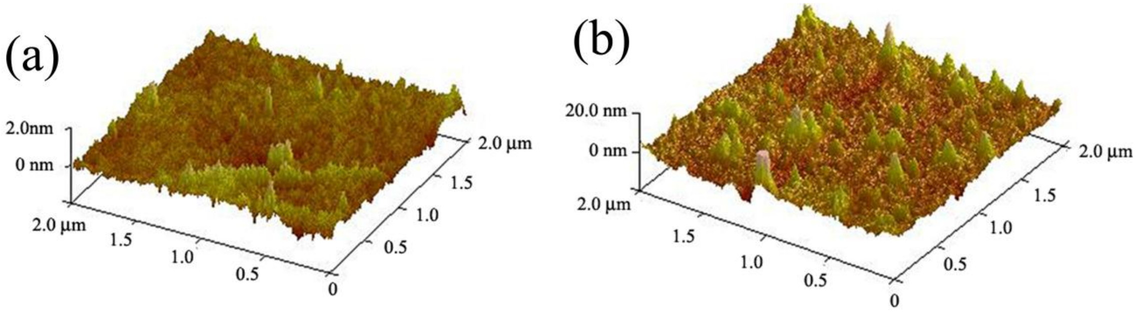

Figure 5.3 Atomic Force Microscopy (AFM) images of pristine single layer graphene film (a) and graphene/PbS QDs hybrid film (b).

Figure 5.3b shows the AFM images of the single-layer graphene after being coated with PbS QDs capped with pyridine. The film becomes very rough after being coated with QDs and the roughness (r.m.s.) is about 2.7 nm.

Transmission Electron Microscopy (TEM): Figure 5.4a shows the transmission (TEM 2100F, Japan) image of the QDs on the surface of a graphene film. We can find that the average size of the PbS QDs is ~4nm and the distribution on graphene is relatively uniform. The electron diffraction pattern of a graphene/PbS QDs hybrid film is shown the insert of Figure 5.4b.

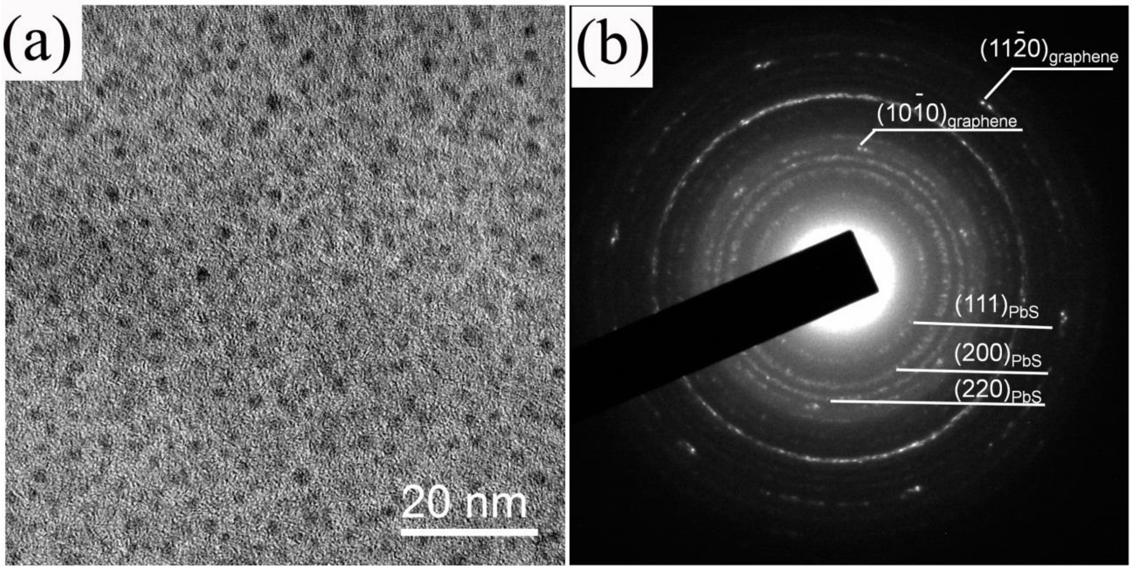

Figure 5.4 (a) Transmission Electron Microscopy (TEM) image of the QDs on the surface of a graphene film. (b) Electron diffraction pattern of a graphene/PbS QDs hybrid film.

5.2.3 **Measurement of Devices**

The graphene transistor was characterized by a semiconductor parameter analyzer (Agilent 4156C) under light illumination with different irradiance in the glovebox. The light sources were monochromatic LED with the wavelength of 895 nm with its light irradiance controlled by a DC power source. The glovebox is full of high purity N_2 and the voltages were applied on every electrode by a probes system.

Photoresponse measurements were carried out with infrared from upside, as shown in Figure 5.1. For the transfer and output characteristics, light illumination at different irradiance was kept for 2 minutes before every measurement.

The flexible photodetectors based on graphene/PbS QDs on PETs were characterized before and after bending tests. In the bending tests, the flexible sample was pressed to the radius of ~4 mm and released for up to 1,000 times, as shown in Figure 5.5.

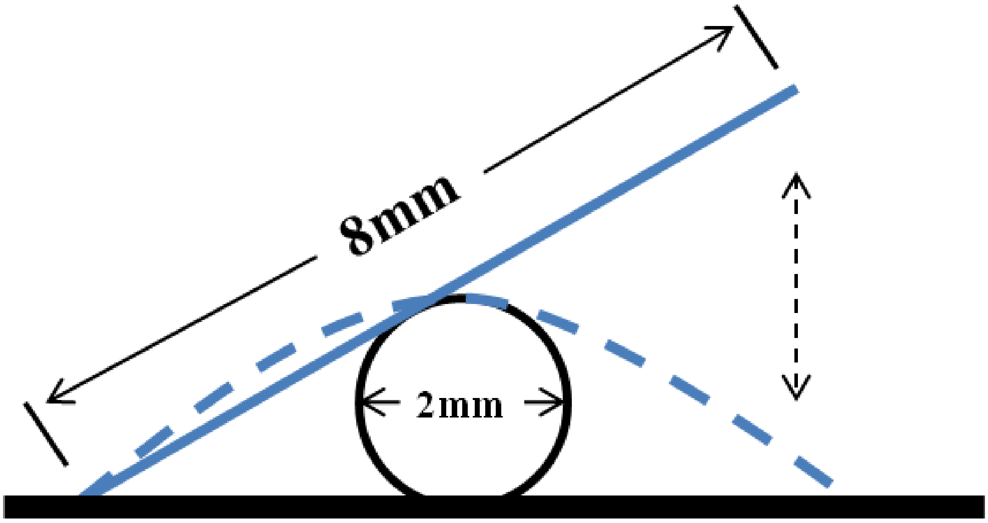

Figure 5.5 Bending operation of the flexible devices.

5.3 Performance of Devices

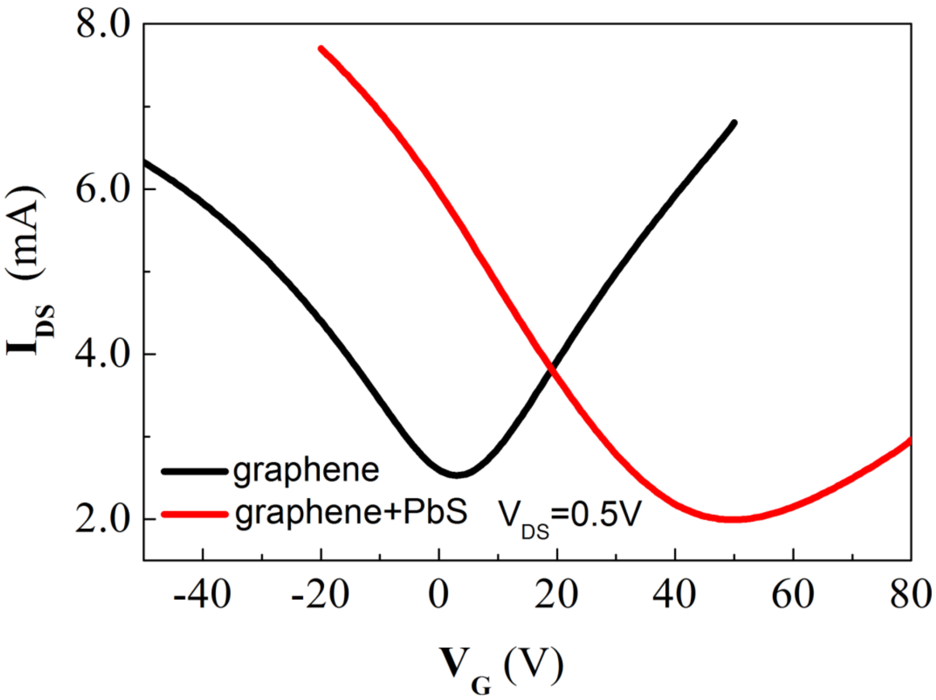

Figure 5.6 Transfer characteristics ($I_{DS} \sim V_G$, $V_{DS} = 0.5\text{V}$) of graphene transistors with or without the modification of PbS QDs on the graphene film.

For the phototransistors based on graphene/PbS QDs hybrid films, before coating PbS

QDs, the field effects of the pure graphene films were characterized. The transfer characteristic ($I_{DS} \sim V_G$, $V_{DS} = 0.5V$) of the transistor measured in dark is show in Figure 5.6. The field effect mobilities are ~1,000 cm^2/Vs for both electrons and holes, which are higher than those of many other semiconductors [127, 217, 226, 227]. Figure 5.6 also shows the transfer curve of the graphene transistor modified with PbS QDs and measured in dark. It is notable that the transfer curve becomes asymmetric and the Dirac point shifts to a positive gate voltage (~50 V) after the modification, indicating a p-type doping in the graphene film [132, 233]. In addition, the electron mobility is decreased to ~ 440 cm^2/Vs while hole mobility remains unchanged.

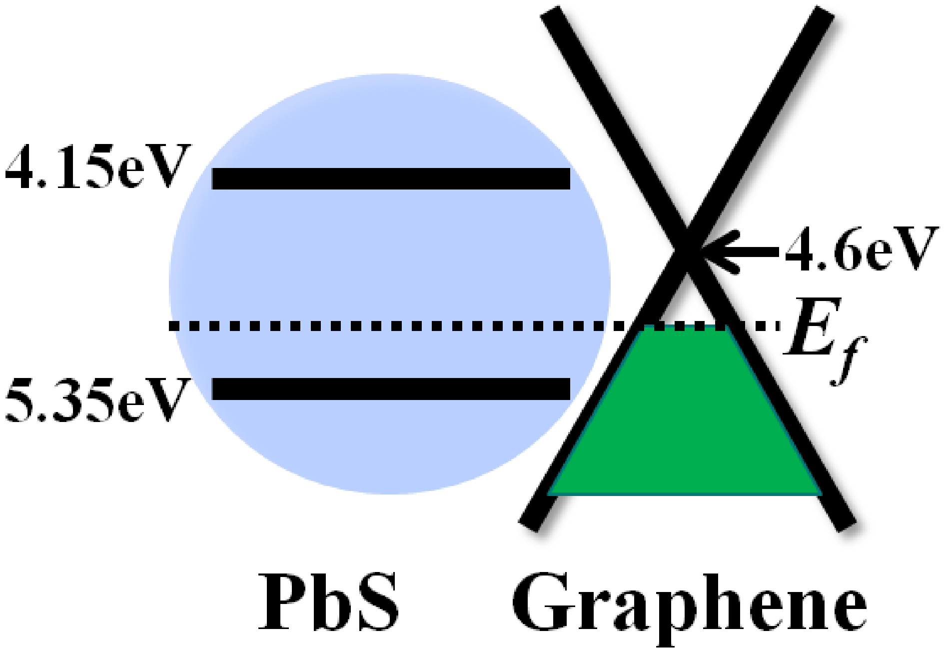

Figure 5.7 Energy diagram of the heterojunction of PbS QDs and graphene.

As mentioned above, energy levels for the conduction and valence bands of PbS QDs are estimated to be 4.15 eV and 5.35 eV, respectively, as shown in Figure 5.7. It is notable that PbS QD is a p-type semiconductor which has the Fermi energy close to its valence band [234]. However, the Fermi level of intrinsic graphene is about 4.6 eV at the Dirac point [231]. Therefore, holes in PbS will inject into the graphene film and induce a p-type doping effect in graphene in the heterojunction of graphene/PbS QD [132]. On the other hand, the decrease of the Fermi level in graphene may induce bigger contact resistances for electron injection and lead to the decrease of the effective electron mobility of the transistor as shown in Figure 5.6 [235].

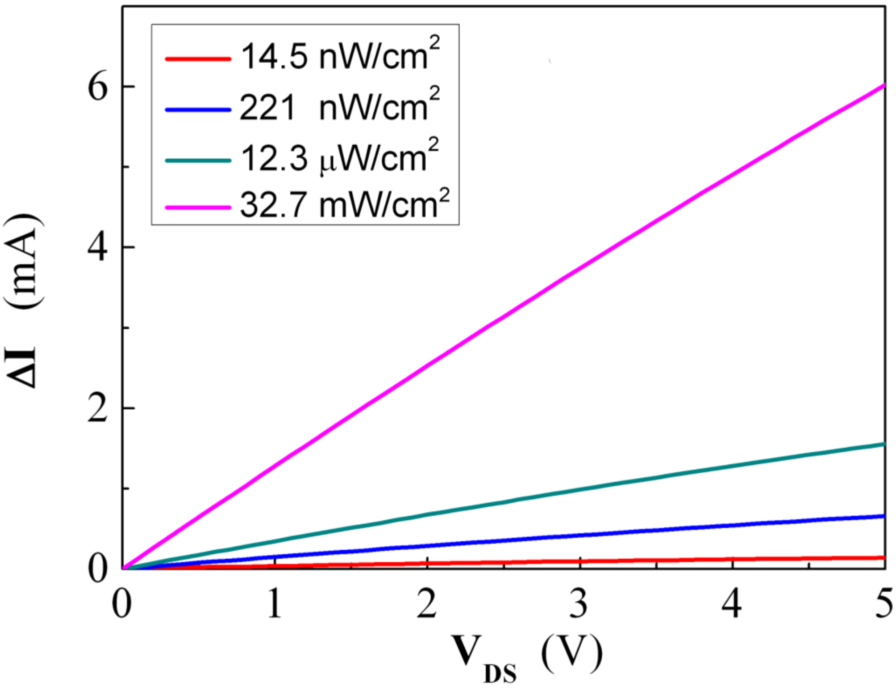

Figure 5.8 Photocurrent of a graphene/PbS QDs photoconductor as functions of applied voltage characterized under different light irradiance. Wavelength: 895nm.

Next the graphene/PbS QDs phototransistors were characterized under the illumination of NIR light with the wavelength of about 895nm. Firstly, no gate voltage was applied on the transistor ($V_G = 0$ V) and thus the device could be regarded as a standard photoconductor. Figure 5.8 and Figure 5.9 show the photocurrent and the responsivity of the device to NIR light as a function of the voltage applied between the source and drain electrodes (V_{DS}). The responsivity increases with the increase of V_{DS} and decreases with the increase of the light irradiance, which is consistent with the QD IR sensors reported before [52].

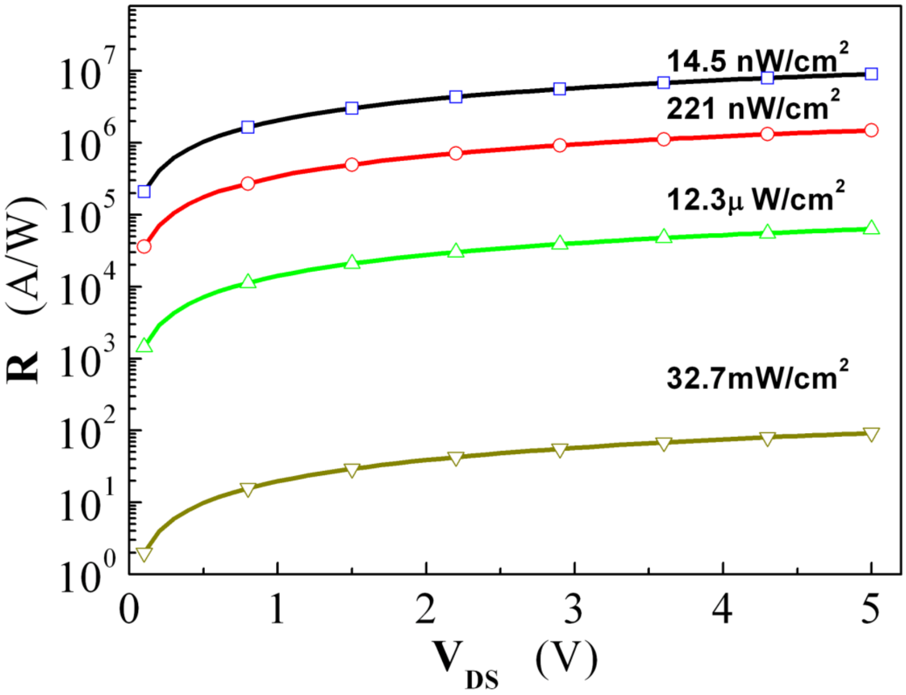

Figure 5.9 Responsivity of a graphene/PbS QDs photoconductor as functions of applied voltage characterized under different light irradiance. Wavelength: 895nm.

It is notable that the maximum responsivity of the detector is about 1×10^7 A/W at the incident power of about 30pW, which is several orders of magnitude higher than that of the QD IR sensors reported before [32, 52]. Since the carrier mobility of graphene is more than four orders of magnitude higher than that of PbS QD films, it is reasonable to observe the ultrahigh responsivity in the devices.

To better understand the sensing mechanism, we characterized the transfer characteristics of the NIR phototransistor on n^+Si/SiO_2 substrate under light illumination with different irradiance. As shown in Figure 5.10, the transfer curves shift to higher gate voltage horizontally with the increase of light irradiance. It is notable that the hole mobility has little change under light illumination. Therefore, the response of the phototransistor to light illumination is mainly due to the modulation of the effective gate voltage applied on the transistor [47, 48].

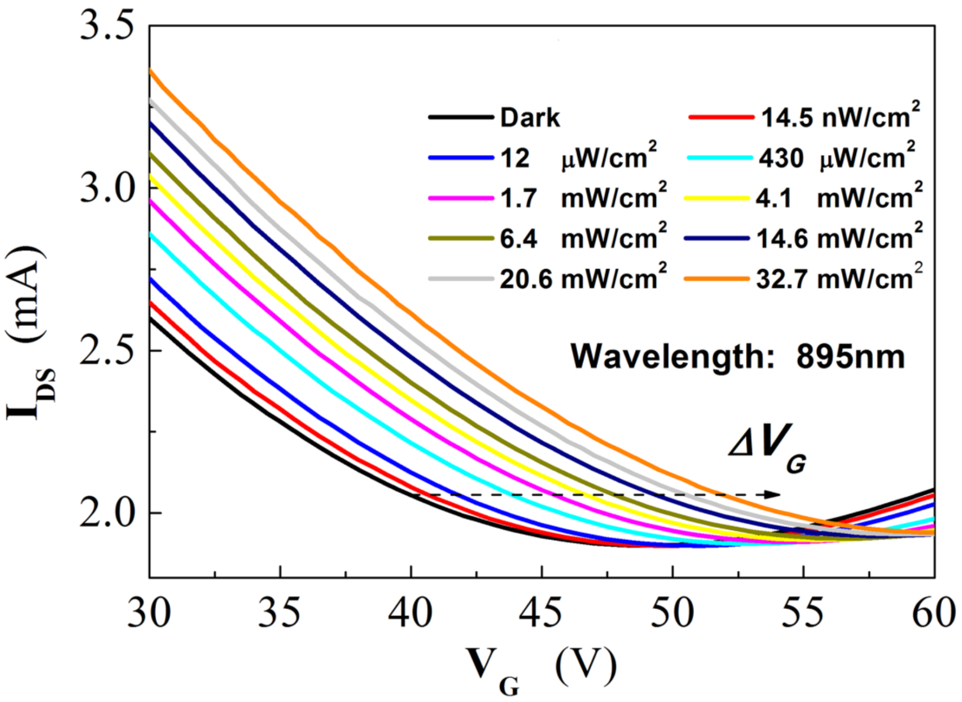

Figure 5.10 Transfer characteristics ($I_{DS} \sim V_G$, V_{DS} = 0.5V) of a graphene/PbS QDs transistor characterized under different light irradiance with the wavelengths of 895nm.

The shift of the transfer curve (ΔV_G) of the device as a function of light irradiance (E_e) is shown in Figure 5.11. Similar with the P3HT/PbS QDs phototransistor, the curve can be fitted very well with the equation 3-1: $\Delta V_G = \alpha E_e{}^{\beta}$, where α and β are constants and $\beta \approx 0.24$. It is worthy of note that this value is similar with the fitting result of P3HT/PbS QDs phototransistor, which is 0.28. Besides, this equation was also successfully used in other phototransistors based on organic/inorganic composites reported before [47, 221].

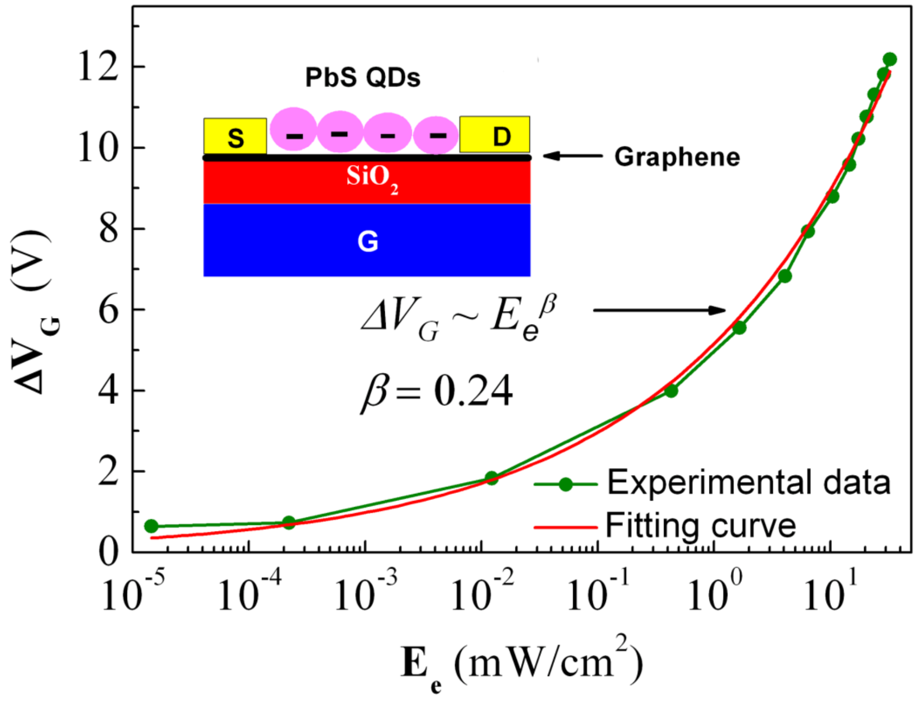

Figure 5.11 Horizontal shift of transfer curves as functions of light irradiance and its fitting result. The inset is the schematic of the net negative charge in PbS QDs under illumination.

The channel current change (ΔI_{DS}) of the graphene/PbS QDs transistor under light illumination is given by equation 4-1 [221]: $\Delta I_{DS} = \frac{W}{L} C_i \mu \Delta V_G V_{DS}$. And the responsivity (R) of the device is given by equation 4-2: $R = \frac{\Delta I_{DS}}{WLE_e} = \frac{C_i \mu \Delta V_G V_{DS}}{L^2 E_e} = \frac{\alpha C_i \mu V_{DS}}{L^2} E_e^{\beta-1}$. Figure 5.12 shows the responsivity of the device versus light irradiance, which can be fitted very well with the equation 4-2. We can find that the responsivity of the phototransistor decreases with the increase of irradiance and shows a nonlinear relationship, which is similar to the IR photoconductor based on PbS QDs reported before [52].

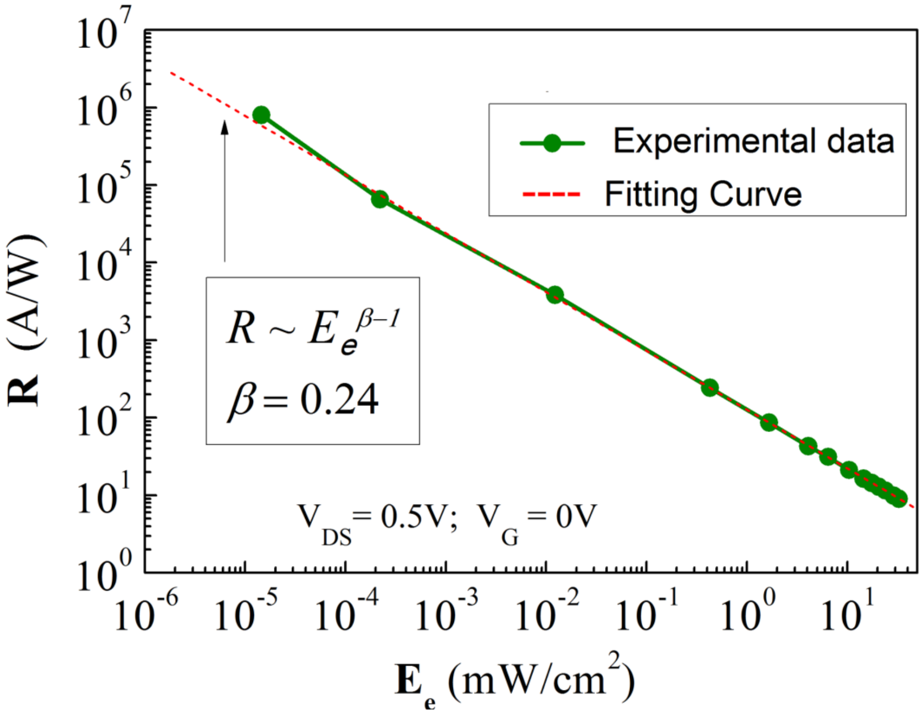

Figure 5.12 Responsivity as functions of light irradiance and its fitting result.

With the same device design and graphene quality, we fabricated a control device which is a graphene transistor without PbS QDs. This control device was measured in illumination and showed very little response to the NIR light, as shown in Figure 5.13. Therefore it can be concluded that PbS QDs play a crucial role on the photosensitive behavior of the device.

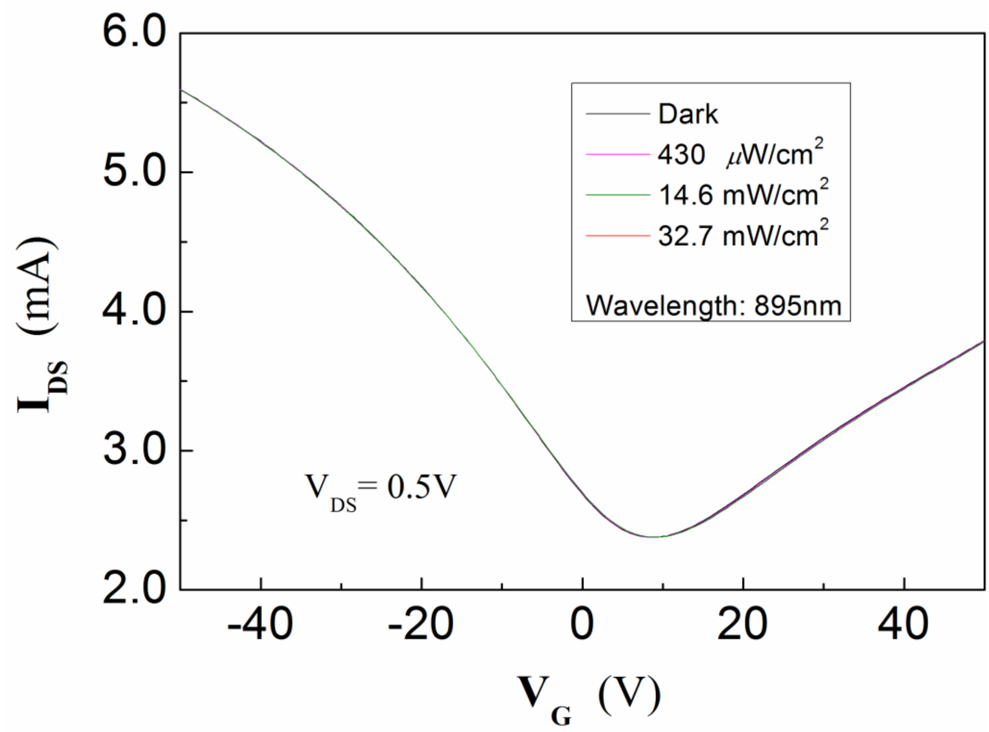

Figure 5.13 Transfer characteristics ($I_{DS} \sim V_G$, V_{DS} = 0.5V) of a graphene transistor under IR light illumination with different irradiance.

The sensing mechanism of the graphene/PbS QDs phototransistor can be attributed to the charge transfer between PbS QDs and graphene. As shown in Figure 5.14, electron/hole pairs (excitons) are generated in PbS QDs under light illumination and then transfer to the graphene film due to the lower energy levels for both electrons and holes in graphene. Because the transfer rates of the electrons and holes are different, the numbers of electrons and holes in a QD will be different, which result in a net negative or positive charge in the QD. As shown in Figure 5.10, the transfer curves shift to positive voltage horizontally under light illumination, indicating that QDs have net negative charges that can attract more holes in the graphene film, as shown in the inset of Figure 5.11. In other words, higher gate voltage is needed to obtain the charge neutrality point (Dirac point) in the graphene transistor because of the net negative charges in the QDs.

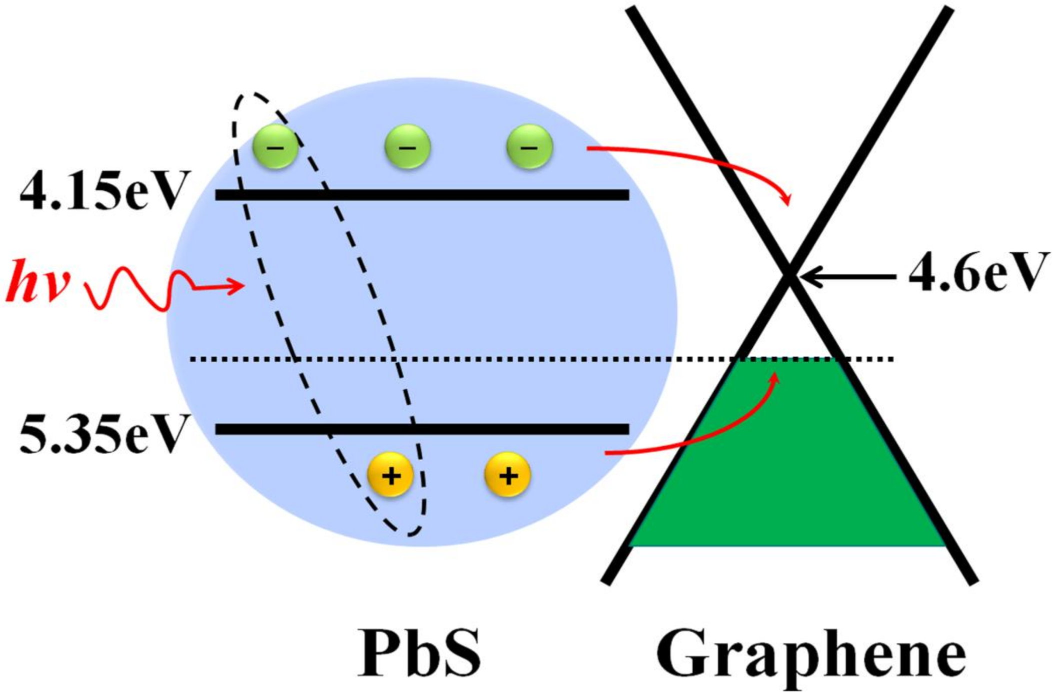

Figure 5.14 Schematic diagram for charge generation in a graphene/PbS QD heterojunction under light illumination.

The responsivity of the phototransistor was found to be influenced by the amount of PbS QDs. As shown in Figure 5.15, the shift (ΔV_G) of the transfer curve increases with the increase of the thickness of the PbS QD layer under the same light irradiance (E_e = 32.7 mW/cm^2) and tends to saturate when the thickness is bigger than 150nm. Therefore, all of the devices mentioned elsewhere have the QD layers of about 150 nm thick unless are otherwise specialized.

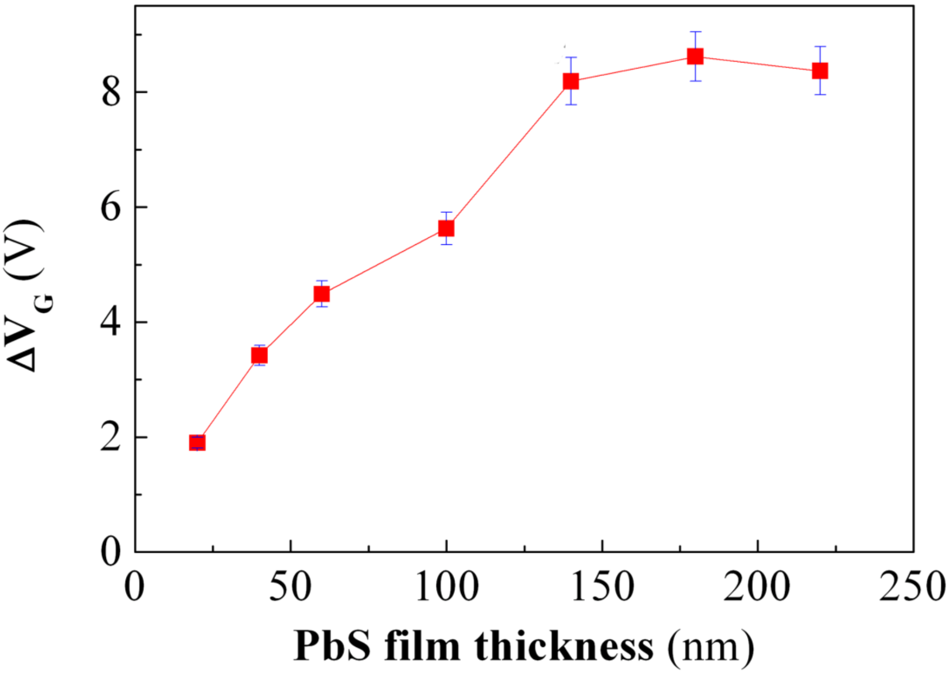

Figure 5.15 Horizontal shift of the transfer curves of the devices with different thicknesses of PbS QDs layers. Light irradiance: 32.7 mW/cm^2, wavelength: 895 nm.

In addition, the surface modification on the PbS QDs can influence the charge transfer from PbS to graphene. We found that the graphene transistor coated with PbS QDs modified with oleic acid showed much lower sensitivity to IR light as shown in Figure 5.16. Because oleic acid has a relatively long molecule chain compared with pyridine, charge transfer from oleic acid-capped PbS QDs to graphene is rather difficult and thus the photosensitivity becomes much lower [52]. In the phototransistors reported by Konstantatos et al. [51], PbS QDs were modified with ethanedithiol, which has the similar length of pyridine. Therefore it is reasonable to find the similar responsivity of our device to the reported one.

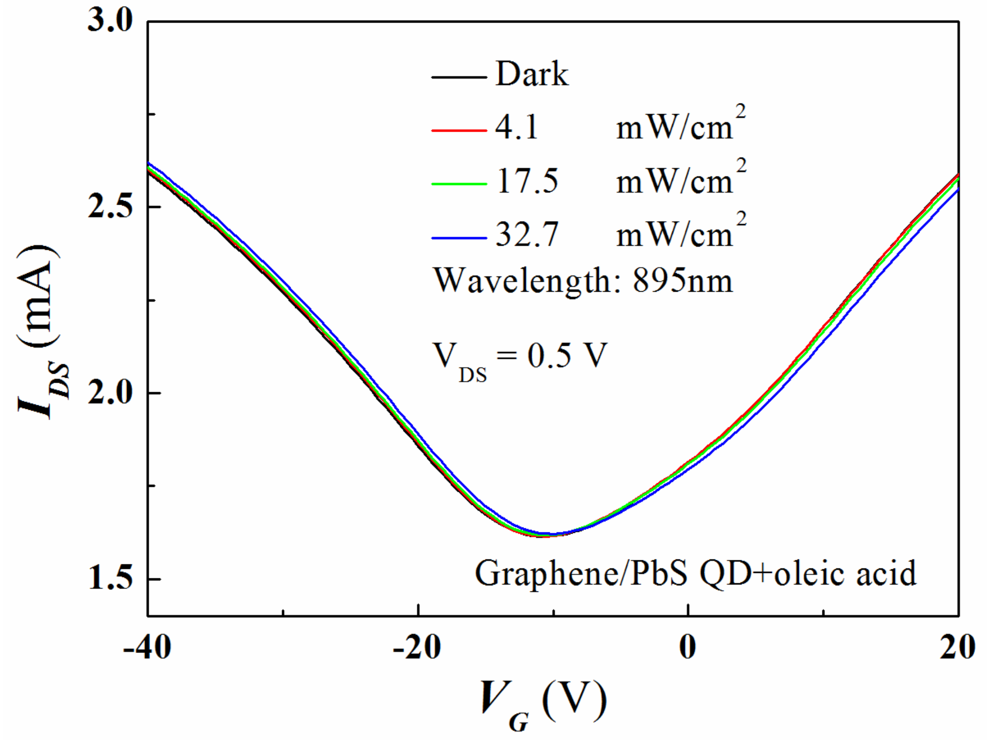

Figure 5.16 Transfer characteristics ($I_{DS} \sim V_G$, V_{DS} = 0.5V) of a graphene/PbS QDs transistor under IR light illumination with different irradiance. The PbS QDs are capped with oleic acid.

Next, the transient behavior of the grapheme/PbS QDs phototransistor was characterized. Figure 5.17 shows the response of the channel current of a device under light illumination. The channel current increases with the illumination time and can be fitted with an exponential function with two relaxation times: $\Delta I_{DS} = \Delta I_1(1-\exp(-t/\tau_1)) + \Delta I_2(1-\exp(-t/\tau_2))$, which is similar to many phototransistors reported before [47, 215]. The time constant τ_1 and τ_2 are 0.13s and 5.0 s, respectively. We speculate that the short relaxation time τ_1 corresponds to the hole transfer from PbS to graphene while the long relaxation time τ_2 represents the charge transfer in PbS QDs layer. Similarly, the channel current decreases with time when the light is switched off and the curve can be fitted with an exponential function: $\Delta I_{DS} = \Delta I_3 \exp(-t/\tau_3) + \Delta I_4 \exp(-t/\tau_4)$ with two decay times: τ_3 = 0.25s and τ_4 = 5.0 s. It is notable that τ_4 can be attributed to the charge transfer between PbS QDs since it is very similar to τ_2. The short decay time τ_3 may represent the lifetime of electrons in PbS QDs before they transfer to neighbouring graphene film. It is notable that the transfer rate of electrons from PbS to graphene is slower than that of holes at the PbS QDs/graphene interface since $\tau_1 < \tau_3$. Therefore it is reasonable to conclude that PbS QDs have net negative charge under light illumination as shown in the inset of Figure 5.11.

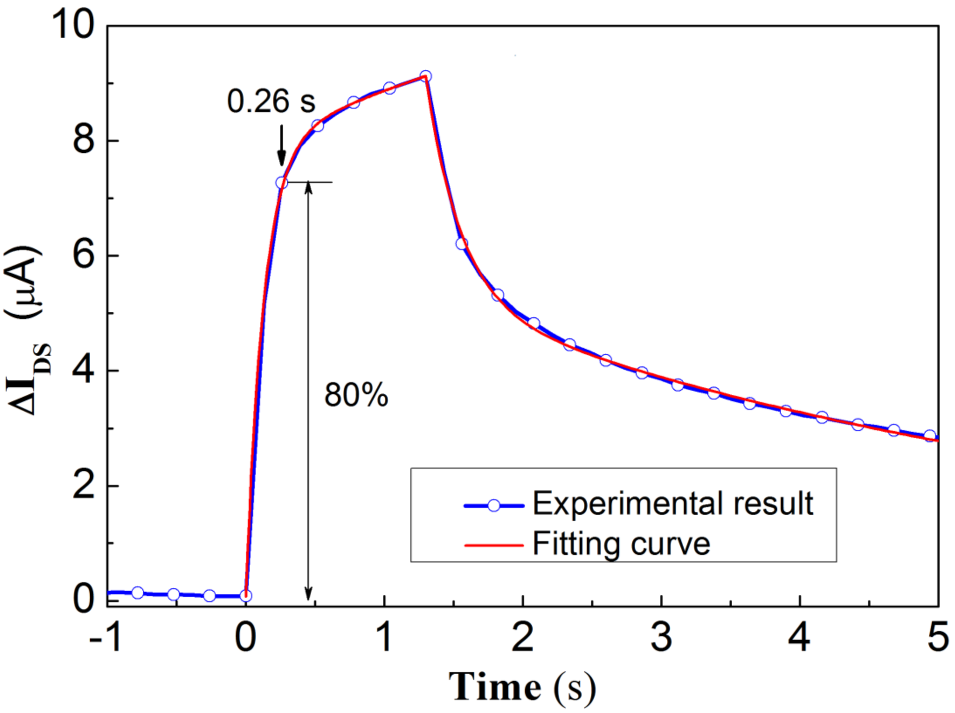

Figure 5.17 Current response of a graphene/PbS QDs photoconductor to on/off IR illumination. V_{DS} = 50mV; wavelength: 895 nm; Irradiance: 6.4mW/cm^2.

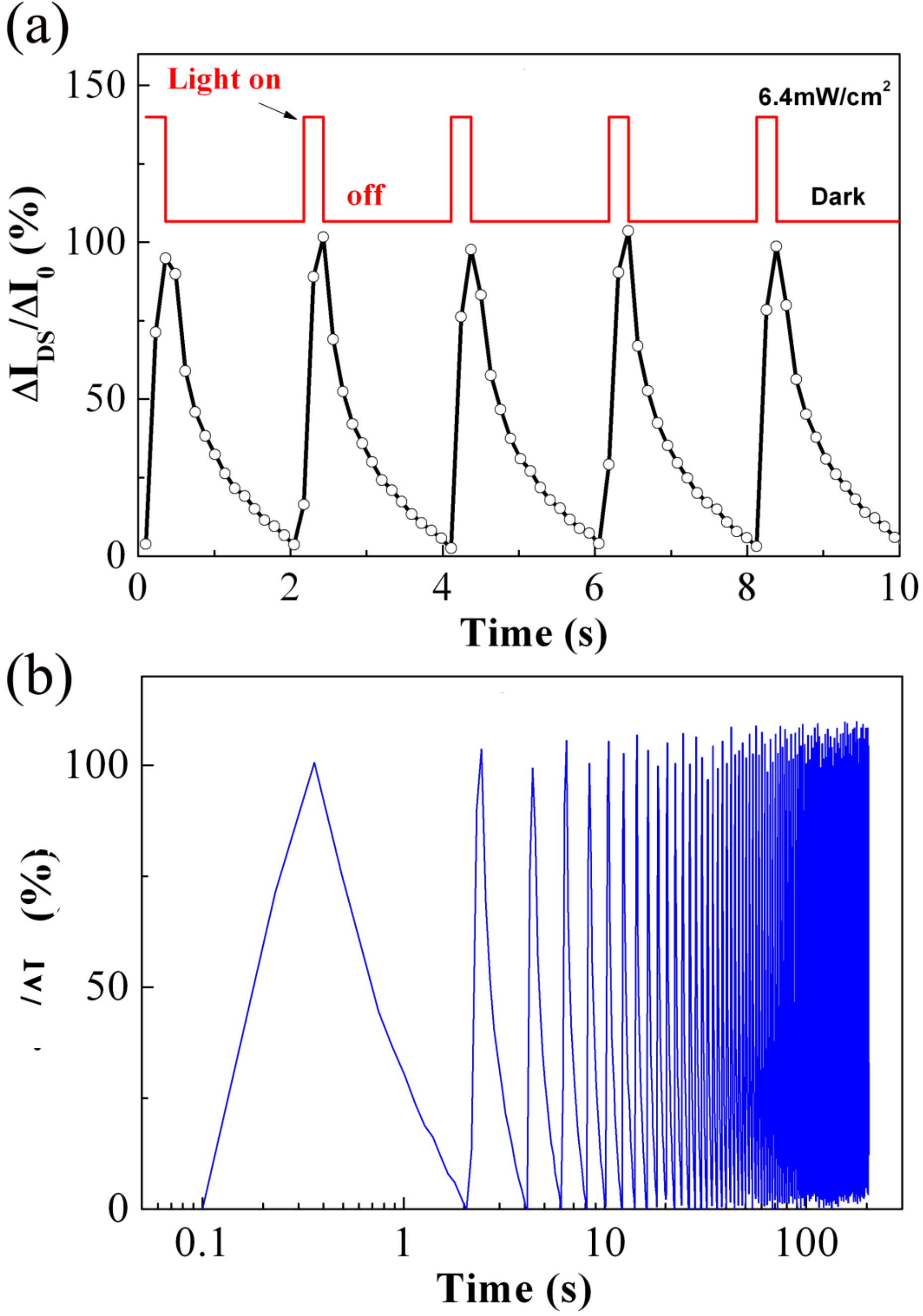

Figure 5.18 (b) and (c) Normalized current response to on/off IR light illumination for various cycles. On time: 0.3s; off time: 1.7s. ΔI_o is the average maximum current response.

Figure 5.18 show the channel current response of the device characterized under on/off light illumination. The response of the phototransistor is repeatable when the device is switched for more than one hundred times. The response of the phototransistor is much faster than the photoconductors based on graphene oxide reported before [215]. Since the response time is related to the transfer rate of electrons and holes from PbS QDs to graphene, the ligand capped on the PbS QDs is critical to the performance of the devices [52].

It is notable that the graphene/PbS QDs photoconductors can be easily fabricated on flexible substrates. CVD-grown single-layer graphene was transferred on a polyethylene terephthalate (PET) substrate and PbS QD film was then coated on the graphene layer by drop casting. Figure 5.19 shows the responsivity of a flexible PbS QDs/graphene photoconductor under different IR light intensity before and after a bending test for 1,000 times. We can find that no obvious degradation can be observed in the device after the bending test.

The responsivity of the device can be fitted very well with equation 4-2, where β=0.24. Since the devices can be easily patterned to small size, array of the highly sensitive IR sensors can be fabricated on flexible substrates for IR sensing or imaging, which may have promising applications in the future.

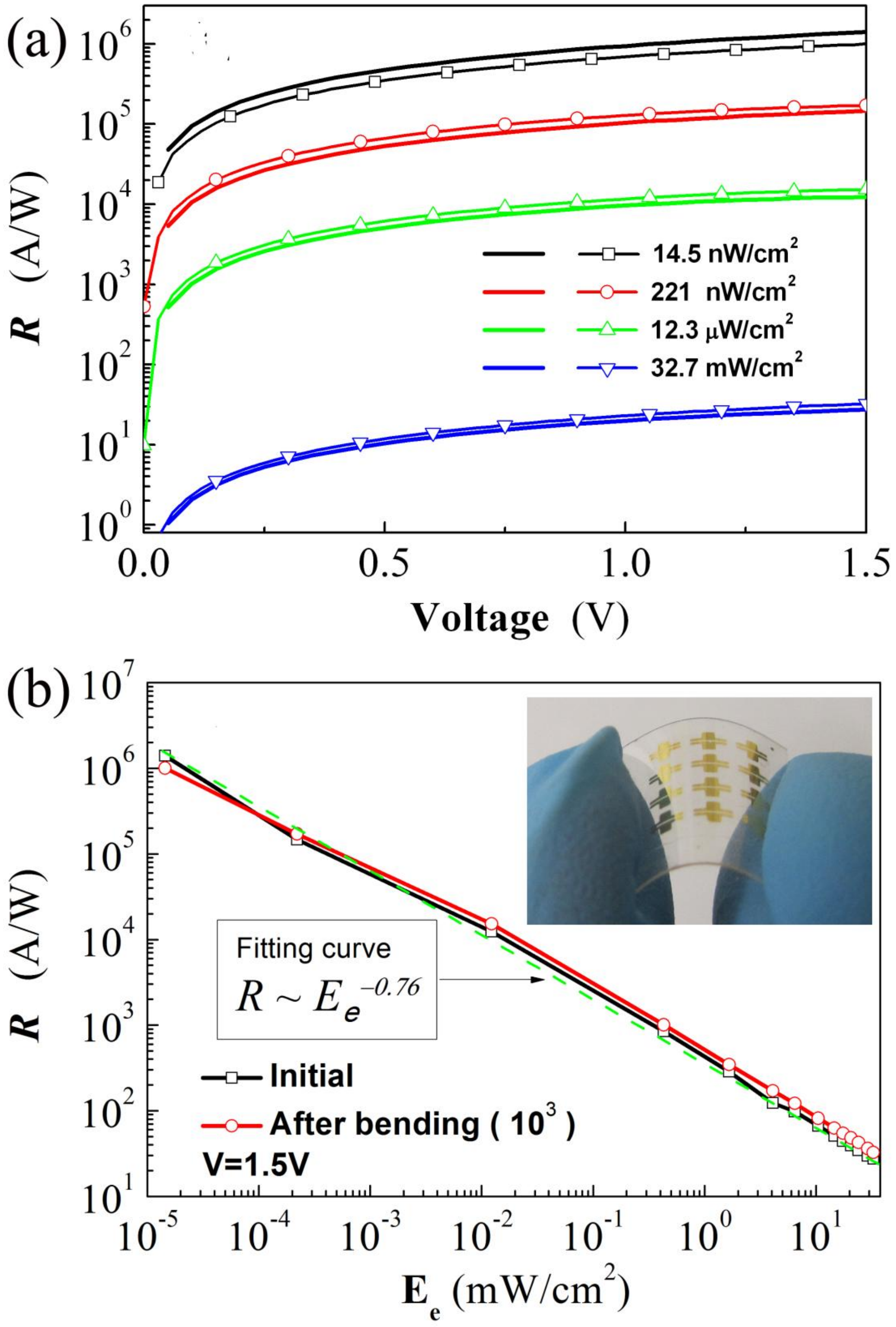

Figure 5.19 (a) Responsivity of a photoconductor based on PbS QDs and graphene fabricated on flexible PET substrate characterized before (solid lines) and after (dot lines) a bending test for 1,000 times. (b) Responsivity of the photoconductor as functions of light irradiance characterized before and after a bending test.

5.4 Summary

In summary, ultrasensitive NIR photodetectors based on CVD-grown graphene and PbS QDs were realized by facile solution process. The responsivities of the devices increase with the decrease of light irradiance/intensity and reach the value as high as 10^7A/W at low light irradiance, which is much higher than those of any photoconductors based on graphene or PbS QDs reported before. Moreover, the devices are fabricated on flexible plastic substrates and show excellent bending stability. The sensing mechanism of the grapheme/PbS QDs phtotoconductors is attributed to the charge transfer from PbS QDs to graphene under light illumination. Because of the different transfer rates of electron and hole from PbS QDs to graphene, net negative charges are accumulated in the PbS QDs under light illumination and result in field effect p-type doping in the graphene film. In addition, the capped ligand on the surface of PbS QDs is found to be critical to the photosensitive behavior of the devices, which will be a key issue to be optimized in further improving the device performance.

Chapter 6 Ultraviolet Driving Multilevel Memory Based on Graphene-TiO_2 Nanodots Hybrid Film

6.1 Introduction

In view of the important applications of memories in electronic products, huge efforts have been devoted to developing low cost, flexible and miniaturized new memory devices [17]. Recently, the application perspective of graphene in new memory device has attracted more and more attention because of its excellent properties such as scalability, flexibility, high carrier mobility and so on [45, 100, 122, 236-244] . Fragmentary Graphene or its derivative graphene oxide (GO) have been used in charge-storage capacitors which show large capacitance-voltage hysteresis [236, 237]. In addition, graphene have been integrated in Ferroelectric Field-Effect Transistor (FFET) as semiconductor layer. These FFETs making use of ferroelectric insulators show large transfer hysteresis that can be used for memory [100, 238, 239]. Some other interesting properties of graphene have also been demonstrated for their applications in memory devices, such as the conducting filament effect under electric field [240, 241], different spin state along graphene zigzag edge observed in equilibrium or with ballistic current [242]. Furthermore, graphene can interact with some other materials to emerge some synergetic effects that are reversible and can be used for memory devices. Very recently Wang et al showed the bistable states of graphene and low-work-function metal junction on modified substrate, which were attribute to the Fermi-level change of graphene induced by the carrier injections or ejections from metal electrode under bias [243]. Similar bistable states of graphene resistors were already reported by Echtermeyer et al. [244] and Zhuang et al [122], which were realized by electrochemical doping of graphene by water in ambient and conjugated polymer, respectively. The delicate properties and large surface area of graphene make it very sensitive to external stimuli. The hybrids based on graphene, especial the graphene-inorganic nanocrystal hybrids have been widely investigated for many promising applications [109]. However, to our best knowledge, no memory device has been reported making use of the graphene-quantum dots hybrid materials.

Multilevel memory devices have attracted increasing attention because of its extraordinary potential for high density storage [17]. Some groups have reported their multilevel memory devices with similar working principles of common binary memories, including the capacitive memory with ferroelectric dielectric that can be multilevel polarized [245], the resistive memories making use of the conductive filament [246, 247], charge trapping centre [248] or redox electrolyte [249] and the transistor memory based on ferroelectric materials [35, 250]. It is worth noting that the aforementioned devices are driven by electricity and can be categorized to three types: capacitor, transistor and resistor, which are the key elements of modern electronics [17].

Recently, Guo et al. reported phototransistors that show multilevel data storage ability. The threshold voltages of the devices can be changed by light-assisted gate voltage scanning and the changes can be stabilized because the photo-induced carriers in the semiconductor layer are trapped in an underlying polymer buffer layer [39]. Utilizing light to drive the nonvolatile memory has been realized in phase change memories used in CD/DVD blu-ray dishes before [98, 251]. Due to the Joule effect of laser, phase change materials are switched between crystalline and amorphous phases under light illumination, which show different conductive or reflective properties. The work of Guo et al expands a common phototransistor to be a multilevel memory device by introducing charge trap layer, which is a new concept that can be utilized in many other devices. In fact, several similar light-driving memory devices have been reported before. These devices make use of organic semiconductors as light harvesters and hybrid interface [41, 54], semiconductor itself [252] or nanocrystalline additives [42, 43] as charge trapping centers. The abundant light harvesting materials accommodate the promising future for light driving multilevel memory devices.

Nanocrystalline colloids have attracted significant attention in optoelectronic research, including solar cells and photodetectors, because of their solution processability and tunable bandgap originated from quantum size effect [16, 46]. In this chapter, we demonstrate a kind of ultraviolet light (UV) driving multilevel resistive memory based on graphene-TiO_2 nanocrystallites hybrid films. This kind of memory device shows multilevel conductive states under UV illumination. Different states can be programmed by adjusting UV irradiance and/or illumination time. These states can retain for long time in dark and can be erased by applying positive gate voltage. The working principle is as follows. The decorated TiO_2 nanocrystallites on graphene layer act as both the UV harvesters and hole trapping centers. The photon-induced electrons in TiO_2 nanocrystallites can inject into graphene film while holes are trapped in the TiO_2 nanocrystallites. The trapped holes can modulate the conductivity of the graphene film due to field effect doping. Surface ligand of the TiO_2 nanocrystallites was found to play a crucial role in trapping holes in TiO_2, which induces the memory effect. Positive gate voltage can elevate the Fermi level of graphene so as to promote electron injection to TiO_2 and erase the memory state.

6.2 Experimental

6.2.1 Materials

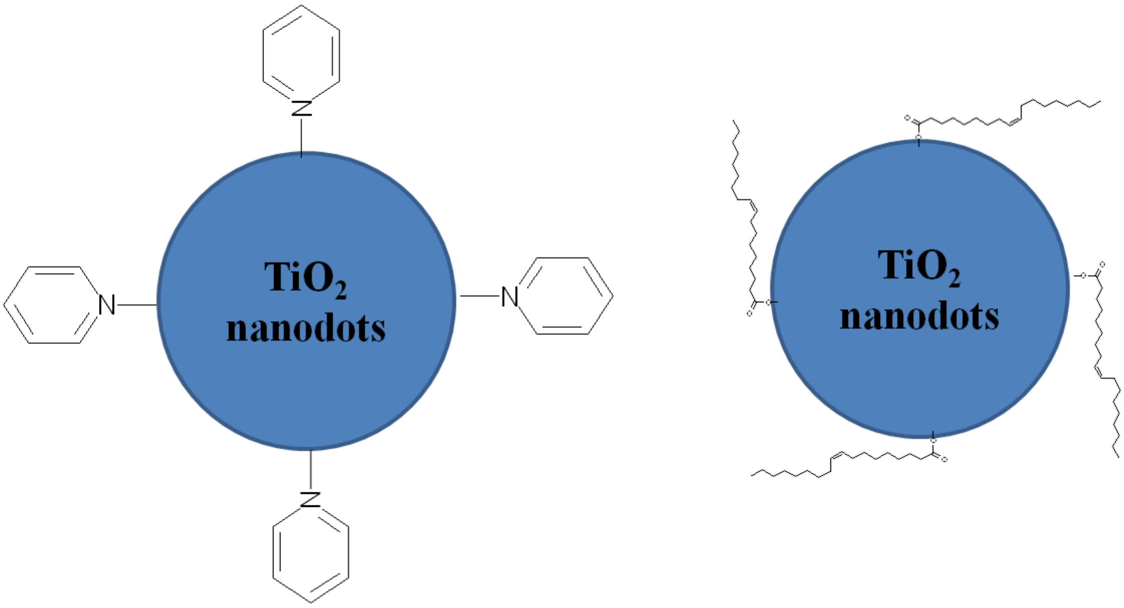

Figure 6.1 Schematics of 5nm TiO_2 nanodots capped with pyridine (left) and oleic acid ligand (right).

Single-layer graphene was prepared by chemical vapor deposition (CVD) method on copper foils and transferred on chosen substrates. TiO_2 nanodots capped with oleic acid ligand (average diameter = 5nm) were synthesized by nonhydrolytic method [207] and used in composite films. Some of this type TiO_2 nanodots were taken out to change their surface ligand from oleic acid to pyridine through the procedure described in the chapter 3.2. The TiO_2 nanodots capped with pyridine ligand were used in the memory devices. TiO_2 nanoparticles without surface modification, including rutile TiO_2 nanorod with a size of 5nm (diameter)×20nm (length) was purchased from Sigma-Aldrich and used in composite films for comparison. The schematic diagrams of TiO_2 nanoparticles with different surface ligand are shown in Figure 6.1.

6.2.2 Device Fabrications

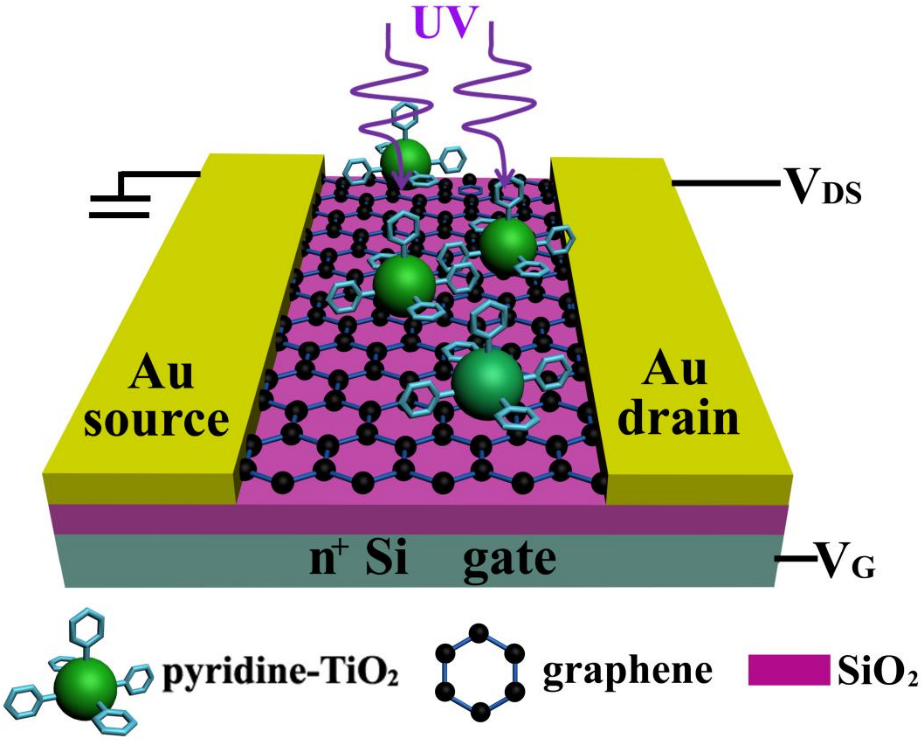

Figure 6.2 Schematic of device structure and measurement.

Single-layer graphene was transferred and patterned on the n^+Si/SiO_2 substrate with the typical technique that is described in the chapter 5.2.1. The thickness of SiO_2 is 300nm. Then gold electrodes were deposited on top of graphene by thermal evaporation through a shadow mask and formed a channel of W/L=2mm/0.1mm. Finally, the TiO_2 nanocrystallites capped with pyridine were coated on the graphene film by dropping their toluene colloid solution on the surface. The device was then dried for several hours in a glovebox filled with high purity N_2 before further measurement. The device structure is illustrated in Figure 6.2.

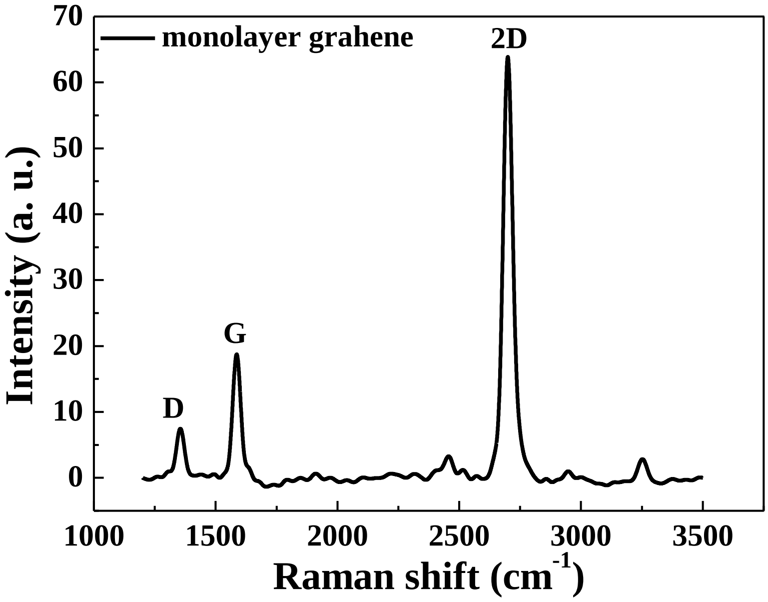

Figure 6.3 Raman spectrum of single-layer graphene on Si/SiO_2 substrate.

Roman spectrum: Raman spectroscopy (HORIBA, 488nm laser source) was used to confirm the monolayer property of graphene. The Raman spectrum of single layer graphene on Si/SiO_2 substrate is shown in Figure 6.3 [231].

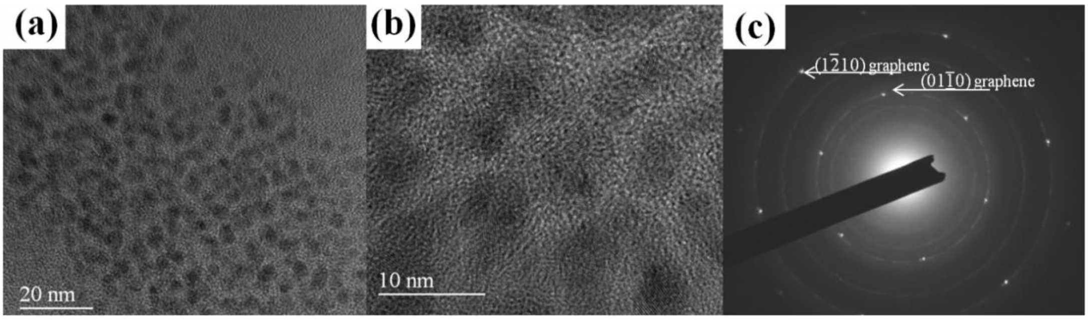

Figure 6.4 Transmission Electron Microscopy (TEM) images of the hybrid films.

Transmission Electron Microscopy (TEM): Figure 6.4a and b show the TEM (2100F, Japan) images of the TiO_2 on the surface of a graphene film. The electron diffraction patterns of graphene and TiO_2 nanocrystallites are shown in Figure 6.4c.

6.2.3 Measurement of Devices

The light driving memory was characterized by a semiconductor parameter analyzer (Agilent 4156C) under light illumination with different irradiance (as shown in Figure 6.2) in the glovebox filled with N_2. The light sources were monochromatic LED with the wavelength of 370nm and its light irradiance was controlled by a DC power source. To get stable results, light illumination at different irradiance was kept for 2 minutes before the measurement of transfer characteristics.

6.3 Performance of Devices

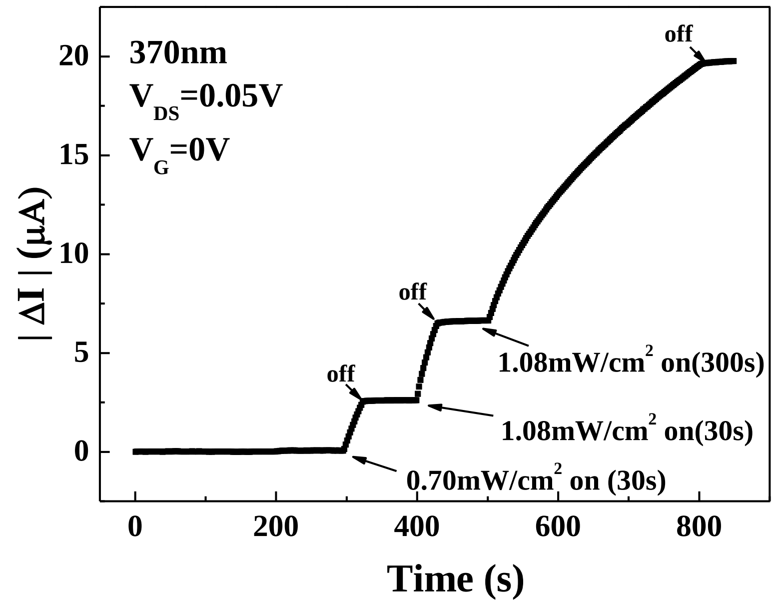

Figure 6.5 Current changes induced by UV illumination with different light irradiance or illumination time under programming condition.

As shown in Figure 6.2 , the device is a typical field-effect transistor with Si substrate as gate electrode and two Au patterns as source and drain electrodes. When the gate voltage (V_G) is 0 V, this device can be regarded as a photoresistor with two Au electrodes. Figure 6.5 shows the time dependent source-drain current (I_{DS}) under UV illumination. The drain-source voltage (V_{DS}) is 0.05V and V_G is 0V. This V_{DS} and V_G values will be called programming condition thereafter. It is notable that the current change increases with the increases of UV irradiance and illumination time. This is not difficult to be understood since TiO_2 can absorb light and generate net charges in TiO_2 that induce field-effect doping in the graphene film, which is similar to some phototransistors based on graphene-nanocrystallites hybrid films reported before [50, 155]. More important, our device shows very stable current after the removal of light, which means a good retention property. This is distinct to the normal photo-excitation and relaxation processes observed in optoelectronic devices reported before [47, 48, 215].

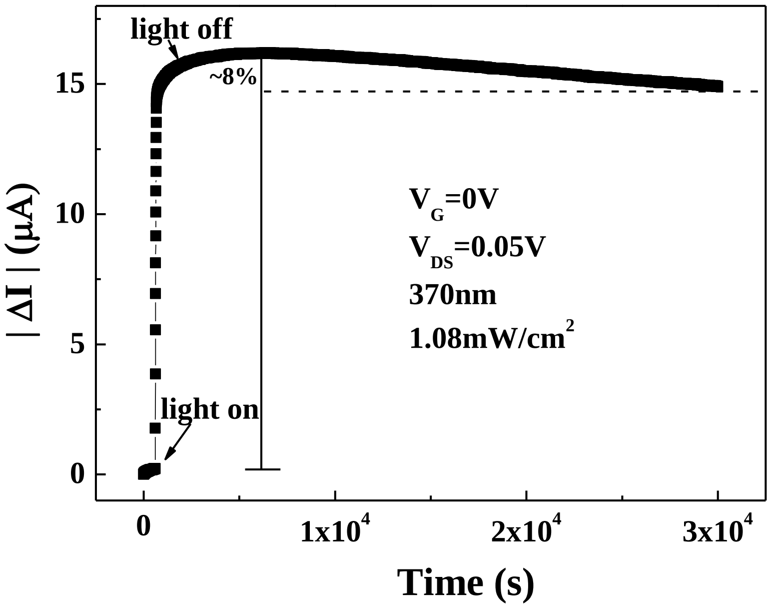

Figure 6.6 The retention of the channel current in dark after UV programming.

To further study the memory effect, long time retention test was carried out and the result is shown in Figure 6.6. The I_{DS} was measured under programming condition with UV illumination for ~100s. Then the light was removed and the measurement was carried on for about 10 hours. It is interesting to find that the current change had decayed only for ~8%. The photo-excitation states are so stable that the device has the potential to be used as a nonvolatile memory with UV illumination as the programming method [38, 42, 43, 54].

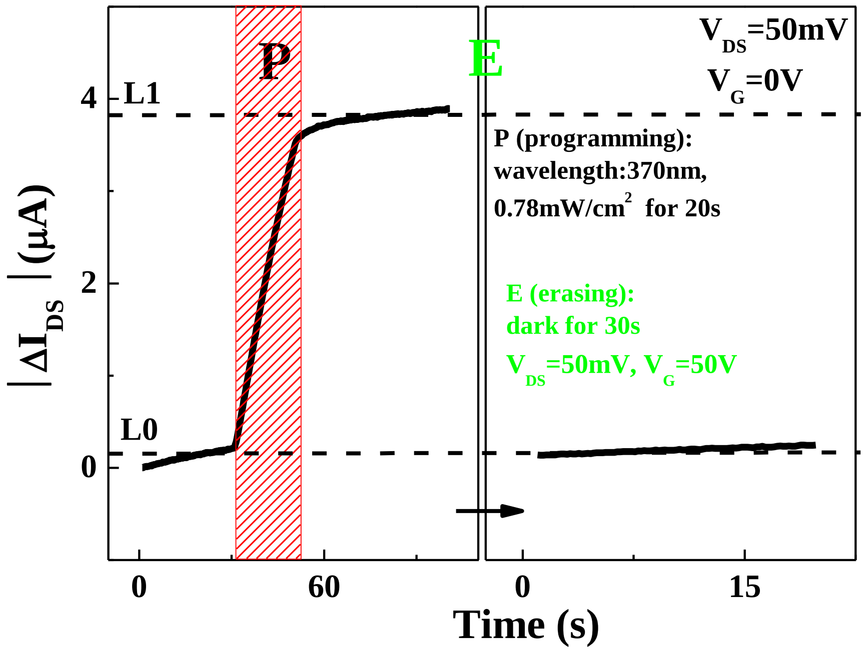

Figure 6.7 A programming-erasing process of a device.

As shown in Figure 6.7, the current change can be erased by applying positive V_G. The device was firstly illuminated by UV with light irradiance of 0.78mW/cm^2 for ~20s under programming condition. Then, light was removed and V_G was changed to 50V with constant V_{DS} for ~30s. It is found that the current change was erased totally. It is worth noting that the time consumed for erasing is dependent on V_G. Shorter erasing time is needed for larger V_G and vice verse. Therefore it provides the possibility to reset this memory shortly with a large positive V_G pulse.

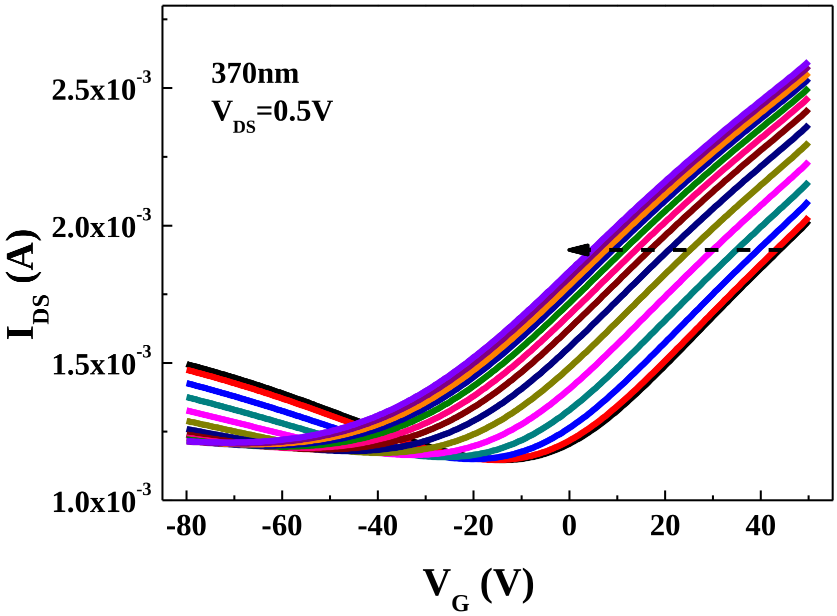

Figure 6.8 The shift of the transfer curves of the device under UV illumination. The arrow indicates the shift direction. From right to left, the UV irradiance are (mW/cm^2): 0; 0.35; 0.45; 0.52; 0.62; 0.70; 0.78; 0.85; 0.93; 0.97; 1.03; 1.08; 1.13; 1.16.

Similar light driving memories based on OTFT or carbon nanotube transistors have been reported by C. C chen et al. [43], J. Borghtti et al. [41], and S. Dutta et al. [54]. Although their devices show similar stable currents like ours, their photocurrents are erased by negative gate voltage. They attribute the programming-erasing processes of their devices to the following mechanism. Under illumination, photo-induced positive charge carriers are generated and injected into the conducting media while the negative charge carriers are trapped in the interfaces. So the negative gate voltage can repel these trapped negative charge carriers and promote their recombination. We consider that our memory can be attributed to the similar mechanism.

To better understand the mechanism of both programming and erasing of our device, field effect of this device was characterized. Figure 6.8 shows the transfer curves (I_{DS}~V_G) under UV illumination, wherein the curves shift to negative gate voltage horizontally with the increase of light irradiance. It is notable that hole mobility in graphene decreases slightly under light illumination.

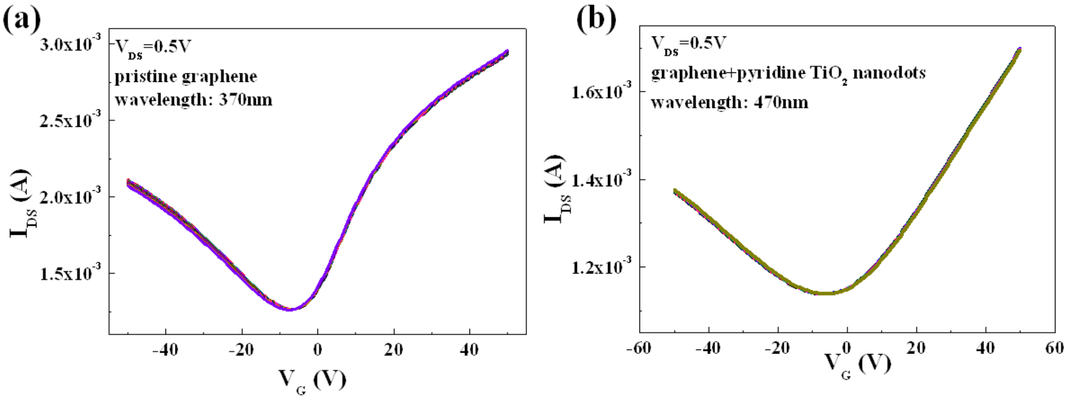

Figure 6.9 (a) Transfer curves of transistor based on pristine graphene under UV illumination (wavelength: 370nm) with different light irradiance. (b) Transfer curves of a graphene/TiO_2 hybrid transistor under visible light illumination (wavelength: 470nm) with different light irradiance.

Control transistor with only TiO_2 nanodots as active layer has been fabricated and measured, which show that the TiO_2-nanodot layer is almost insulating. Therefore the channel current can be attributed to graphene film solely. Theoretical calculations show that anatase TiO_2 nanocrystallites with a diameter of ~5nm will have the bandgap of ~3.2V corresponding to the UV wavelength of 385nm [253]. On the other hand, pure graphene shows poor optical absorption which is less than 5% at 370 nm and the absorption is even smaller at longer wavelength region [133]. Therefore it is reasonable to found that the device based on pure graphene is insensitive to UV, as shown in Figure 6.9a. Furthermore, graphene-TiO_2 hybrid transistor is not sensitive to the light illumination with the wavelength of 470nm, as shown in Figure 6.9b. Therefore, it can be concluded that graphene and TiO_2 nanocrystallites are responsible for conducting charge carriers and UV light harvesting, respectively.

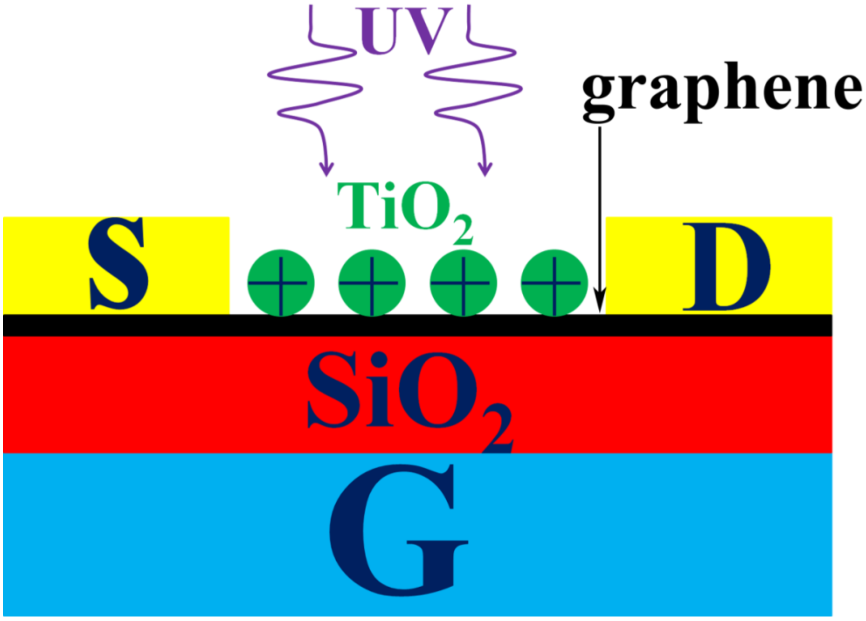

Figure 6.10 Mechanism of the UV response of the device. TiO_2 is positively charged under UV.

Apparently, the response of the transistor to light illumination is mainly due to the modulation of the effective gate voltage applied on it, which is similar to the phototransistors discussed in chapter 3 and 5 [47, 48]. Figure 6.10 demonstrates the mechanism of this process. TiO_2 nanocrystallites have the valence band level E_v of 7.5eV and the conduction band level E_c of 4.3eV [253]. The Fermi level of intrinsic graphene is about 4.6 eV at the Dirac point [231]. Therefore, when TiO_2 nanocrystallites are illuminated under UV light, electron/hole pairs (excitons) are generated and dissociate at the interface of TiO_2 and graphene. As the Fermi level of graphene is lower than the conducting band of TiO_2, electrons will inject into graphene, which will result in net positive charges in the nanocrystallites. In other words, more negative gate voltage is needed to obtain the charge neutrality point (Dirac point) in the graphene transistor and thus the conductivity of graphene film at V_G of 0V will increase. This charge transfer process is illustrated in Figure 6.11. At the same time, the injection of electrons into graphene will lead to the rise of Fermi level of graphene and thus increase the graphene-electrode potential barrier for hole injection. This is responsible for the aforementioned decrease of hole mobility [235].

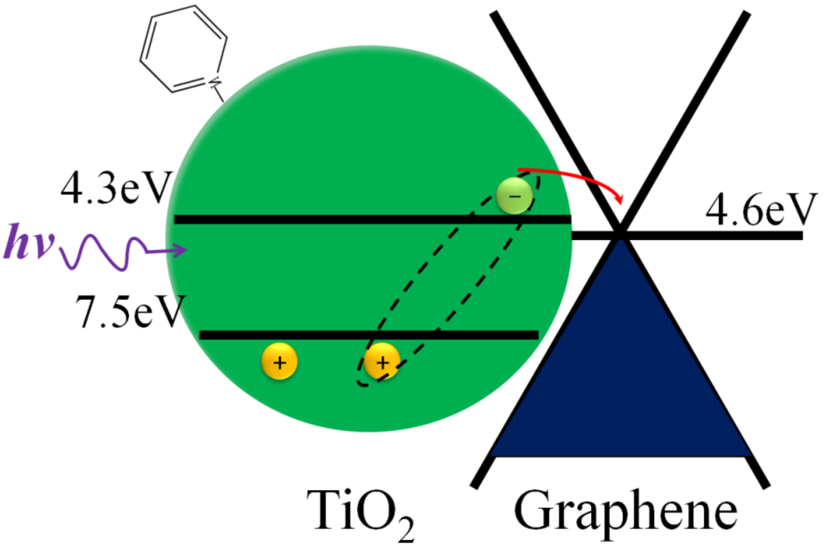

Figure 6.11 Schematic diagram of the proposed mechanisms of the programming.

In fact, the optoelectronic property of graphene-TiO_2 nanocrystallites hybrid system has already been studied for their applications in photodetectors [254], photocatalysts [255] and so on. The photon-induced carriers all recombine fast in those reports. Nevertheless, photo-excitation states in this report retain for pretty long time, which means excellent memory effect. To clarify the reasons, control devices with TiO_2 nanodots capped with oleic acid ligand or without any ligand were fabricated and characterized. Their retention behaviors are shown in Figure 6.12. These devices show similar photoresponse behaviors while the currents decay quickly. Therefore, the unique memory effect can be attributed to the suitable surface ligand (pyridine) of TiO_2.

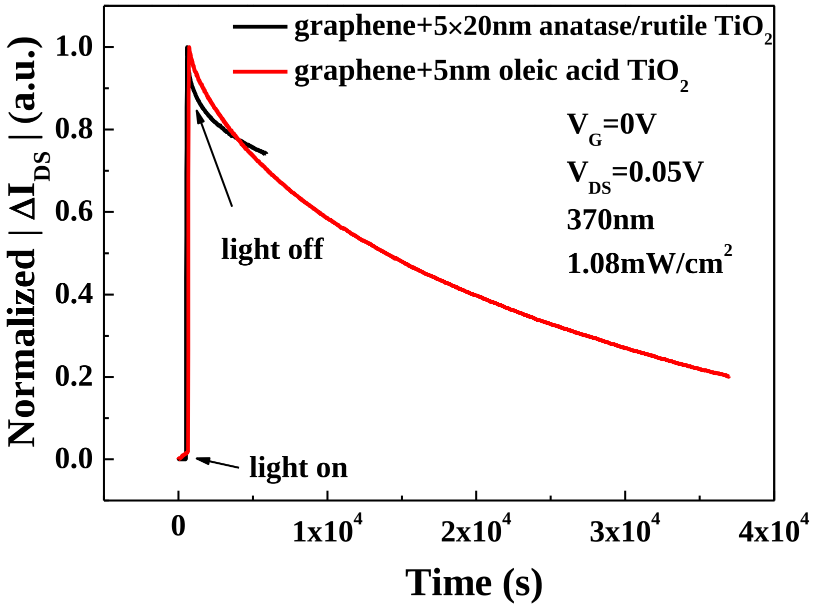

Figure 6.12 Current changes of control devices after UV illumination.

The mechanism of the erasing process of the memory device is speculated as follows and demonstrated in Figure 6.13. Under the stable photo-excitation states of a memory device, if a positive V_G is applied on the gate electrode, the Fermi level of graphene will increase to approach or exceed the conduction band of TiO_2. This will facilitate the injection of electrons from graphene to TiO_2 and promote the recombination of electrons and holes in TiO_2. The rate of this process will be dependent on the applied gate voltage V_G.

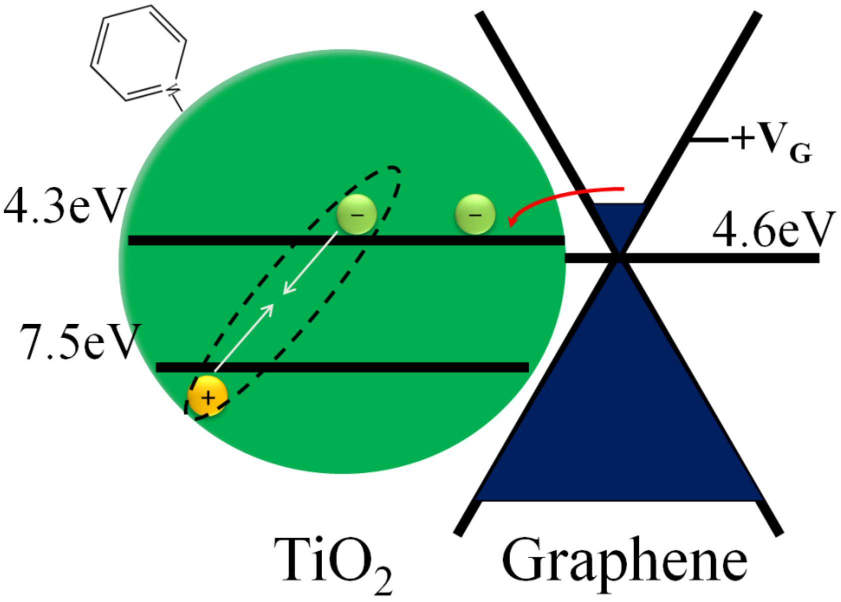

Figure 6.13 Illustration of the proposed mechanism of positive V_G induced erasing of a memory device. Fermi level of graphene is elevated by positive V_G so as to facilitate the hole-electron recombination in TiO_2.

What should be pointed out is that this work demonstrates a different photoresponse behavior to the work in chapter 5, which is the phototransistor based on graphene/PbS QDs. The origin of this difference is not clear yet and maybe related to the different energy band structures and interface properties of TiO_2 nanodots and PbS QDs. Further work is needed to clarify it.

The device exhibits excellent multilevel memory behavior. Figure 6.14a shows the current changes of the resistive memory (V_G=0V) under UV illumination for three times. The current changes are similar and device reaches a stable state after each illumination. This uniform programming can be repeated for more than ten times as shown in Figure 6.14b. Therefore, the multilevel memory can be realized by controlling light irradiance and/or illumination time. Figure 6.14c and d show the distinct current changes under different light irradiance and illumination time. This feature renders the device to have plenty of states for multilevel memory applications, which is highly controllable by UV illumination.

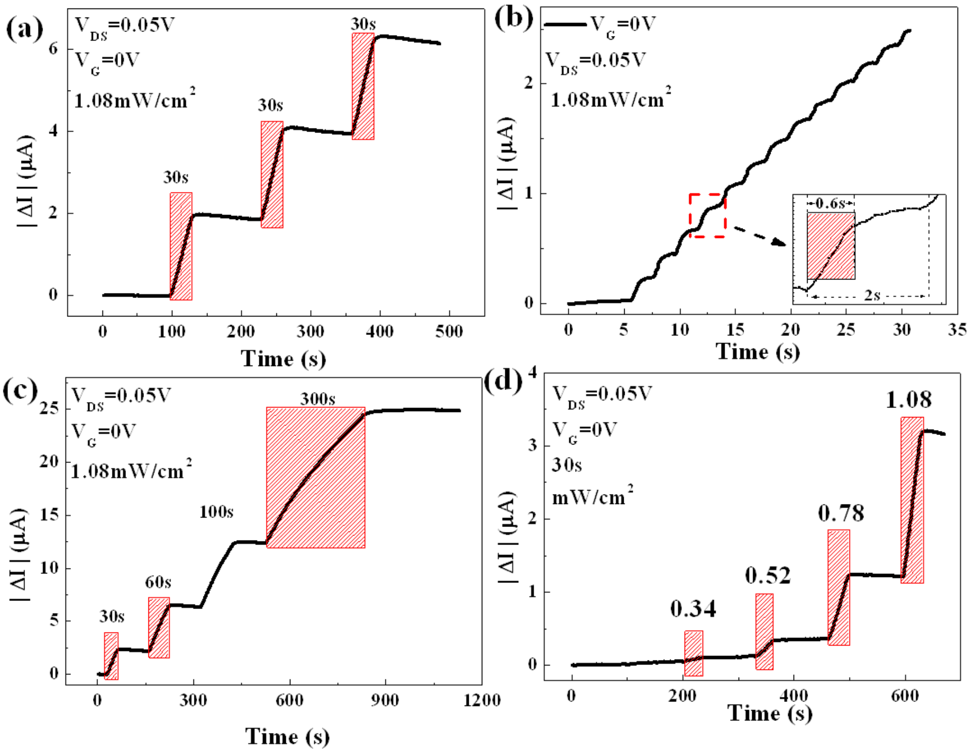

Figure 6.14 Various programming features of a memory. The programming light wavelength is 370nm. Red patterns represent the light illumination stages. (a) and (b) The repeatable programming of a device by UV with same irradiance and illumination time. (c) Different current change programmed by UV with constant irradiance and different illumination time. (d) Different current change programmed by UV with different irradiance and same illumination time

Figure 6.15 shows programming-erasing processes for three cycles. These levels are programmed by UV with different light irradiance or different illumination time. After each programming, positive V_G of 50V was applied to erase the current change to zero.

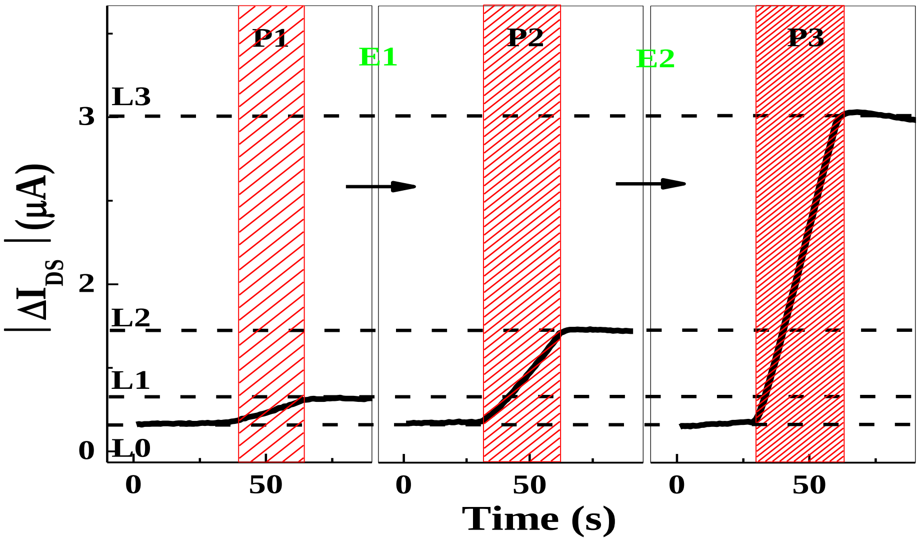

Figure 6.15 Multilevel programming and erasing process. “L”, “P” and “E” represent “level”, “programming” and “Erasing” respectively. Programming condition: V_G=0V, V_{DS}=0.05V. Erasing condition: V_G=50V, V_{DS}=0.05V. L1, L2 and L3 are programmed by UV (370nm) with irradiance (mW/cm^2)/illumination time (s) of 0.52 /30, 0.78 /30 and 1.08/30, respectively. Erasing time E1 and E2 are 12s and 60s, respectively.

6.4 Summary

In summary, we fabricated a novel nonvolatile, rewritable and multilevel resistive memory based on graphene-TiO_2 nanocrystallites hybrid film. This memory can be programmed by UV illumination. The current change in the hybrid film under the programming process shows multilevel characters and good retention for long time. Different current level of the hybrid film can be used to record different information and plenty of levels can be obtained by controlling UV irradiance and/or illumination time. The UV excitation of TiO_2 nanocrystallites is responsible to the photoresponse of the device. The surface pyridine ligand on TiO_2 nanocrystallites was found to be crucial to the stability of the excitation states. Positive gate voltage can be used to erase the programmed information by promoting the recombination of photo-induced carriers in TiO_2. This study paves a way to realizing multi-level memories driven by light.

Chapter 7 **Conclusion and Future Prospect**

7.1 **Conclusion**

In conclusion, huge effort has been devoted to the research of functional TFTs in view of their promising applications. Hybrid materials show many advantages when they are used in the TFTs because of the combination of the intrinsic properties of each component as well as the synergistic effects of them. It is notable that heterojunctions formed in the hybrid materials is critical to the optoelectronic performance of the devices. In this thesis, functional TFTs including phototransistors and light driving memories based on organic-inorganic and graphene-inorganic hybrid materials have been systemically studied.

P3HT/TiO_2 nanocrystallites hybrid films have been investigated. It is found that hole mobility of P3HT can be enhanced by the TiO_2 component. This enhancement can be attributed to the improved crystallinity of P3HT and the optimized orientation of polymer chains in the composite films, which is derived from the self-assembling effect induced by the TiO_2 component. Through comparing effects of different kinds of TiO_2, we found that both the rod-like shape and surface pyridine ligand of the nanocrystallites are necessary for the enhancement of mobility. Ultraviolet phototransistors have been fabricated based on this kind of hybrid film. With the improved hole mobility of P3HT, the phototransistors show superior current response than the P3HT/TiO_2 hybrid devices reported before.

Two kinds of NIR phototransistor based on P3HT/PbS QDs or graphene/PbS QDs hybrid films are fabricated and characterized. These transistors show shifting transfer curves toward high gate voltage under NIR illumination with the wavelength of 895nm. The photoresponsivities of the devices based on P3HT/PbS QDs and graphene PbS QDs reach up to 2×10^4 A/W and 1×10^7 A/W, respectively, which is much higher than that of a NIR photoresistor based on PbS QDs only. The sensing mechanism is due to the photo-induced charge generated in PbS QDs, which may change the effective gate voltage applied on the transistor. The high responsivities of the devices can be attributed to the high carrier mobilities in organic semiconductors or graphene.

Light driving, multilevel, rewritable and nonvolatile resistive memories have been fabricated using graphene/TiO_2 nanodots hybrid films. This kind of memory can be programmed by ultraviolet light and erased by applying positive gate voltage. The programming of the memory is essentially a photo-excitation process, which lead to field-effect doping of the graphene film. This doping effect can modulate the conductance of graphene and retain for long time after the removal of light. Surface pyridine ligand of TiO_2 nanodots is critical to the retention behavior. Multilevel feature of the memory can be realized by controlling light irradiance and/or illumination time.

7.2 Future Prospect

Although functional TFTs with excellent performance have been realized in our lab, further work is needed to enable their practical applications. Some properties such as stability in atmosphere, reproducibility, response speed and endurance of the devices need to be further improved. More importantly, devices with new functions and better performance are expected to be realized by choosing more suitable materials or optimum device design, which will be the future work of this area.

References

[1] J.E. Lilienfeld, Device for controlling electric current, in, US, 1933.

[2] P.S. Peercy, The drive to miniaturization. Nature 406 (2000) 1023-1026.

[3] K. Kano, Semiconductor devices, Prentice-Hall, Inc, 1998.

[4] A.I. Kingon, J.P. Maria, S.K. Streiffer, Alternative dielectrics to silicon dioxide for memory and logic devices. Nature 406 (2000) 1032-1038.

[5] P.K. Weimer, The TFT - a New Thin-Film Transistor. Proceedings of the ire (1962) 1462-1469.

[6] T.P. Brody, The Thin-Film Transistor - a Late Flowering Bloom. Ieee T Electron Dev 31 (1984) 1614-1628.

[7] T.P. Brody, The birth and early childhood of active matrix — A personal memoir. Journal of the Society for Information Display 4 (1996) 113-127.

[8] R.A. Street, Thin-Film Transistors. Adv Mater 21 (2009) 2007-2022.

[9] M.C. Hamilton, S. Martin, J. Kanicki, Thin-film organic polymer phototransistors. Ieee T Electron Dev 51 (2004) 877-885.

[10] A. Rogalski, J. Antoszewski, L. Faraone, Third-generation infrared photodetector arrays. J Appl Phys 105 (2009) 091101.

[11] R.C.G. Naber, K. Asadi, P.W.M. Blom, D.M. de Leeuw, B. de Boer, Organic Nonvolatile Memory Devices Based on Ferroelectricity. Adv Mater 22 (2010) 933-945.

[12] P. Lin, F. Yan, Organic Thin-Film Transistors for Chemical and Biological Sensing. Adv Mater 24 (2012) 34-51.

[13] J. Zaumseil, H. Sirringhaus, Electron and ambipolar transport in organic field-effect transistors. Chem Rev 107 (2007) 1296-1323.

[14] F. Cicoira, C. Santato, Organic light emitting field effect transistors: Advances and perspectives. Adv Funct Mater 17 (2007) 3421-3434.

[15] Y.L. Guo, G. Yu, Y.Q. Liu, Functional Organic Field-Effect Transistors. Adv Mater 22 (2010) 4427-4447.

[16] G. Konstantatos, E.H. Sargent, Solution-Processed Quantum Dot Photodetectors. P Ieee 97 (2009) 1666-1683.

[17] J.C. Scott, L.D. Bozano, Nonvolatile memory elements based on organic materials. Adv Mater 19 (2007) 1452-1463.

[18] M.C. Lemme, F.H.L. Koppens, A.L. Falk, M.S. Rudner, H. Park, L.S. Levitov, C.M. Marcus, Gate-Activated Photoresponse in a Graphene p-n Junction. Nano Lett 11 (2011) 4134-4137.

[19] S. Jeon, S.E. Ahn, I. Song, C.J. Kim, U.I. Chung, E. Lee, I. Yoo, A. Nathan, S. Lee, J. Robertson, K. Kim, Gated three-terminal device architecture to eliminate persistent photoconductivity in oxide semiconductor photosensor arrays. Nat Mater 11 (2012) 301-305.

[20] S.J. Kim, J.S. Lee, Flexible Organic Transistor Memory Devices. Nano Lett 10 (2010) 2884-2890.

[21] C.R. Kagan, P. Andry, Thin-film transistors, Marcel Dekker, Inc, 2003.

[22] G. Horowitz, Organic field-effect transistors. Adv Mater 10 (1998) 365-377.

[23] R.P. Ortiz, A. Facchetti, T.J. Marks, High-k Organic, Inorganic, and Hybrid Dielectrics for Low-Voltage Organic Field-Effect Transistors. Chem Rev 110 (2010) 205-239.

[24] L. Liao, Y.C. Lin, M.Q. Bao, R. Cheng, J.W. Bai, Y.A. Liu, Y.Q. Qu, K.L. Wang, Y. Huang, X.F. Duan, High-speed graphene transistors with a self-aligned nanowire gate. Nature 467 (2010) 305-308.

[25] Y.M. Lin, C. Dimitrakopoulos, K.A. Jenkins, D.B. Farmer, H.Y. Chiu, A. Grill, P. Avouris, 100-GHz Transistors from Wafer-Scale Epitaxial Graphene. Science 327 (2010) 662-662.

[26] D.B. Mitzi, Thin-film deposition of organic-inorganic hybrid materials. Chem Mater 13 (2001) 3283-3298.

[27] C. Sanchez, P. Belleville, M. Popall, L. Nicole, Applications of advanced hybrid organic-inorganic nanomaterials: from laboratory to market. Chem Soc Rev 40 (2011) 696-753.

[28] P.G. Romero, C. Sanchez, Functional hybrid materials, Wiley-Vch, 2004.

[29] C. Sanchez, B. Julian, P. Belleville, M. Popall, Applications of hybrid organic-inorganic nanocomposites. J Mater Chem 15 (2005) 3559-3592.

[30] B. Lebeau, P. Innocenzi, Hybrid materials for optics and photonics. Chem Soc Rev 40 (2011) 886-906.

[31] H. Sirringhaus, N. Tessler, R.H. Friend, Integrated optoelectronic devices based on conjugated polymers. Science 280 (1998) 1741-1744.

[32] G. Konstantatos, E.H. Sargent, Nanostructured materials for photon detection. Nat Nano 5 (2010) 391-400.

[33] Y. Zhou, S.T. Han, Z.X. Xu, V.A.L. Roy, Controlled Ambipolar Charge Transport Through a Self-Assembled Gold Nanoparticle Monolayer. Adv Mater 24 (2012) 1247-1251.

[34] X.B. Lu, J.Y. Dai, Memory effects of carbon nanotubes as charge storage nodes for floating gate memory applications. Appl Phys Lett 88 (2006) 2179374.

[35] J.I. Sohn, S.S. Choi, S.M. Morris, J.S. Bendall, H.J. Coles, W.K. Hong, G. Jo, T. Lee, M.E. Welland, Novel Nonvolatile Memory with Multibit Storage Based on a ZnO Nanowire Transistor. Nano Lett 10 (2010) 4316-4320.

[36] P.C. Wu, Y. Dai, Y. Ye, X.L. Fang, T. Sun, C. Liu, L. Dai, High-performance non-volatile CdS nanobelt-based floating nanodot gate memory. J Mater Chem 20 (2010) 4404-4408.

[37] Q.S. Wei, Y. Lin, E.R. Anderson, A.L. Briseno, S.P. Gido, J.J. Watkins, Additive-Driven Assembly of Block Copolymer-Nanoparticle Hybrid Materials for Solution Processable Floating Gate Memory. Acs Nano 6 (2012) 1188-1194.

[38] A. Star, Y. Lu, K. Bradley, G. Gruner, Nanotube optoelectronic memory devices. Nano Lett 4 (2004) 1587-1591.

[39] Y.L. Guo, C.A. Di, S.H. Ye, X.N. Sun, J. Zheng, Y.G. Wen, W.P. Wu, G. Yu, Y.Q. Liu, Multibit Storage of Organic Thin-Film Field-Effect Transistors. Adv Mater 21 (2009) 1954-1959.

[40] J.P. Bourgoin, J. Borghetti, P. Chenevier, V. Derycke, A. Filorarno, L. Goux, M.F. Goffinan, S. Lyonnais, K. Nguyen, G. Robert, S. Streiff, J.M. Bethoux, H. Happy, G. Dambrine, S. Lenfant, D. Vuillaume, Directed assembly for carbon nanotube device fabrication. Int El Devices Meet (2006) 164-167.

[41] J. Borghetti, V. Derycke, S. Lenfant, P. Chenevier, A. Filoramo, M. Goffman, D. Vuillaume, J.P. Bourgoin, Optoelectronic switch and memory devices based on polymer-functionalized carbon nanotube transistors. Adv Mater 18 (2006) 2535-2540.

[42] M.Y. Chiu, C.C. Chen, J.T. Sheu, K.H. Wei, An optical programming/electrical erasing memory device: Organic thin film transistors incorporating core/shell CdSe@ZnSe quantum dots and poly(3-hexylthiophene). Org Electron 10 (2009) 769-774.

[43] C.C. Chen, M.Y. Chiu, J.T. Sheu, K.H. Wei, Photoresponses and memory effects in organic thin film transistors incorporating poly(3-hexylthiophene)/CdSe quantum dots. Appl Phys Lett 92 (2008) 2899997.

[44] H. Shirakawa, E.J. Louis, A.G. Macdiarmid, C.K. Chiang, A.J. Heeger, Synthesis of Electrically Conducting Organic Polymers - Halogen Derivatives

of Polyacetylene, (Ch)X. J Chem Soc Chem Comm (1977) 578-580.

[45] A.K. Geim, K.S. Novoselov, The rise of graphene. Nat Mater 6 (2007) 183-191.

[46] P.V. Kamat, Quantum Dot Solar Cells. Semiconductor Nanocrystals as Light Harvesters. J Phys Chem C 112 (2008) 18737-18753.

[47] F. Yan, J.H. Li, S.M. Mok, Highly photosensitive thin film transistors based on a composite of poly(3-hexylthiophene) and titania nanoparticles. J Appl Phys 106 (2009) 3225760.

[48] S.M. Mok, F. Yan, H.L.W. Chan, Organic phototransistor based on poly(3-hexylthiophene)/TiO_2 nanoparticle composite. Appl Phys Lett 93 (2008) 023310.

[49] F.N. Xia, T. Mueller, Y.M. Lin, A. Valdes-Garcia, P. Avouris, Ultrafast graphene photodetector. Nat Nanotechnol 4 (2009) 839-843.

[50] D. Zhang, Gan, L., Cao, Y., Wang, Q., Qi, L. and Guo, X, Understanding Charge Transfer at PbS-Decorated Graphene Surfaces toward a Tunable Photosensor. Adv Mater 24 (2012) 2715–2720.

[51] G. Konstantatos, M. Badioli, L. Gaudreau, J. Osmond, M. Bernechea, F.P.G. de Arquer, F. Gatti, F.H.L. Koppens, Hybrid graphene-quantum dot phototransistors with ultrahigh gain. Nat Nano 7(2012) 363-368.

[52] G. Konstantatos, I. Howard, A. Fischer, S. Hoogland, J. Clifford, E. Klem, L. Levina, E.H. Sargent, Ultrasensitive solution-cast quantum dot photodetectors.

Nature 442 (2006) 180-183.

[53] V. Ryzhii, The theory of quantum-dot infrared phototransistors. Semicond Sci Tech 11 (1996) 759-765.

[54] S. Dutta, K.S. Narayan, Gate-voltage control of optically-induced charges and memory effects in polymer field-effect transistors. Adv Mater 16 (2004) 2151-2155.

[55] Y.S. Kim, S.Y. Bae, K.H. Kim, T.W. Lee, J.A. Hur, M.H. Hoang, M.J. Cho, S.J. Kim, Y. Kim, M. Kim, K. Lee, S.J. Lee, D.H. Choi, Highly sensitive phototransistor with crystalline microribbons from new pi-extended pyrene derivative via solution-phase self-assembly. Chem Commun 47 (2011) 8907-8909.

[56] A. Urich, K. Unterrainer, T. Mueller, Intrinsic Response Time of Graphene Photodetectors. Nano Lett 11 (2011) 2804-2808.

[57] M. Debucquoy, S. Verlaak, S. Steudel, K. Myny, J. Genoe, P. Heremans, Correlation between bias stress instability and phototransistor operation of pentacene thin-film transistors. Appl Phys Lett 91 (2007) 2777177.

[58] Y.L. Guo, C.Y. Du, G. Yu, C.A. Di, S.D. Jiang, H.X. Xi, J. Zheng, S.K. Yan, C.L. Yu, W.P. Hu, Y.Q. Liu, High-Performance Phototransistors Based on Organic Microribbons Prepared by a Solution Self-Assembly Process. Adv Funct Mater 20 (2010) 1019-1024.

[59] Y.Y. Noh, D.Y. Kim, Y. Yoshida, K. Yase, B.J. Jung, E. Lim, H.K. Shim,

High-photosensitivity p-channel organic phototransistors based on a biphenyl end-capped fused bithiophene oligomer. Appl Phys Lett 86 (2005) 1856144.

[60] G. Scarpa, E. Martin, S. Locci, B. Fabel, P. Lugli, Organic thin-film phototransistors based on poly(3-hexylthiophene). J Phys Conf Ser 193 (2009) 012114.

[61] T.P.I. Saragi, R. Pudzich, T. Fuhrmann, J. Salbeck, Organic phototransistor based on intramolecular charge transfer in a bifunctional spiro compound. Appl Phys Lett 84 (2004) 2334-2336.

[62] Y.Y. Noh, J. Ghim, S.J. Kang, K.J. Baeg, D.Y. Kim, K. Yase, Effect of light irradiation on the characteristics of organic field-effect transistors. J Appl Phys 100 (2006) 2364449.

[63] Y.R. Liu, J.B. Peng, P. Lai, Photo-response of polymer thin-film transistors based on poly(2-methoxy-5-(2'-ethyl-hexyloxy)-1,4-phenylene vinylene). Thin Solid Films 516 (2008) 4295-4300.

[64] D.Y. Tu, S. Pagliara, R. Cingolani, D. Pisignano, An electrospun fiber phototransistor by the conjugated polymer poly[2-methoxy-5-(2 '-ethylhexyloxy)-1,4-phenylene-vinylene]. Appl Phys Lett 98 (2011) 3534803.

[65] H.L. Dong, Z.S. Bo, W.P. Hu, High Performance Phototransistors of a Planar Conjugated Copolymer. Macromol Rapid Comm 32 (2011) 649-653.

[66] K.H. Kim, S.Y. Bae, Y.S. Kim, J.A. Hur, M.H. Hoang, T.W. Lee, M.J. Cho, Y. Kim, M. Kim, J.I. Jin, S.J. Kim, K. Lee, S.J. Lee, D.H. Choi, Highly

Photosensitive J-Aggregated Single-Crystalline Organic Transistors. Adv Mater 23 (2011) 3095-3099.

[67] Y. Cao, S. Liu, Q. Shen, K. Yan, P.J. Li, J. Xu, D.P. Yu, M.L. Steigerwald, C. Nuckolls, Z.F. Liu, X.F. Guo, High-Performance Photoresponsive Organic Nanotransistors with Single-Layer Graphenes as Two-Dimensional Electrodes. Adv Funct Mater 19 (2009) 2743-2748.

[68] M.J. Deen, M.H. Kazemeini, Photosensitive polymer thin-film FETs based on poly(3-octylthiophene). P Ieee 93 (2005) 1312-1320.

[69] K.S. Narayan, N. Kumar, Light responsive polymer field-effect transistor. Appl Phys Lett 79 (2001) 1891-1893.

[70] T. Pal, M. Arif, S.I. Khondaker, High performance organic phototransistor based on regioregular poly(3-hexylthiophene). Nanotechnology 21 (2010) 325201.

[71] Y.F. Xu, P.R. Berger, J.N. Wilson, U.H.F. Bunz, Photoresponsivity of polymer thin-film transistors based on polyphenyleneethynylene derivative with improved hole injection. Appl Phys Lett 85 (2004) 4219-4221.

[72] J.M. Choi, J. Lee, D.K. Hwang, J.H. Kim, S. Im, E. Kim, Comparative study of the photoresponse from tetracene-based and pentacene-based thin-film transistors. Appl Phys Lett 88 (2006) 2168493.

[73] B. Park, P. Paoprasert, I. In, J. Zwickey, P.E. Colavita, R.J. Hamers, P. Gopalan, P.G. Evans, Functional self-assembled monolayers for optimized

photoinduced charge transfer in organic field effect transistors. Adv Mater 19 (2007) 4353-4357.

[74] Y. Hu, G.F. Dong, C. Liu, L.D. Wang, Y. Qiu, Dependency of organic phototransistor properties on the dielectric layers. Appl Phys Lett 89 (2006) 2336722.

[75] V. Podzorov, M.E. Gershenson, Photoinduced charge transfer across the interface between organic molecular crystals and polymers. Phys Rev Lett 95 (2005) 016602.

[76] P.H. Wobkenberg, J.G. Labram, J.M. Swiecicki, K. Parkhomenko, D. Sredojevic, J.P. Gisselbrecht, D.M. de Leeuw, D.D.C. Bradley, J.P. Djukic, T.D. Anthopoulos, Ambipolar organic transistors and near-infrared phototransistors based on a solution-processable squarilium dye. J Mater Chem 20 (2010) 3673-3680.

[77] H.X. Chang, Z.H. Sun, Q.H. Yuan, F. Ding, X.M. Tao, F. Yan, Z.J. Zheng, Thin Film Field-Effect Phototransistors from Bandgap-Tunable, Solution-Processed, Few-Layer Reduced Graphene Oxide Films. Adv Mater 22 (2010) 4872-4876.

[78] M. Okada, K. Matsuura, J.P. Ao, Y. Ohno, H. Kawai, High-sensitivity UV phototransistor with GaN/AlGaN/GaN gate epi-structure. Phys Status Solidi A 204 (2007) 2117-2120.

[79] Z.Y. Yin, H. Li, H. Li, L. Jiang, Y.M. Shi, Y.H. Sun, G. Lu, Q. Zhang, X.D.

Chen, H. Zhang, Single-Layer MoS_2 Phototransistors. Acs Nano 6 (2012) 74-80.

[80] Y.M. Shi, W.J. Fang, K.K. Zhang, W.J. Zhang, L.J. Li, Photoelectrical Response in Single-Layer Graphene Transistors. Small 5 (2009) 2005-2011.

[81] N.M. Johnson, A. Chiang, Highly Photosensitive Transistors in Single-Crystal Silicon Thin-Films on Fused-Silica. Appl Phys Lett 45 (1984) 1102-1104.

[82] A. Zhang, H. Kim, J. Cheng, Y.H. Lo, Ultrahigh Responsivity Visible and Infrared Detection Using Silicon Nanowire Phototransistors. Nano Lett 10 (2010) 2117-2120.

[83] C.J. Kim, H.S. Lee, Y.J. Cho, K. Kang, M.H. Jo, Diameter-Dependent Internal Gain in Ohmic Ge Nanowire Photodetectors. Nano Lett 10 (2010) 2043-2048.

[84] V. Ryzhii, M. Ryzhii, Graphene bilayer field-effect phototransistor for terahertz and infrared detection. Phys Rev B 79 (2009) 245311.

[85] T. Mueller, F.N.A. Xia, P. Avouris, Graphene photodetectors for high-speed optical communications. Nat Photonics 4 (2010) 297-301.

[86] S. Liu, J.F. Ye, Y. Cao, Q. Shen, Z.F. Liu, L.M. Qi, X.F. Guo, Tunable Hybrid Photodetectors with Superhigh Responsivity. Small 5 (2009) 2371-2376.

[87] M.A. Loi, C. Rost-Bietsch, M. Murgia, S. Karg, W. Riess, M. Muccini, Tuning optoelectronic properties of ambipolar organic light-emitting transistors using a bulk-heterojunction approach. Adv Funct Mater 16 (2006) 41-47.

[88] Z.H. Sun, J.H. Li, C.M. Liu, S.H. Yang, F. Yan, Enhancement of Hole Mobility

of Poly(3-hexylthiophene) Induced by Titania Nanorods in Composite Films. Adv Mater 23 (2011) 3648-3652.

[89] T.D. Anthopoulos, Electro-optical circuits based on light-sensing ambipolar organic field-effect transistors. Appl Phys Lett 91 (2007) 2778754.

[90] N. Marjanovic, T.B. Singh, G. Dennler, S. Gunes, H. Neugebauer, N.S. Sariciftci, R. Schwodiauer, S. Bauer, Photoresponse of organic field-effect transistors based on conjugated polymer/fullerene blends. Org Electron 7 (2006) 188-194.

[91] Y.F. Li, T. Kaneko, J. Kong, R. Hatakeyama, Photoswitching in Azafullerene Encapsulated Single-Walled Carbon Nanotube FET Devices. J Am Chem Soc 131 (2009) 3412-3413.

[92] K.K. Manga, S. Wang, M. Jaiswal, Q.L. Bao, K.P. Loh, High-Gain Graphene-Titanium Oxide Photoconductor Made from Inkjet Printable Ionic Solution. Adv Mater 22 (2010) 5265-5270.

[93] H.W. Zan, W.T. Chen, H.W. Hsueh, S.C. Kao, M.C. Ku, C.C. Tsai, H.F. Meng, Amorphous indium-gallium-zinc-oxide visible-light phototransistor with a polymeric light absorption layer. Appl Phys Lett 97 (2010) 3517506.

[94] S. Nam, H. Hwang, H. Kim, Y. Kim, Effect of Gate Voltage in Organic Phototransistors Based on Polythiophene/Fullerene Bulk Heterojunction Nanolayers. Mol Cryst Liq Cryst 519 (2010) 260-265.

[95] H. Hwang, H. Kim, S. Nam, D.D.C. Bradley, C.S. Ha, Y. Kim, Organic

phototransistors with nanoscale phase-separated polymer/polymer bulk heterojunction layers. Nanoscale 3 (2011) 2275-2279.

[96] R.M. Meixner, H. Gobel, F.A. Yildirim, W. Bauhofer, W. Krautschneider, Wavelength-selective organic field-effect phototransistors based on dye-doped poly-3-hexylthiophene. Appl Phys Lett 89 (2006) 2344838.

[97] J.N. Shive, The Phototransistor in, Bell Laboratories RECORD, 1950.

[98] H.S.P. Wong, S. Raoux, S. Kim, J.L. Liang, J.P. Reifenberg, B. Rajendran, M. Asheghi, K.E. Goodson, Phase Change Memory. P Ieee 98 (2010) 2201-2227.

[99] B.N. Pal, P. Trottman, J. Sun, H.E. Katz, Solution-deposited zinc oxide and zinc oxide/pentacene bilayer transistors: High mobility n-channel, ambipolar and nonvolatile devices. Adv Funct Mater 18 (2008) 1832-1839.

[100] Y. Zheng, G.X. Ni, C.T. Toh, M.G. Zeng, S.T. Chen, K. Yao, B. Ozyilmaz, Gate-controlled nonvolatile graphene-ferroelectric memory. Appl Phys Lett 94 (2009) 3119215.

[101] B. Pradhan, S.K. Batabyal, A.J. Pal, Electrical bistability and memory phenomenon in carbon nanotube-conjugated polymer matrixes. J Phys Chem B 110 (2006) 8274-8277.

[102] P. Gomez-Romero, Hybrid organic-inorganic materials - In search of synergic activity. Adv Mater 13 (2001) 163-174.

[103] W.R. Wu, U.S. Jeng, C.J. Su, K.H. Wei, M.S. Su, M.Y. Chiu, C.Y. Chen, W.B. Su, C.H. Su, A.C. Su, Competition between Fullerene Aggregation and

Poly(3-hexylthiophene) Crystallization upon Annealing of Bulk Heterojunction Solar Cells. Acs Nano 5 (2011) 6233-6243.

[104] J. Soeda, Y. Hirose, M. Yamagishi, A. Nakao, T. Uemura, K. Nakayama, M. Uno, Y. Nakazawa, K. Takimiya, J. Takeya, Solution-Crystallized Organic Field-Effect Transistors with Charge-Acceptor Layers: High-Mobility and Low-Threshold-Voltage Operation in Air. Adv Mater 23 (2011) 3309-3314.

[105] R. Hamilton, J. Smith, S. Ogier, M. Heeney, J.E. Anthony, I. McCulloch, J. Veres, D.D.C. Bradley, T.D. Anthopoulos, High-Performance Polymer-Small Molecule Blend Organic Transistors. Adv Mater 21 (2009) 1166-1171.

[106] M. Shkunov, R. Simms, M. Heeney, S. Tierney, I. McCulloch, Ambipolar field-effect transistors based on solution-processable blends of thieno[2,3-b]thiophene terthiophene polymer and methanofullerenes. Adv Mater 17 (2005) 2608-2612.

[107] H.M. Cheong, D. Kim, M.C. Hanna, A. Mascarenhas, Effect of doping on photoluminescence upconversion in GaAs/$Al_xGa_{1-x}As$ heterostructures. Appl Phys Lett 81 (2002) 58-60.

[108] B. Das, B. Choudhury, A. Gomathi, A.K. Manna, S.K. Pati, C.N.R. Rao, Interaction of Inorganic Nanoparticles with Graphene. Chemphyschem 12 (2011) 937-943.

[109] S. Bai, X.P. Shen, Graphene-inorganic nanocomposites. Rsc Adv 2 (2012) 64-98.

[110] B. Arkles, MRS Bull 26 (2001) 402.

[111] C. Sanchez, M. In, Molecular design of alkoxide precursors for the synthesis of hybrid organic-inorganic gels. Journal of Non-Crystalline Solids 147 (1992) 1-12.

[112] P. Judeinstein, C. Sanchez, Hybrid organic-inorganic materials: a land of multidisciplinarity. J Mater Chem 6 (1996) 511-525.

[113] C.R. Kagan, D.B. Mitzi, C.D. Dimitrakopoulos, Organic-inorganic hybrid materials as semiconducting channels in thin-film field-effect transistors. Science 286 (1999) 945-947.

[114] Z.X. Xu, V.A.L. Roy, P. Stallinga, M. Muccini, S. Toffanin, H.F. Xiang, C.M. Che, Nanocomposite field effect transistors based on zinc oxide/polymer blends. Appl Phys Lett 90 (2007) 2740478.

[115] J. Halme, P. Vahermaa, K. Miettunen, P. Lund, Device Physics of Dye Solar Cells. Adv Mater 22 (2010) E210-E234.

[116] B. Oregan, M. Gratzel, A Low-Cost, High-Efficiency Solar-Cell Based on Dye-Sensitized Colloidal TiO_2 Films. Nature 353 (1991) 737-740.

[117] B.Q. Wang, B. Li, Q. Deng, S.J. Dong, Amperometric glucose biosensor based on sol-gel organic-inorganic hybrid material. Anal Chem 70 (1998) 3170-3174.

[118] A.C. Arango, S.A. Carter, P.J. Brock, Charge transfer in photovoltaics consisting of interpenetrating networks of conjugated polymer and TiO2

nanoparticles. Appl Phys Lett 74 (1999) 1698.

[119] H. Yoneyama, M. Tokuda, S. Kuwabata, Photoinduced Electrochromic Reactions of Deprotonated Polyaniline Containing Cadmium-Sulfide Particles. Electrochim Acta 39 (1994) 1315-1320.

[120] H. Yoneyama, A. Kishimoto, S. Kuwabata, Charge Discharge Properties of Polypyrrole Films Containing Manganese-Dioxide Particles. J Chem Soc Chem Comm (1991) 986-987.

[121] M. Lira-Cantu, P. Gomez-Romero, The organic-inorganic polyaniline/V2O5 system - Application as a high-capacity hybrid cathode for rechargeable lithium batteries. J Electrochem Soc 146 (1999) 2029-2033.

[122] X.D. Zhuang, Y. Chen, G. Liu, P.P. Li, C.X. Zhu, E.T. Kang, K.G. Neoh, B. Zhang, J.H. Zhu, Y.X. Li, Conjugated-Polymer-Functionalized Graphene Oxide: Synthesis and Nonvolatile Rewritable Memory Effect. Adv Mater 22 (2010) 1731-1735.

[123] S. Stankovich, D.A. Dikin, G.H.B. Dommett, K.M. Kohlhaas, E.J. Zimney, E.A. Stach, R.D. Piner, S.T. Nguyen, R.S. Ruoff, Graphene-based composite materials. Nature 442 (2006) 282-286.

[124] D.B. Mitzi, M.T. Prikas, K. Chondroudis, Thin film deposition of organic-inorganic hybrid materials using a single source thermal ablation technique. Chem Mater 11 (1999) 542-544.

[125] J. Park, S. Lee, H.H. Lee, High-mobility polymer thin-film transistors

fabricated by solvent-assisted drop-casting. Org Electron 7 (2006) 256-260.

[126] K.S. Novoselov, Nobel Lecture: Graphene: Materials in the Flatland. Rev Mod Phys 83 (2011) 837-849.

[127] K.S. Novoselov, A.K. Geim, S.V. Morozov, D. Jiang, Y. Zhang, S.V. Dubonos, I.V. Grigorieva, A.A. Firsov, Electric field effect in atomically thin carbon films. Science 306 (2004) 666-669.

[128] C.R. Dean, A.F. Young, I. Meric, C. Lee, L. Wang, S. Sorgenfrei, K. Watanabe, T. Taniguchi, P. Kim, K.L. Shepard, J. Hone, Boron nitride substrates for high-quality graphene electronics. Nat Nanotechnol 5 (2010) 722-726.

[129] K.I. Bolotin, K.J. Sikes, Z. Jiang, M. Klima, G. Fudenberg, J. Hone, P. Kim, H.L. Stormer, Ultrahigh electron mobility in suspended graphene. Solid State Commun 146 (2008) 351-355.

[130] E.V. Castro, H. Ochoa, M.I. Katsnelson, R.V. Gorbachev, D.C. Elias, K.S. Novoselov, A.K. Geim, F. Guinea, Limits on Charge Carrier Mobility in Suspended Graphene due to Flexural Phonons. Phys Rev Lett 105 (2010) 266601.

[131] Y.M. Lin, K.A. Jenkins, A. Valdes-Garcia, J.P. Small, D.B. Farmer, P. Avouris, Operation of Graphene Transistors at Gigahertz Frequencies. Nano Lett 9 (2009) 422-426.

[132] Z.K. Liu, J.H. Li, Z.H. Sun, G.A. Tai, S.P. Lau, F. Yan, The Application of

Highly Doped Single-Layer Graphene as the Top Electrodes of Semitransparent Organic Solar Cells. Acs Nano 6 (2012) 810-818.

[133] S. Bae, H. Kim, Y. Lee, X.F. Xu, J.S. Park, Y. Zheng, J. Balakrishnan, T. Lei, H.R. Kim, Y.I. Song, Y.J. Kim, K.S. Kim, B. Ozyilmaz, J.H. Ahn, B.H. Hong, S. Iijima, Roll-to-roll production of 30-inch graphene films for transparent electrodes. Nat Nanotechnol 5 (2010) 574-578.

[134] K.F. Mak, M.Y. Sfeir, Y. Wu, C.H. Lui, J.A. Misewich, T.F. Heinz, Measurement of the Optical Conductivity of Graphene. Phys Rev Lett 101 (2008) 196405.

[135] R.R. Nair, P. Blake, A.N. Grigorenko, K.S. Novoselov, T.J. Booth, T. Stauber, N.M.R. Peres, A.K. Geim, Fine structure constant defines visual transparency of graphene. Science 320 (2008) 1308-1308.

[136] A.B. Kuzmenko, E. van Heumen, F. Carbone, D. van der Marel, Universal optical conductance of graphite. Phys Rev Lett 100 (2008) 117401.

[137] Z.Q. Li, E.A. Henriksen, Z. Jiang, Z. Hao, M.C. Martin, P. Kim, H.L. Stormer, D.N. Basov, Dirac charge dynamics in graphene by infrared spectroscopy. Nat Phys 4 (2008) 532-535.

[138] V.G. Kravets, A.N. Grigorenko, R.R. Nair, P. Blake, S. Anissimova, K.S. Novoselov, A.K. Geim, Spectroscopic ellipsometry of graphene and an exciton-shifted van Hove peak in absorption. Phys Rev B 81 (2010) 155413.

[139] A.F. Young, P. Kim, Quantum interference and Klein tunnelling in graphene

heterojunctions. Nat Phys 5 (2009) 222-226.

[140] A. Kumar, C.W. Zhou, The Race To Replace Tin-Doped Indium Oxide: Which Material Will Win? Acs Nano 4 (2010) 11-14.

[141] C.W. Jeong, P. Nair, M. Khan, M. Lundstrom, M.A. Alam, Prospects for Nanowire-Doped Polycrystalline Graphene Films for Ultratransparent, Highly Conductive Electrodes. Nano Lett 11 (2011) 5020-5025.

[142] J.B. Wu, M. Agrawal, H.A. Becerril, Z.N. Bao, Z.F. Liu, Y.S. Chen, P. Peumans, Organic Light-Emitting Diodes on Solution-Processed Graphene Transparent Electrodes. Acs Nano 4 (2010) 43-48.

[143] C. Lee, X.D. Wei, J.W. Kysar, J. Hone, Measurement of the elastic properties and intrinsic strength of monolayer graphene. Science 321 (2008) 385-388.

[144] L. Gong, I.A. Kinloch, R.J. Young, I. Riaz, R. Jalil, K.S. Novoselov, Interfacial Stress Transfer in a Graphene Monolayer Nanocomposite. Adv Mater 22 (2010) 2694-2697.

[145] C. Gomez-Navarro, M. Burghard, K. Kern, Elastic properties of chemically derived single graphene sheets. Nano Lett 8 (2008) 2045-2049.

[146] A.A. Balandin, S. Ghosh, W.Z. Bao, I. Calizo, D. Teweldebrhan, F. Miao, C.N. Lau, Superior thermal conductivity of single-layer graphene. Nano Lett 8 (2008) 902-907.

[147] X. Huang, X.Y. Qi, F. Boey, H. Zhang, Graphene-based composites. Chem Soc Rev 41 (2012) 666-686.

[148] J.R. Potts, D.R. Dreyer, C.W. Bielawski, R.S. Ruoff, Graphene-based polymer nanocomposites. Polymer 52 (2011) 5-25.

[149] R. Verdejo, M.M. Bernal, L.J. Romasanta, M.A. Lopez-Manchado, Graphene filled polymer nanocomposites. J Mater Chem 21 (2011) 3301-3310.

[150] J. Huang, L.M. Zhang, B.A. Chen, N. Ji, F.H. Chen, Y. Zhang, Z.J. Zhang, Nanocomposites of size-controlled gold nanoparticles and graphene oxide: Formation and applications in SERS and catalysis. Nanoscale 2 (2010) 2733-2738.

[151] Y.X. Fang, S.J. Guo, C.Z. Zhu, Y.M. Zhai, E.K. Wang, Self-Assembly of Cationic Polyelectrolyte-Functionalized Graphene Nanosheets and Gold Nanoparticles: A Two-Dimensional Heterostructure for Hydrogen Peroxide Sensing. Langmuir 26 (2010) 11277-11282.

[152] Z.P. Li, J.Q. Wang, X.H. Liu, S. Liu, J.F. Ou, S.R. Yang, Electrostatic layer-by-layer self-assembly multilayer films based on graphene and manganese dioxide sheets as novel electrode materials for supercapacitors. J Mater Chem 21 (2011) 3397-3403.

[153] F.A. He, J.T. Fan, D. Ma, L.M. Zhang, C. Leung, H.L. Chan, The attachment of Fe_3O_4 nanoparticles to graphene oxide by covalent bonding. Carbon 48 (2010) 3139-3144.

[154] G.X. Zhu, Y.J. Liu, Z. Xu, T.A. Jiang, C. Zhang, X. Li, G. Qi, Flexible Magnetic Nanoparticles-Reduced Graphene Oxide Composite Membranes

Formed by Self-Assembly in Solution. Chemphyschem 11 (2010) 2432-2437.

[155] X.M. Geng, L. Niu, Z.Y. Xing, R.S. Song, G.T. Liu, M.T. Sun, G.S. Cheng, H.J. Zhong, Z.H. Liu, Z.J. Zhang, L.F. Sun, H.X. Xu, L. Lu, L.W. Liu, Aqueous-Processable Noncovalent Chemically Converted Graphene-Quantum Dot Composites for Flexible and Transparent Optoelectronic Films. Adv Mater 22 (2010) 638-642.

[156] X.R. Zhang, S.G. Li, X. Jin, S.S. Zhang, A new photoelectrochemical aptasensor for the detection of thrombin based on functionalized graphene and CdSe nanoparticles multilayers. Chem Commun 47 (2011) 4929-4931.

[157] H.Q. Zhou, C.Y. Qiu, Z. Liu, H.C. Yang, L.J. Hu, J. Liu, H.F. Yang, C.Z. Gu, L.F. Sun, Thickness-Dependent Morphologies of Gold on N-Layer Graphenes. J Am Chem Soc 132 (2010) 944-946.

[158] B.N. Szafranek, D. Schall, M. Otto, D. Neumaier, H. Kurz, High On/Off Ratios in Bilayer Graphene Field Effect Transistors Realized by Surface Dopants. Nano Lett 11 (2011) 2640-2643.

[159] Y.Y. Hui, G.A. Tai, Z.H. Sun, Z.H. Xu, N. Wang, F. Yan, S.P. Lau, n- and p-Type modulation of ZnO nanomesh coated graphene field effect transistors. Nanoscale 4 (2012) 3118-3122.

[160] J.T. Han, B.J. Kim, B.G. Kim, J.S. Kim, B.H. Jeong, S.Y. Jeong, H.J. Jeong, J.H. Cho, G.-W. Lee, Enhanced Electrical Properties of Reduced Graphene Oxide Multilayer Films by In-Situ Insertion of a TiO_2 Layer. Acs Nano 5 (2011)

8884-8891.

[161] S. Chen, J.W. Zhu, X.D. Wu, Q.F. Han, X. Wang, Graphene Oxide-MnO2 Nanocomposites for Supercapacitors. Acs Nano 4 (2010) 2822-2830.

[162] H.X. Chang, Z.H. Sun, K.Y.F. Ho, X.M. Tao, F. Yan, W.M. Kwok, Z.J. Zheng, A highly sensitive ultraviolet sensor based on a facile in situ solution-grown ZnO nanorod/graphene heterostructure. Nanoscale 3 (2011) 258-264.

[163] S.X. Wu, Z.Y. Yin, Q.Y. He, X.A. Huang, X.Z. Zhou, H. Zhang, Electrochemical Deposition of Semiconductor Oxides on Reduced Graphene Oxide-Based Flexible, Transparent, and Conductive Electrodes. J Phys Chem C 114 (2010) 11816-11821.

[164] H.X. Chang, X.J. Lv, H. Zhang, J.H. Li, Quantum dots sensitized graphene: In situ growth and application in photoelectrochemical cells. Electrochem Commun 12 (2010) 483-487.

[165] A. Cao, Z. Liu, S. Chu, M. Wu, Z. Ye, Z. Cai, Y. Chang, S. Wang, Q. Gong, Y. Liu, A Facile One-step Method to Produce Graphene–CdS Quantum Dot Nanocomposites as Promising Optoelectronic Materials. Adv Mater 22 (2010) 103-106.

[166] S. Huh, J. Park, K.S. Kim, B.H. Hong, S. Bin Kim, Selective n-Type Doping of Graphene by Photo-patterned Gold Nanoparticles. Acs Nano 5 (2011) 3639-3644.

[167] H.M.A. Hassan, V. Abdelsayed, A.E.R.S. Khder, K.M. AbouZeid, J. Terner,

M.S. El-Shall, S.I. Al-Resayes, A.A. El-Azhary, Microwave synthesis of graphene sheets supporting metal nanocrystals in aqueous and organic media. J Mater Chem 19 (2009) 3832-3837.

[168] T. Cassagneau, J.H. Fendler, Preparation and layer-by-layer self-assembly of silver nanoparticles capped by graphite oxide nanosheets. J Phys Chem B 103 (1999) 1789-1793.

[169] L.M. Dai, Layered Graphene/Quantum Dots: Nanoassemblies for Highly Efficient Solar Cells. Chemsuschem 3 (2010) 797-799.

[170] S.R. Sun, L. Gao, Y.Q. Liu, Enhanced dye-sensitized solar cell using graphene-TiO_2 photoanode prepared by heterogeneous coagulation. Appl Phys Lett 96 (2010) 3318466.

[171] Y.B. Tang, C.S. Lee, J. Xu, Z.T. Liu, Z.H. Chen, Z.B. He, Y.L. Cao, G.D. Yuan, H.S. Song, L.M. Chen, L.B. Luo, H.M. Cheng, W.J. Zhang, I. Bello, S.T. Lee, Incorporation of Graphenes in Nanostructured TiO_2 Films via Molecular Grafting for Dye-Sensitized Solar Cell Application. Acs Nano 4 (2010) 3482-3488.

[172] N.L. Yang, J. Zhai, D. Wang, Y.S. Chen, L. Jiang, Two-Dimensional Graphene Bridges Enhanced Photoinduced Charge Transport in Dye-Sensitized Solar Cells. Acs Nano 4 (2010) 887-894.

[173] J.L. Johnson, A. Behnam, S.J. Pearton, A. Ural, Hydrogen Sensing Using Pd-Functionalized Multi-Layer Graphene Nanoribbon Networks. Adv Mater

22 (2010) 4877-4880.

[174] K. Wang, Q.A. Liu, X.Y. Wu, Q.M. Guan, H.N. Li, Graphene enhanced electrochemiluminescence of CdS nanocrystal for H_2O_2 sensing. Talanta 82 (2010) 372-376.

[175] W.G. Tu, Y. Zhou, Q. Liu, Z.P. Tian, J. Gao, X.Y. Chen, H.T. Zhang, J.G. Liu, Z.G. Zou, Robust Hollow Spheres Consisting of Alternating Titania Nanosheets and Graphene Nanosheets with High Photocatalytic Activity for CO_2 Conversion into Renewable Fuels. Adv Funct Mater 22 (2012) 1215-1221.

[176] H. Zhang, X.J. Lv, Y.M. Li, Y. Wang, J.H. Li, P25-Graphene Composite as a High Performance Photocatalyst. Acs Nano 4 (2010) 380-386.

[177] L.H. Tang, Y. Wang, Y.M. Li, H.B. Feng, J. Lu, J.H. Li, Preparation, Structure, and Electrochemical Properties of Reduced Graphene Sheet Films. Adv Funct Mater 19 (2009) 2782-2789.

[178] X.F. Zhou, F. Wang, Y.M. Zhu, Z.P. Liu, Graphene modified $LiFePO_4$ cathode materials for high power lithium ion batteries. J Mater Chem 21 (2011) 3353-3358.

[179] H.L. Wang, Y. Yang, Y.Y. Liang, L.F. Cui, H.S. Casalongue, Y.G. Li, G.S. Hong, Y. Cui, H.J. Dai, $LiMn_{1-x}Fe_xPO4$ Nanorods Grown on Graphene Sheets for Ultrahigh-Rate-Performance Lithium Ion Batteries. Angew Chem Int Edit 50 (2011) 7364-7368.

[180] M.H. Liang, L.J. Zhi, Graphene-based electrode materials for rechargeable lithium batteries. J Mater Chem 19 (2009) 5871-5878.

[181] S.M. Paek, E. Yoo, I. Honma, Enhanced Cyclic Performance and Lithium Storage Capacity of SnO_2/Graphene Nanoporous Electrodes with Three-Dimensionally Delaminated Flexible Structure. Nano Lett 9 (2009) 72-75.

[182] M.D. Stoller, S.J. Park, Y.W. Zhu, J.H. An, R.S. Ruoff, Graphene-Based Ultracapacitors. Nano Lett 8 (2008) 3498-3502.

[183] C. Wang, H. Dong, W. Hu, Y. Liu, D. Zhu, Semiconducting π-Conjugated Systems in Field-Effect Transistors: A Material Odyssey of Organic Electronics. Chem Rev 112 (2011) 2208-2267.

[184] A. Facchetti, Semiconductors for organic transistors. Mater Today 10 (2007) 28-37.

[185] S. Ono, N. Minder, Z. Chen, A. Facchetti, A.F. Morpurgo, High-performance n-type organic field-effect transistors with ionic liquid gates. Appl Phys Lett 97 (2010) 3493190.

[186] C. Rost, S. Karg, W. Riess, M.A. Loi, M. Murgia, M. Muccini, Ambipolar light-emitting organic field-effect transistor. Appl Phys Lett 85 (2004) 1613-1615.

[187] J. Huang, J. Sun, H.E. Katz, Monolayer-dimensional 5,5'-Bis(4-hexylphenyl)-2,2'-bithiophene transistors and chemically

responsive heterostructures. Adv Mater 20 (2008) 2567-2572.

[188] J.H. Burroughes, D.D.C. Bradley, A.R. Brown, R.N. Marks, K. Mackay, R.H. Friend, P.L. Burns, A.B. Holmes, Light-Emitting-Diodes Based on Conjugated Polymers. Nature 347 (1990) 539-541.

[189] W.U. Huynh, J.J. Dittmer, A.P. Alivisatos, Hybrid nanorod-polymer solar cells. Science 295 (2002) 2425-2427.

[190] Y.Y. Lin, T.H. Chu, S.S. Li, C.H. Chuang, C.H. Chang, W.F. Su, C.P. Chang, M.W. Chu, C.W. Chen, Interfacial Nanostructuring on the Performance of Polymer/TiO_2 Nanorod Bulk Heterojunction Solar Cells. J Am Chem Soc 131 (2009) 3644-3649.

[191] J. Boucle, S. Chyla, M.S.P. Shaffer, J.R. Durrant, D.D.C. Bradley, J. Nelson, Hybrid solar cells from a blend of poly(3-hexylthiophene) and ligand-capped TiO_2 nanorods. Adv Funct Mater 18 (2008) 622-633.

[192] Q.D. Tai, X.Z. Zhao, F. Yan, Hybrid solar cells based on poly(3-hexylthiophene) and electrospun TiO_2 nanofibers with effective interface modification. J Mater Chem 20 (2010) 7366-7371.

[193] S.J. Wu, Q.D. Tai, F. Yan, Hybrid Photovoltaic Devices Based on Poly (3-hexylthiophene) and Ordered Electrospun ZnO Nanofibers. J Phys Chem C 114 (2010) 6197-6200.

[194] J.E. Kroeze, T.J. Savenije, M.J.W. Vermeulen, J.M. Warman, Contactless determination of the photoconductivity action spectrum, exciton diffusion

length, and charge separation efficiency in polythiophene-sensitized TiO_2 bilayers. J Phys Chem B 107 (2003) 7696-7705.

[195] J.W. Thackeray, M.S. Wrighton, Chemically Responsive Microelectrochemical Devices Based on Platinized Poly(3-Methylthiophene) - Variation in Conductivity with Variation in Hydrogen, Oxygen, or Ph in Aqueous-Solution. J Phys Chem-Us 90 (1986) 6674-6679.

[196] Z. Bao, A. Dodabalapur, A.J. Lovinger, Soluble and processable regioregular poly(3-hexylthiophene) for thin film field-effect transistor applications with high mobility. Appl Phys Lett 69 (1996) 4108-4110.

[197] H. Sirringhaus, P.J. Brown, R.H. Friend, M.M. Nielsen, K. Bechgaard, B.M.W. Langeveld-Voss, A.J.H. Spiering, R.A.J. Janssen, E.W. Meijer, P. Herwig, D.M. de Leeuw, Two-dimensional charge transport in self-organized, high-mobility conjugated polymers. Nature 401 (1999) 685-688.

[198] J.F. Chang, B.Q. Sun, D.W. Breiby, M.M. Nielsen, T.I. Solling, M. Giles, I. McCulloch, H. Sirringhaus, Enhanced mobility of poly(3-hexylthiophene) transistors by spin-coating from high-boiling-point solvents. Chem Mater 16 (2004) 4772-4776.

[199] Y.D. Park, H.S. Lee, Y.J. Choi, D. Kwak, J.H. Cho, S. Lee, K. Cho, Solubility-Induced Ordered Polythiophene Precursors for High-Performance Organic Thin-Film Transistors. Adv Funct Mater 19 (2009) 1200-1206.

[200] D.H. Kim, Y.D. Park, Y.S. Jang, H.C. Yang, Y.H. Kim, J.I. Han, D.G. Moon,

S.J. Park, T.Y. Chang, C.W. Chang, M.K. Joo, C.Y. Ryu, K.W. Cho, Enhancement of field-effect mobility due to surface-mediated molecular ordering in regioregular polythiophene thin film transistors. Adv Funct Mater 15 (2005) 77-82.

[201] G.M. Wang, J. Swensen, D. Moses, A.J. Heeger, Increased mobility from regioregular poly(3-hexylthiophene) field-effect transistors. J Appl Phys 93 (2003) 6137-6141.

[202] M. Brinkmann, J.C. Wittmann, Orientation of regioregular poly(3-hexylthiophene) by directional solidification: A simple method to reveal the semicrystalline structure of a conjugated polymer. Adv Mater 18 (2006) 860-863.

[203] S. Cho, K. Lee, J. Yuen, G.M. Wang, D. Moses, A.J. Heeger, M. Surin, R. Lazzaroni, Thermal annealing-induced enhancement of the field-effect mobility of regioregular poly(3-hexylthiophene) films. J Appl Phys 100 (2006) 2400796.

[204] C.A. Di, K. Lu, L. Zhang, Y.Q. Liu, Y.L. Guo, X.N. Sun, Y.G. Wen, G. Yu, D.B. Zhu, Solvent-Assisted Re-annealing of Polymer Films for Solution-Processable Organic Field-Effect Transistors. Adv Mater 22 (2010) 1273-1277.

[205] S.J. Wu, J.H. Li, Q.D. Tai, F. Yan, Investigation of High-Performance Air-Processed Poly(3-hexylthiophene)/Methanofullerene

Bulk-Heterojunction Solar Cells. J Phys Chem C 114 (2010) 21873-21877.

[206] K.M. Coakley, B.S. Srinivasan, J.M. Ziebarth, C. Goh, Y.X. Liu, M.D. McGehee, Enhanced hole mobility in regioregular polythiophene infiltrated in straight nanopores. Adv Funct Mater 15 (2005) 1927-1932.

[207] C.M. Liu, H. Sun, S.H. Yang, From Nanorods to Atomically Thin Wires of Anatase TiO_2: Nonhydrolytic Synthesis and Characterization. Chem-Eur J 16 (2010) 4381-4393.

[208] Y.Y. Lin, T.H. Chu, C.W. Chen, W.F. Su, Improved performance of polymer/TiO_2 nanorod bulk heterojunction photovoltaic devices by interface modification. Appl Phys Lett 92 (2008) 2839405.

[209] P.J. Brown, H. Sirringhaus, M. Harrison, M. Shkunov, R.H. Friend, Optical spectroscopy of field-induced charge in self-organized high mobility poly(3-hexylthiophene). Phys Rev B 63 (2001) 125204.

[210] P.J. Brown, D.S. Thomas, A. Köhler, J.S. Wilson, J.-S. Kim, C.M. Ramsdale, H. Sirringhaus, R.H. Friend, Effect of interchain interactions on the absorption and emission of poly(3-hexylthiophene). Phys Rev B 67 (2003) 064203.

[211] M. Brinkmann, D. Aldakov, F. Chandezon, Fabrication of oriented and periodic hybrid nanostructures of regioregular poly(3-hexylthiophene) and CdSe nanocrystals by directional epitaxial solidification. Adv Mater 19 (2007) 3819-3823.

[212] M.A. Lampert, P. Mark, Current Injection in Solids, Academic Press, Inc,

1970.

[213] S.A. McDonald, G. Konstantatos, S.G. Zhang, P.W. Cyr, E.J.D. Klem, L. Levina, E.H. Sargent, Solution-processed PbS quantum dot infrared photodetectors and photovoltaics. Nat Mater 4 (2005) 138-142.

[214] E. Perzon, F. Zhang, M. Andersson, W. Mammo, O. Inganäs, M.R. Andersson, A Conjugated Polymer for Near Infrared Optoelectronic Applications. Adv Mater 19 (2007) 3308-3311.

[215] B. Chitara, L.S. Panchakarla, S.B. Krupanidhi, C.N.R. Rao, Infrared Photodetectors Based on Reduced Graphene Oxide and Graphene Nanoribbons. Adv Mater 23 (2011) 5419-5424.

[216] H. Chen, Y. Guo, G. Yu, Y. Zhao, J. Zhang, D. Gao, H. Liu, Y. Liu, Highly π-Extended Copolymers with Diketopyrrolopyrrole Moieties for High-Performance Field-Effect Transistors. Adv Mater 24 (2012) n/a-n/a.

[217] J.H. Li, Z.H. Sun, F. Yan, Solution Processable Low-Voltage Organic Thin Film Transistors with High-k Relaxor Ferroelectric Polymer as Gate Insulator. Adv Mater 24 (2012) 88-93.

[218] L. Wen, B.C. Duck, P.C. Dastoor, S.C. Rasmussen, Poly(2,3-dihexylthieno[3,4-b]pyrazine) via GRIM polymerization: Simple preparation of a solution processable, low-band-gap conjugated polymer. Macromolecules 41 (2008) 4576-4578.

[219] X. Gong, M.H. Tong, Y.J. Xia, W.Z. Cai, J.S. Moon, Y. Cao, G. Yu, C.L. Shieh,

B. Nilsson, A.J. Heeger, High-Detectivity Polymer Photodetectors with Spectral Response from 300 nm to 1450 nm. Science 325 (2009) 1665-1667.

[220] T. Rauch, M. Boberl, S.F. Tedde, J. Furst, M.V. Kovalenko, G.N. Hesser, U. Lemmer, W. Heiss, O. Hayden, Near-infrared imaging with quantum-dot-sensitized organic photodiodes. Nat Photonics 3 (2009) 332-336.

[221] S.M. Sze, Physics of Semiconductor Devices, , John Wiley & Sons, 1981.

[222] S. Zhang, P.W. Cyr, S.A. McDonald, G. Konstantatos, E.H. Sargent, Enhanced infrared photovoltaic efficiency in PbS nanocrystal/semiconducting polymer composites: 600-fold increase in maximum power output via control of the ligand barrier. Appl Phys Lett 87 (2005) 233101.

[223] J.H. Warner, E. Thomsen, A.R. Watt, N.R. Heckenberg, H. Rubinsztein-Dunlop, Time-resolved photoluminescence spectroscopy of ligand-capped PbS nanocrystals. Nanotechnology 16 (2005) 175-179.

[224] F. Bonaccorso, Z. Sun, T. Hasan, A.C. Ferrari, Graphene photonics and optoelectronics. Nat Photonics 4 (2010) 611-622.

[225] B. Pradhan, K. Setyowati, H.Y. Liu, D.H. Waldeck, J. Chen, Carbon nanotube - Polymer nanocomposite infrared sensor. Nano Lett 8 (2008) 1142-1146.

[226] F. Yan, P. Migliorato, R. Ishihara, Simulation of twin boundary effect on characteristics of single grain-silicon thin film transistors. Appl Phys Lett 91 (2007) 073509.

[227] G. Adamopoulos, S. Thomas, P.H. Wobkenberg, D.D.C. Bradley, M.A.

McLachlan, T.D. Anthopoulos, High-Mobility Low-Voltage ZnO and Li-Doped ZnO Transistors Based on ZrO_2 High-k Dielectric Grown by Spray Pyrolysis in Ambient Air. Adv Mater 23 (2011) 1894-1898.

[228] N.M. Gabor, J.C.W. Song, Q. Ma, N.L. Nair, T. Taychatanapat, K. Watanabe, T. Taniguchi, L.S. Levitov, P. Jarillo-Herrero, Hot Carrier-Assisted Intrinsic Photoresponse in Graphene. Science 334 (2011) 648-652.

[229] D. Sun, G. Aivazian, A.M. Jones, J.S. Ross, W. Yao, D. Cobden, X.D. Xu, Ultrafast hot-carrier-dominated photocurrent in graphene. Nat Nanotechnol 7 (2012) 114-118.

[230] R.X. He, P. Lin, Z.K. Liu, H.W. Zhu, X.Z. Zhao, H.L.W. Chan, F. Yan, Solution-Gated Graphene Field Effect Transistors Integrated in Microfluidic Systems and Used for Flow Velocity Detection. Nano Lett 12 (2012) 1404-1409.

[231] C. Mattevi, H. Kim, M. Chhowalla, A review of chemical vapour deposition of graphene on copper. J Mater Chem 21 (2011) 3324-3334.

[232] Z.G. Cheng, Q.Y. Zhou, C.X. Wang, Q.A. Li, C. Wang, Y. Fang, Toward Intrinsic Graphene Surfaces: A Systematic Study on Thermal Annealing and Wet-Chemical Treatment of SiO_2-Supported Graphene Devices. Nano Lett 11 (2011) 767-771.

[233] J.H. Chen, C. Jang, S. Adam, M.S. Fuhrer, E.D. Williams, M. Ishigami, Charged-impurity scattering in graphene. Nat Phys 4 (2008) 377-381.

[234] A.K. Rath, M. Bernechea, L. Martinez, G. Konstantatos, Solution-Processed Heterojunction Solar Cells Based on p-type PbS Quantum Dots and n-type Bi2S3 Nanocrystals. Adv Mater 23 (2011) 3712-3717.

[235] D.B. Farmer, R. Golizadeh-Mojarad, V. Perebeinos, Y.M. Lin, G.S. Tulevski, J.C. Tsang, P. Avouris, Chemical Doping and Electron-Hole Conduction Asymmetry in Graphene Devices. Nano Lett 9 (2009) 388-392.

[236] A.J. Hong, E.B. Song, H.S. Yu, M.J. Allen, J. Kim, J.D. Fowler, J.K. Wassei, Y. Park, Y. Wang, J. Zou, R.B. Kaner, B.H. Weiller, K.L. Wang, Graphene Flash Memory. Acs Nano 5 (2011) 7812-7817.

[237] S. Wang, J. Pu, D.S.H. Chan, B.J. Cho, K.P. Loh, Wide memory window in graphene oxide charge storage nodes. Appl Phys Lett 96 (2010) 3383234.

[238] Y.J. Doh, G.C. Yi, Nonvolatile memory devices based on few-layer graphene films. Nanotechnology 21 (2010) 105204.

[239] E.B. Song, B. Lian, S.M. Kim, S. Lee, T.K. Chung, M.S. Wang, C.F. Zeng, G.Y. Xu, K. Wong, Y. Zhou, H.I. Rasool, D.H. Seo, H.J. Chung, J. Heo, S. Seo, K.L. Wang, Robust bi-stable memory operation in single-layer graphene ferroelectric memory. Appl Phys Lett 99 (2011) 3619816.

[240] B. Standley, W.Z. Bao, H. Zhang, J. Bruck, C.N. Lau, M. Bockrath, Graphene-Based Atomic-Scale Switches. Nano Lett 8 (2008) 3345-3349.

[241] D.I. Son, T.W. Kim, J.H. Shim, J.H. Jung, D.U. Lee, J.M. Lee, W. Il Park, W.K. Choi, Flexible Organic Bistable Devices Based on Graphene Embedded

in an Insulating Poly(methyl methacrylate) Polymer Layer. Nano Lett 10 (2010) 2441-2447.

[242] D. Gunlycke, D.A. Areshkin, J.W. Li, J.W. Mintmire, C.T. White, Graphene nanostrip digital memory device. Nano Lett 7 (2007) 3608-3611.

[243] X.M. Wang, W.G. Xie, J. Du, C.L. Wang, N. Zhao, J.B. Xu, Graphene/Metal Contacts: Bistable States and Novel Memory Devices. Adv Mater 24 (2012) 2614-2619.

[244] T.J. Echtermeyer, M.C. Lemme, M. Baus, B.N. Szafranek, A.K. Geim, H. Kurz, Nonvolatile switching in graphene field-effect devices. Ieee Electr Device L 29 (2008) 952-954.

[245] D. Lee, S.M. Yang, T.H. Kim, B.C. Jeon, Y.S. Kim, J.G. Yoon, H.N. Lee, S.H. Baek, C.B. Eom, T.W. Noh, Multilevel Data Storage Memory Using Deterministic Polarization Control. Adv Mater 24 (2012) 402-406.

[246] H.K. Lau, C.W. Leung, Nonvolatile multilevel memory effect by resistive switching in manganite thin films. J Appl Phys 104 (2008) 3043801.

[247] Y.T. Lu, S.B. Long, Q. Liu, Q. Wang, M.H. Zhang, H.B. Lv, L.B. Shao, Y. Wang, S. Zhang, Q.Y. Zuo, S. Liu, M. Liu, Nonvolatile multilevel memory effect in Cu/WO_3/Pt device structures. Phys Status Solidi-R 4 (2010) 124-126.

[248] S.K. Hwang, J.M. Lee, S. Kim, J.S. Park, H.I. Park, C.W. Ahn, K.J. Lee, T. Lee, S.O. Kim, Flexible Multilevel Resistive Memory with Controlled Charge Trap Band N-Doped Carbon Nanotubes. Nano Lett 12 (2012) 2217-2221.

[249] Q.L. Li, G. Mathur, S. Gowda, S. Surthi, Q. Zhao, L.H. Yu, J.S. Lindsey, D.F. Bocian, V. Misra, Multibit memory using self-assembly of mixed ferrocene/porphyrin monolayers on silicon. Adv Mater 16 (2004) 133-137.

[250] A.K. Tripathi, A.J.J.M. van Breemen, J. Shen, Q. Gao, M.G. Ivan, K. Reimann, E.R. Meinders, G.H. Gelinck, Multilevel Information Storage in Ferroelectric Polymer Memories. Adv Mater 23 (2011) 4146-4151.

[251] S. Raoux, W. Welnic, D. Ielmini, Phase Change Materials and Their Application to Nonvolatile Memories. Chem Rev 110 (2010) 240-267.

[252] C.J. Kim, S.J. Choi, S. Kim, J.W. Han, H. Kim, S. Yoo, Y.K. Choi, Photoinduced Memory with Hybrid Integration of an Organic Fullerene Derivative and an Inorganic Nanogap-Embedded Field-Effect Transistor for Low-Voltage Operation. Adv Mater 23 (2011) 3326-3331.

[253] Y.J. Liu, R.O. Claus, Blue light emitting nanosized TiO_2 colloids. J Am Chem Soc 119 (1997) 5273-5274.

[254] Q. Wang, X.F. Guo, L.C. Cai, Y. Cao, L. Gan, S. Liu, Z.X. Wang, H.T. Zhang, L.D. Li, TiO_2-decorated graphenes as efficient photoswitches with high oxygen sensitivity. Chem Sci 2 (2011) 1860-1864.

[255] Y.H. Zhang, Z.R. Tang, X.Z. Fu, Y.J. Xu, TiO2-Graphene Nanocomposites for Gas-Phase Photocatalytic Degradation of Volatile Aromatic Pollutant: Is TiO_2-Graphene Truly Different from Other TiO_2-Carbon Composite Materials? Acs Nano 4 (2010) 7303-7314.